Computational Fluid Dynamics Modelling of Incompressible Flow and Mixing in Continuous Microreactors

Antonio D'Orazio

Thesis submitted to the University of Ottawa
in partial Fulfillment of the requirements for the degree of
Master of Applied Science in Chemical Engineering

Department of Chemical and Biological Engineering
Faculty of Engineering
University of Ottawa

uOttawa

February 2021

Abstract

Continuous milli-scale and micro-scale structures such as FlowPlate® microreactors have emerged as a promising element of process intensification due to their inherently effective rates of mass and heat transfer. These microfluidic devices have proven to be a preferred solution in place of energy-intensive batch processes for certain pathways of fine chemical and pharmaceutical synthesis, most notably fast reactions taking place on the scale of milliseconds to seconds. Computational fluid dynamics (CFD) has become an increasingly valuable tool in the field of microreactor design and optimization for its ability to locally map complex fluid flow patterns and resolve microscopic scales of reactive mixing that are challenging to characterize experimentally.

The primary objective of this research was thus to develop and validate a mathematical model for the simulation of chaotic flow and homogeneous mixing in continuous microreactors. The model needed to be versatile enough to handle transition between flow regimes within a given reactor as well as the coexistence of both chaotic and laminar flow patterns in the micromixing elements that comprise said reactors. This was successfully achieved through the implementation of a *k-ω* SST (shear-stress transport) turbulence model that accounts for the impact of small-scale temporal and spatial fluctuations generated in the micromixer geometries studied herein; be it a liquid-liquid mixer (LLM), a serpentine (SZ) or a tangential (TG) mixer. In a first CFD study, the computational predictions were validated based on excellent agreement with experimental pressure loss ($R^2 > 0.997$) and residence time distribution (RTD) data ($R^2 > 0.97$) in several LL microreactors at Reynolds numbers ranging from 210 to 2140. Furthermore, the local velocity distribution and streamlines were mapped across the 3D domain of these reactors and it was discovered, based on the emergence of advective recirculation zones and turbulent dispersion, that a drastic change in flow behaviour occurred in these mixing elements at a Reynolds number of about 640. The interspacing of LLM elements with straight microchannels proved to be a suitable approach to modulating pressure loss while concurrently maintaining the chaotic secondary flow patterns generated from the mixers.

In a second CFD study, the impact of micromixer geometry on the local velocity fields and advective transport performance was investigated both from a macromixing and micromixing perspective. Like the LLM, the SZ and TG mixers conferred chaotic secondary flow patterns at

characteristic Reynolds numbers between 500 and 1000. As such, it was concluded that it would be ideal to operate these mixers at water flow rates of at least 30 ml/min. Contour plots of the velocity magnitude coupled with the computation of RTD showed that the SZ virtually mimics a plug-flow profile over a volume of 77 mm^3 or greater at 50 g/min. The RTD of the LLM and TG resembles that of a mixed flow pattern given that approximately 65-80% of their fluid volume is occupied by recirculation zones. As such, it required 65 LLMs in series (3105 mm^3) and 80 TGs (1142 mm^3) to approach the same pattern as 10 SZs (77 mm^3) from a macromixing perspective. Micromixing time distributions (MTD) were also characterized by locally computing the decay time of small-scale segregation (t_{SSS}) as a function of flow rate, wherein higher flow rates generated lower characteristic mixing times. The TG and LLM conferred the broadest range of mixing times, spanning nearly four orders of magnitude in the range of [0.02 ms, 10 ms], whereas the SZ generated a much narrower MTD ranging between [0.024 ms, 0.69 ms].

Finally, the impact of geometry and flow conditions on reaction yield was assessed by characterizing the extent of a finite-rate reaction relative to an infinitely fast reaction taking place in parallel. The calculated yield for the competitive-parallel reaction scheme showed that the second Damköhler number (Da_{II}) computed based on the mean t_{SSS} provides useful information about whether the process will be limited by the intrinsic rate of reaction or by the rate of mass transfer, even though the reaction process is controlled by a combination of the RTD as well as loss of LSS and SSS. It was concluded that the change in MTD as a function of power dissipation should coincide with the reaction yield response, and that any deviation in that relationship is because of macroscopic blending of reactants in the entrance region.

Résumé

Les structures à échelle microscopique en opération continu, telles que les microréacteurs FlowPlate®, sont devenues un élément important dans l'intensification de procédés industrielles en raison du taux de transfert de masse et chaleur intrinsèquement efficaces à celles-ci. Comme instruments microfluidiques, les microréacteurs représentent souvent une meilleure option pour entreprendre la synthèse de produits pharmaceutiques comparés aux réacteurs en opération discontinu, surtout pour les réactions rapides qui sont susceptibles à des limitations par rapport au taux de mélange. La modélisation mathématique des motifs d'écoulement dynamiques – c'est-à-dire la simulation par *computational fluid dynamics* (CFD) – est devenue de plus en plus important comme outil dans le domaine de conception et optimisation de microréacteurs. Cette approche permet la caractérisation des profils de vitesse ainsi que la résolution de plusieurs échelles de mélange en milieu réactionnaire au niveau locale qui sont difficile, ou même impossible, à analyser expérimentalement.

L'objectif primaire de cette thèse était donc de développer et de valider un modèle mathématique pour la simulation d'écoulement et de mélange homogène en régime chaotique dans les microréacteurs à opération continu. Le modèle fallait être suffisamment versatile pour gérer la transition entre régimes d'écoulement dans plusieurs géométries quelconque, ainsi que la coexistence de motifs chaotiques et laminaires dans les éléments de mélange passif qui comprennent ces réacteurs. Ceci a été réalisé grâce à un modèle *k-ω* SST (*shear-stress transport*) capable de préciser l'impact des fluctuations temporelles et spatiales à petite échelle générées dans trois géométries uniques : un mélangeur liquide-liquide (LLM), un mélangeur serpentin (SZ) et un mélangeur tangentiel (TG). Dans une première étude numérique, les résultats provenant des simulations CFD ont été validées par étant bien en accord avec les données expérimentale de perte de pression ($R^2 > 0.997$) ainsi qu'avec les données de distribution des temps de séjour (*residence time distribution*, RTD) ($R^2 > 0.97$) dans plusieurs microréacteurs LL. Cette validation a été complété à des nombres de Reynolds allant de 210 à 2140. Ensuite, les distributions de la vitesse locale et des lignes de courant ont été cartographiées à travers le domaine 3D de ces réacteurs. Il a été découvert qu'un changement fondamental du comportement d'écoulement s'est produit dans ces géométries à un nombre de Reynolds d'environ 640. Ceci a été conclu à partir de l'apparition de zones de recirculation chaotique et de dispersion turbulente. L'utilisation de canaux

rectangulaires qui espacent les mélangeurs passives s'est avéré être une approche appropriée pour moduler la perte de pression tout en gardant simultanément les motifs d'écoulement secondaire chaotiques générés par les mélangeurs.

Dans une deuxième étude numérique, l'objectif était d'analyser l'impact de la géométrie des mélangeurs sur les profils de vitesse et sur la performance de transport par advection. Ce dernier a été caractérisé du point de vue de mélange macroscopique et microscopique. Comme le LLM, les mélangeurs SZ et TG conféraient des motifs d'écoulement secondaire chaotiques à des nombres de Reynolds caractéristiques entre 500 et 1000. En tant que tel, il a été conclu qu'il serait idéal d'opérer ces mélangeurs à des débits d'eau d'au moins 30 ml/min. Le profil de vitesse ainsi que le RTD à ce débit montrent du point de vue macroscopique que le mélangeur SZ imite un profile piston (*plug-flow*) à travers un volume d'au moins 77 mm^3. Le RTD du LLM et du TG ressemblait plutôt à celui d'un profile parfaitement mélangé étant donné qu'environ 65-80% du volume de fluide est occupé par des zones de recirculation dans ceux-ci. Il a fallu 65 mélangeurs LLM en série (3105 mm^3) et 80 TG (1142 mm^3) pour s'approcher du même RTD que 10 SZ (77 mm^3). Les distributions de temps de mélange du point de vue microscopique (MTD) ont également été caractérisées en calculant localement le temps de ségrégation à petite échelle (*small-scale segregation time*, t_{SSS}) en fonction du débit. Comme prévu, les débits plus élevés génèrent des temps caractéristiques de mélange plus courtes. Le TG et le LLM conféraient la plus large gamme de temps de mélange, couvrant près de quatre ordres de magnitude dans la gamme de [0,02 ms, 10 ms], tandis que le SZ générait un MTD beaucoup plus étroit compris entre [0,024 ms, 0,69 ms].

Finalement, l'impact de la géométrie sur le rendement de réaction a été évalué en caractérisant le taux d'une réaction à vitesse finie par rapport à une réaction infiniment rapide se déroulant en parallèle. Le rendement global calculé pour ce réseau de réactions en série a démontré que le deuxième nombre de Damköhler (Da_{II}) obtenu en fonction du t_{SSS} nous indique si le taux effectif du processus sera limité par la vitesse intrinsèque de réaction ou par la vitesse de transfert de masse; même bien que le processus de réaction soit contrôlé par une combinaison du RTD ainsi que par la perte de LSS et de SSS. Il a été conclu que le changement de MTD en fonction de la dissipation de puissance devrait coïncider avec le rendement de réaction calculé, et que tout écart dans cette relation est dû aux effets de mélange macroscopique des réactifs dans la région d'entrée.

Statement of Contributions of Collaborators

I hereby declare that I am the sole author of this thesis. The numerical work that I completed in this research through computational fluid dynamics (CFD) simulation was inspired by previous experimental work conducted on existing FlowPlate® microreactor geometries designed by Lonza. All CFD modelling, simulation results and post-processing of data described in this thesis is my own work.

Both of my thesis supervisors, Dr. Arturo Macchi and Dr. Jan Haelssig, provided weekly guidance in this research and contributed to the editing of both articles presented in Chapter 2 and Chapter 3. Dr. Dominique Roberge and his colleagues also provided continual support and guidance in this work as part of our group of industrial collaborators at Lonza. All three are listed as co-authors of the articles that make up this thesis.

The experimental pressure drop and residence time distribution (RTD) results used in Chapter 2 were previously gathered and analyzed by Craig Holvey and Alexandra Hopley, respectively, under the supervision of Dr. Macchi. This work served as a basis for the validation of the CFD model developed herein. The microreactor plates used in this experimental work were manufactured by Ehrfeld Mikrotechnik.

The preliminary modelling of the LL microreactors in AutoCAD was completed by Dr. Jan Haelssig. He also played a crucial role in the programming of custom macromixing and micromixing solvers in OpenFOAM. I was able to then build upon that numerical framework for the development and validation of the present CFD model by executing a vast library of flow and and mass transport simulations.

Acknowledgements

My sincere gratitude goes out to my supervisors Dr. Arturo Macchi and Dr. Jan Haelssig for providing me with the opportunity to complete computational work that will hopefully serve useful for academic and industrial groups interested in microreactor development through CFD. I thank them both for their vital roles in my professional development, for providing me with a project that is industry driven and that has a strong fundamental basis in fluid mechanics and chemical reaction engineering.

I would also like to thank the Natural Sciences and Engineering Research Council (NSERC) of Canada, particularly the CREATE program of Continuous Flow Science, as well as acknowledge the support received from the Ontario Graduate Scholarship (OGS) program. In addition, I thank ACENET and Compute Canada for providing computational resources and support for the vast number of CFD simulations completed in this work.

Industry partners at Lonza AG led by Dr. Dominique Roberge are acknowledged for their role in the design of continuous-flow microreactors and for their financial contribution. Ehrfeld Mikrotechnik are also acknowledged for their role in manufacturing the microreactors used in the previous experimental work tied to this research.

Finally, I am eternally grateful for the love and support of my friends and family over the course of these two years of graduate studies and five years of undergraduate studies.

Table of Contents

List of Figures

List of Tables

Chapter 1. Introduction

1.1. Microreactor technology and process intensification

The synthesis of fine chemicals and pharmaceuticals has traditionally been undertaken in solvent-intensive batch or semi-batch reactors [1]. These stirred-tank reactors have historically been – and still considered to be – the benchmark for many synthesis pathways in these industries due to their modularity, availability, and ease of scale-up [1–3]. However, recent social developments in process safety management and environmental awareness have led to the development of more volume-efficient, more economically viable and safer solutions. Process intensification can be defined as a paradigm shift in process equipment and design of manufacturing plants that serves this purpose by reducing equipment size and minimizing the number of unit operations. In general, microreactor technology represents a promising element of process intensification for fast chemical reactions because of their inherently effective rates of heat and mass transfer [4–7]. Microreactors are microfluidic devices that specialize in promoting efficient reactant mixing via small spatial dimensions to improve surface-to-volume ratio, and geometrical artifacts that perturbate the direction and magnitude of flow without the need for mechanical agitation. Thus, for synthesis pathways involving inherently fast reactions, these milli-/micro-scale structures have tremendous potential over traditional stirred-tank reactors. From an industrial perspective, the use of micromixing structures for large-scale production theoretically leads to a higher volumetric productivity and allows for safer handling of hazardous materials or unstable intermediates via shorter residence times, lower fluid inventory and more controlled operating conditions [8, 9]. In addition, microreactor plate(s) are often placed in between heating/cooling plates which adds another degree of process modulation via more efficient heat transfer. From a reaction engineering perspective, the improvement in mixing performance often translates into greater control of residence time and product selectivity, whereas the enhanced rate of heat transfer makes it inherently safer for undertaking fast exothermic reactions that are susceptible to thermal runaway [10].

Conversely, microreactors present challenges in the industrial manufacturing of certain chemicals, particularly those involving the processing of solids due to the increased risk of clogging [6]. The scale-up of these reactors is another obvious challenge to overcome given that

the surface-to-volume ratio diminishes as the characteristic dimensions are enlarged for higher throughput [11]. To overcome this challenge, a near-optimal reactor configuration (e.g., mixing regions interspaced with residence time channels as in Figure 1.1) and operating conditions are first identified for a given reaction, subsequently scaled up to flow rates relevant across all phases of clinical trials (1–600 ml/min), and finally parallelized if need be to meet industrial scale throughput [1, 12–15]. This thesis directly addresses the first of these points as it aims to generate new knowledge about the scales of mixing and flow patterns present in custom-designed FlowPlate® microreactors comprised of industrially-relevant micromixing structures. A robust and comprehensive computational fluid dynamics (CFD) model was developed for this purpose, which presented additional numerical challenges associated to the resolution of small-scale spatial and temporal fluctuations in regimes of chaotic advection.

1.2. FlowPlate® microreactors

Many continuous-flow microreactors have been designed and benchmarked by Lonza for a variety of single-phase, liquid-liquid or gas-liquid reactions. In general, they differ in terms of their passive mixing elements (Figure 1.2) and mixing configuration (Figure 1.1). For example, the liquid-liquid mixer (LLM: 9.22 × 5 × 1.25 mm; Figure 1.2A) is a split-and-recombine (SAR), venturi-like structure containing a rhombus obstacle that specializes in fluid-fluid contact and homogeneous liquid mixing [16, 17]. This mixing module served as the base case for the development and validation of the CFD model described in Chapter 2. This first simulation study was completed with respect to four different configurations of LL microreactors (Figure 1.1) to verify the accuracy and robustness of the model in transitioning between flow regimes within a given reactor (i.e., chaotic flow in the mixing region and laminar flow in the microchannels).

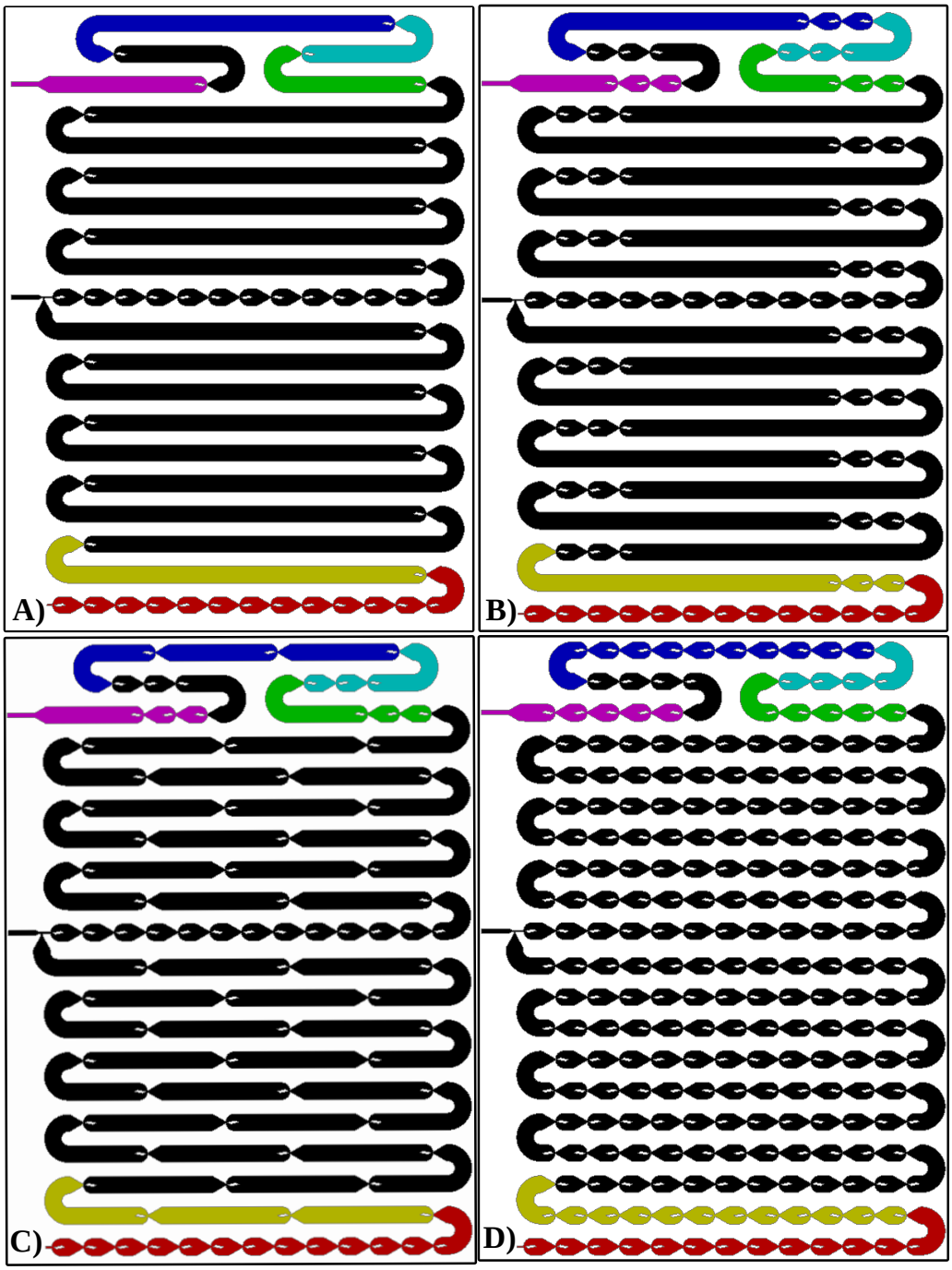

Figure 1.1. LL microreactor configurations: (A) minimal mixing, (B) grouped mixing, (C) equally-spaced mixing, and (D) continuous mixing. The colour-coded regions are repeating segments that were simulated independently (direction of flow is from left to right)

The model was then used to quantitatively investigate the impact of micromixer geometry by comparing the LLM to serpentine (SZ) and tangential (TG) mixers (Figure 1.2B and Figure 1.2C, respectively). As described in previous experimental work by Plouffe *et al*., these mixers are all best served for fast and/or exothermic reactions (i.e., Type A reactions) in the rate of reaction

range of milliseconds to seconds [1, 16, 18]. However, their proposed applications differ with respect to the reacting phase(s) that they take on; wherein the SZ is supposedly best served for homogeneous flow, the LLM is designed for contacting immiscible liquids, and the TG may be applied to gas-liquid reactions [1]. In Chapter 3, the macroscopic and microscopic mixing efficiency of incompressible flow in each geometry was characterized locally through CFD simulation.

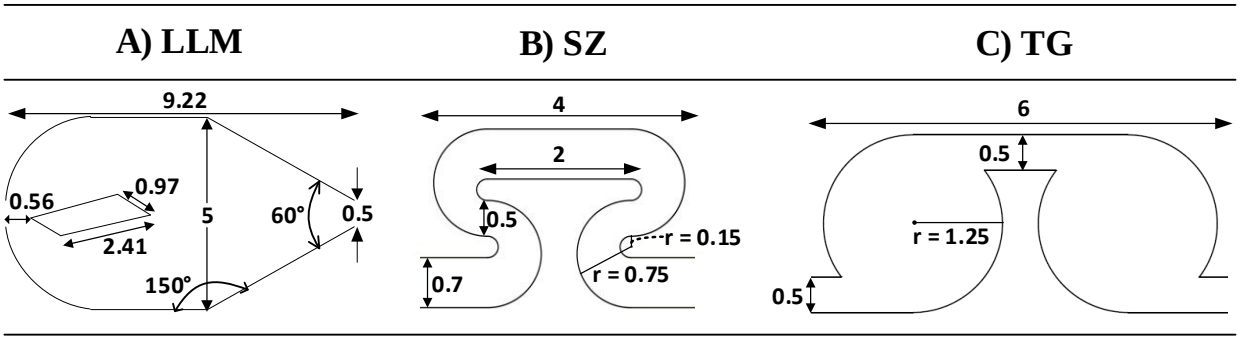

Figure 1.2. Micromixer dimensions in mm (geometries not drawn to scale). Direction of flow is from left to right

1.3. Mixing

The quality of mixing is an important phenomenon to consider in microreactor design, particularly for fast reaction applications in which the overall performance of the system is prone to mixing time limitations [19]. Generally it can be divided into three scales of mixing that occur in parallel: macromixing, mesomixing and micromixing [20]. Macromixing leads to a distribution of residence times involving the "packets" of fluid entering the system, but it does not describe how molecules of different age encounter one another in the system. The latter is characterized by the quality of micromixing; wherein a system is said to be completely mixed microscopically if the molecules of different residence times are completely blended at the molecular level, or completely segregated if the molecules of the same residence time do not mix with other age groups as they travel through the system. Finally, mesomixing occurs on a smaller scale relative to that of the system but coarser relative to micromixing and is often caused by the turbulent dispersion of a feed stream shortly after it enters a mixed system [21]. For a given set of reaction kinetics, the RTD and micromixing time distribution co-determine the distribution of products yielded from each reaction whether they are competitive or in series. As such, the development and validation of a complete mathematical model for predicting the fluid flow characteristics as well as the different levels of mixing down to the Kolmogorov scale was sought.

Mechanistically, the vast library of existing micromixing modules (i.e., micromixers) used in microreactor design are generally categorized as *active* or *passive*. Active mixing is defined as flow perturbation generated by an external energy source whereas passive mixing utilizes geometrical artifacts to create changes in flow direction and magnitude without external energy. Examples of active mixing devices include acoustic-based mixers that rely on magnetic fields and ultrasonic vibration [22, 23], which may also be combined with passive mixing elements such as serpentine channels and sharp-edged structures [24, 25]. Although these microfluidic devices have shown promise for lab-on-chip applications and for biomedical diagnostics [2], passive micromixers are often preferred for fine chemical synthesis since they confer less energy-intensive means of generating effective mixing via chaotic advection [26, 27]. Several articles have detailed the experimental analysis of microchannels with custom-design serpentine structures [28, 29], split-and-recombine (SAR) structures [30–32], flow-obstructing/separating structures as well as two-layer crossing channels [33]. However, few have gone about quantitatively comparing the mixing quality of these structures, be it experimentally or numerically. Falk and Commenge published one of the first comprehensive studies on the experimental characterization of mixing quality in various micromixers using a fast-competitive reaction scheme [34]. The characteristic micromixing times in this study were deduced from the product yield of the Villermaux-Dushman reaction as a function of Reynolds number and specific power dissipation [35]. Boskovic *et al.* did a similar comparative analysis of micromixer geometries in the same range of Reynolds numbers ($0.3 < Re < 110$) but rather from a macromixing perspective [36]. Most recently, Raza *et al.* completed a performance review of a much vaster library of micromixers using computational fluid dynamics (CFD) [2]. However, the latter study focused solely on the characterization of flow patterns for distinguishing different flow regimes without computing the distribution of residence times or micromixing times, and the comparison was only completed up to a Reynolds number of 120.

As described in Chapter 3, an important objective of this work was thus to complete a more thorough comparison of micromixers in terms of local fluid dynamics and different scales of mixing efficiency at higher Reynolds numbers (i.e., where chaotic advection is dominant and small-scale flow pattern fluctuations are challenging to resolve without turbulence modelling). Although the number of different geometries studied herein was limited, together they incorporate

many of the aforementioned passive mixing techniques (e.g., SAR, serpentine, tangential counter-rotating flow, etc.) reviewed in previous experimental and numerical work.

1.4. CFD modelling of continuous-flow microreactors

The application of CFD in microreactor design, optimization and scale-up has become widespread in both industry and academia as it allows for the mathematical modelling of local fluid dynamics and associated transport processes through simulation. Upon numerical validation, the use of these models in place of experimental methods can considerably mitigate environmental and economic impact tied to exploratory reaction conditions that may be overly expensive and/or hazardous to conduct experimentally. Moreover, the local characterization of velocity profiles, power dissipation, and species concentration are particularly important for reactor development because they provide information about the behaviour inside the reactor that is impractical to deduce experimentally. Although CFD modelling has been applied to microreactor design previously, few publications have employed turbulence modelling in complex microstructures, and less have aimed to use low-Re turbulence models to properly mimic chaotic advection at Reynolds numbers beyond 500. [15, 37–41]

Much effort has been invested in the CFD modelling of mixing at the microscopic/molecular scale (i.e., micromixing) in various reactors due to the importance of these phenomena in scaling of stirred-tank reactors [42], packed beds [43, 44], and micromixers [45–48]. Micromixing models aim to reproduce small-scale transport phenomena, which facilitates prediction of apparent reaction rates for both kinetically and mass-transfer limited reactions, thereby providing a better indication of how applicable a given geometry might be for undertaking a particular reaction pathway. Quantification of mixing efficiency via computational methods is now becoming a feasible alternative to experimentally using competitive reaction schemes to deduce mixing times. For example, the research by Fox and collaborators throughout the early 2000s led to the development and validation of a direct-quadrature-method-of-moments (DQMOM) coupled with an interaction-by-exchange-with-the-mean (IEM) model for locally computing small-scale and large-scale segregation time constants [49–52]. This DQMOM-IEM model was subsequently used to simulate competitive reactions for characterizing reactive mixing [52–54]. Since then, increasingly sophisticated models for characterizing the mixing time

computationally have been published, such as the hybrid approach proposed by Rizzotto *et al.* that combines a laminar rate model with a multiple time-scale model [55].

1.5. Thesis objectives and outline

The chief objective of this thesis was to develop a CFD model capable of simulating incompressible flow, mixing efficiency (both macroscopically and microscopically) and chemical reaction in continuous microreactors. The flow simulations covered in both articles were completed at Reynolds numbers ranging from 200 to 2100, and were carried out using the open-source software OpenFOAM (open-source field operation and manipulation) [56].

In Chapter 2, a mathematical model for predicting chaotic advection and scalar transport in continuous-flow microreactors was to be validated in comparison to previous experimental work on liquid and liquid-liquid reactor development [16–18, 57]. Pressure drop and RTD results in four different configurations of LL microreactors at flow rates ranging from 10 to 100 ml/min were obtained experimentally, wherein each configuration shared the same base mixing element but contained a different number of them with varying levels of spacing. As such, the accuracy and robustness of the model in transitioning between flow regimes for these geometries was questioned. A turbulence model capable of simulating the oscillation between chaotic flow in the LLM and laminar flow in the microchannels that interspace them was sought after. Upon validation, the four reactor configurations were to be compared more extensively in hope of ultimately mitigating pressure loss while maintaining the RTD for future design considerations.

In Chapter 3, additional mathematical components were implemented into the CFD model for locally computing the time constants of large-scale segregation (i.e., the macroscopic blending time) and small-scale segregation (i.e., the micromixing time), as well as the conversion of products yielded from a competitive reaction scheme. A quantitative study of single-phase flow and mixing in the LLM, SZ and TG mixers was also completed in order to better understand the impact of different geometrical micromixing elements. This comparative analysis aimed to provide detailed information about the flow patterns, local blending, RTD, MTD and reaction conversion occurring in each geometry, including a discussion of advantages and limitations. Based on previous experimental work, it was hypothesized that each benchmark micromixer would yield differences in RTD and MTD at equivalent flow rate, but not necessarily over equivalent power dissipation.

Chapter 2. CFD Simulation of Pressure Drop and Macromixing in LL Microreactors

Antonio O. D'Orazio [1], Jan B. Haelssig [2*], Dominique M. Roberge [3], Arturo Macchi [1*]

[1] *Department of Chemical and Biological Engineering, University of Ottawa, Ottawa, ON, Canada*

[2] *Department of Process Engineering and Applied Science, Dalhousie University, Halifax, NS, Canada*

[3] *Chemical Manufacturing Technologies, Lonza AG, CH-3930, Visp, Switzerland*

Abstract

A computational fluid dynamics (CFD) model was developed to simulate single-phase flow in LL microreactors using the open-source software OpenFOAM. The *k*-ω SSTLM turbulence model was implemented to account for the impact of small-scale temporal and spatial fluctuations that emerge in the base LL mixing module (LLM) on the flow field and transport of a passive scalar. The CFD model was successfully validated based on excellent conformance to experimental pressure loss ($R^2 > 0.997$) and residence time distribution (RTD) data ($R^2 > 0.97$) at flow rates ranging from 10 to 100 g/min. Streamlines, velocity, pressure, and turbulent viscosity profiles were mapped across the 3D domain of repeating reactor segments to analyze local fluid dynamics. In a continuous series of LLMs, the flow field becomes fully developed after the second module. A drastic change in flow behaviour in the LLM was identified at 30 g/min (Re = 643) based on the emergence of advective recirculation zones and significant turbulent dispersion. Recirculation zones in the LLM grow larger from 20 to 50 g/min and are equal in size from 50 to 100 g/min. Four LL reactor plates with differing configurations of spacing between LLMs were compared extensively by analyzing pressure drop and RTD. Plates with continuous or equally-spaced LLMs demonstrated a near plug-flow profile with minor dispersion (Pe > 100), albeit at a greater power dissipation. Plates with longer residence-time channels between LLMs yielded a broader and right-skewed RTD due to the intermittent attenuation of chaotic flow patterns.

Keywords: CFD, LL mixing module, Microreactor, RTD, Turbulence modelling

2.1. Introduction

The use of microreactors in the synthesis of fine chemicals and pharmaceuticals offers several advantages over solvent-intensive batch and semi-batch processes, which has made them an attractive technology for process development and intensification in these industries. Designing continuous-flow microreactors with micro-scale characteristic transport dimensions can mitigate negative environmental impacts due to their higher volumetric productivity. By conferring shorter diffusion paths and promoting more intimate contact between reactants, these miniaturized units maintain higher heat and mass transfer rates, which in turn permit improved reaction control and selectivity at more severe operating conditions. Microreactors also offer safer handling of hazardous materials and unstable intermediates via shorter residence times, lower fluid inventory, and more controlled operating conditions. [4–6, 58]

Scaling up microreactors by increasing the characteristic dimensions presents obvious drawbacks given that their enhanced transport rates become diminished if the characteristic lengths are increased for higher throughput. Alternatively, one can implement both scale-up and scale-out, whereby flow regimes and equivalent power dissipation are maintained across scales and flow rates (e.g., 1–600 g/min for clinical trials), and the units can subsequently be parallelized. Since microreactors are typically modular, this approach facilitates scale-up once optimal process configuration and operating conditions are identified. [1, 12–15]

The geometry of a mixer is often designed to generate macro-scale secondary flow patterns and advective transport. For example, (LL) mixing modules (9.22 × 5 × 1.25 mm; Figure 2.1E) passively generate mixing using a rhombus obstacle, curvature, and an expansion/contraction geometry that serve to change the direction and magnitude of the velocity field. The LL module (LLM) was chosen in this CFD study because it is part of Lonza's toolbox of custom-design commercial microreactors. Although they were originally designed for fluid-fluid reactions, the LL microreactors can also be useful for undertaking fast single-phase liquid reactions in which the overall rate of production is mass-transfer limited. As such, the effectiveness of the LLM as a venturi-like split-and-recombine micromixer, particularly for undertaking fast single-phase reactions, was sought. [1, 12, 16–18]

The application of computational fluid dynamics (CFD) as a tool for microreactor design and optimization has garnered much attention in recent years. The motivation behind developing CFD models is that, upon validation in comparison to experimental data, they allow for the prediction of fluid dynamics and associated transport processes in various systems. Local velocity, pressure, and species concentration profiles are particularly important for reactor development because they provide information about the behaviour inside the reactor that is impractical to deduce experimentally. By developing robust and comprehensive models that predict fluid flow in microreactors, these systems can be optimized and scaled up without having to perform hazardous and/or costly experiments. Although CFD modelling has been applied to microreactor design previously, few publications have employed turbulence modelling in complex microstructures, and less have aimed to use low-Re turbulence models to properly mimic chaotic advection.[15, 37–41]

Thus, following experimental work on liquid and liquid-liquid reactor development [16–18, 57], the present study aimed to develop a mathematical model for predicting incompressible flow and transport of a passive scalar in continuous LL microreactors using CFD. The CFD model was validated by comparison to experimental pressure drop and residence time distribution (RTD) data at flow rates ranging from 10 to 100 g/min. The validation was completed for four configurations of LL microreactors (Figure 2.1A-D): LL-minimal (LL4351), LL-grouped (LL4341), LL-equally-spaced (LL4361), and LL-continuous (LL4381). Each reactor variation shares the same base mixing unit—the LLM with a rhombus obstacle—but contains a different number of LLMs and different spacing between LLMs. As such, the accuracy and robustness of the model in transitioning between flow regimes within a given reactor (i.e., turbulent flow at high flow rates in the LLM and laminar flow in the microchannels) was further validated by performing simulations for all four configurations. Following CFD model validation, local velocity, pressure, and turbulent viscosity fields were analyzed in the repeating segments of the reactor. All CFD simulations were carried out using the open-source software OpenFOAM (field operation and manipulation) [56].

2.2. Methodology

2.2.1. Microreactor geometries

Four different microreactor plates were modelled using AutoCAD, each comprised of a serpentine channel containing several LLMs configured with different spacing. The LL plates had a dimension of 210 × 148 × 5 mm and were manufactured according to specifications in Table 2.1. Each serpentine channel is 2.35 m in axial length and the hydraulic diameter at the smallest cross-section in an LLM (0.5 × 1.25 mm) is 0.71 mm. The LL-continuous plate is uniform in depth (1.25 mm), whereas the other plates have a change in depth from 1.25 mm in the mixing regions to 2 mm in the straight spacing segments.

Table 2.1. LL microreactor dimensions

LL Plate #	Mixing Configuration	Depth (mm)	Number of LLMs	Volume (mL)	
				Manufactured	Modelled
LL4351	Minimal	1.25–2	46	22.2	22.9
LL4341	Grouped	1.25–2	86	18.8	20.2
LL4361	Equally-spaced	1.25–2	86	19.5	20.4
LL4381	Continuous	1.25	234	10.3	11.5

The geometry of each LL reactor is shown in Figure 2.1. The colour-coded regions represent repeating segments that were simulated independently—R1 (red), R2 (yellow), R3 (green), R4 (cyan), R5 (blue), and R6 (magenta)—whereas non-coloured regions were excluded from the simulation to reduce computational requirements. A continuous mixing region (R1) at the start and midpoint of the plate is common to all configurations. The other repeating segments (R2–R6) are residence-time regions (RTR)—comprised of an obstacle followed by a residence-time channel (RTC). Each RTR is bounded by a hydraulic expansion at the start of the channel and a hydraulic contraction at the end. The expansions and contractions were manufactured as gradual changes in depth but were modelled in AutoCAD as straight jumps of equivalent volume to simplify the computational mesh.

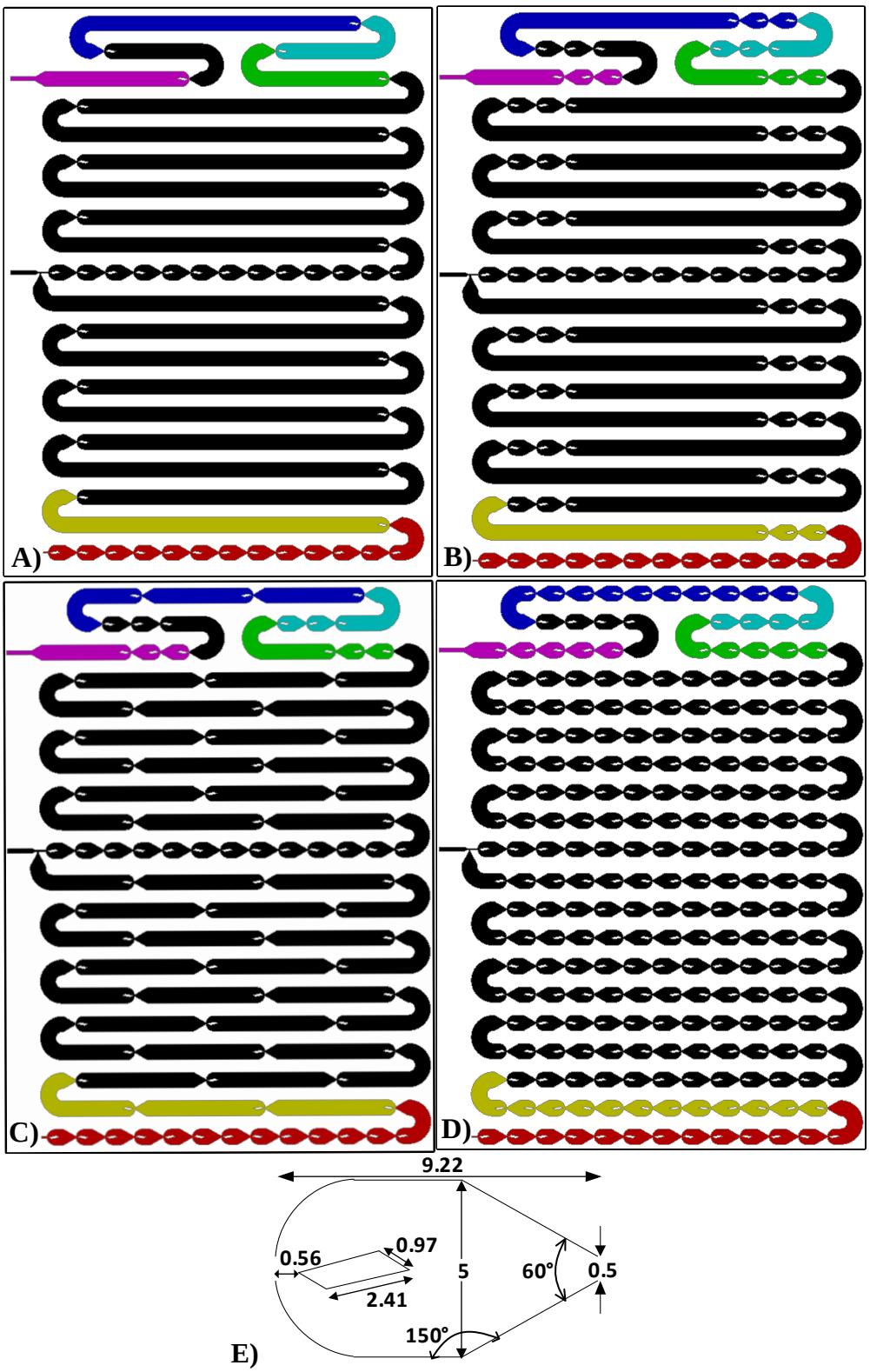

Figure 2.1. LL microreactor configurations: (A) LL4351-minimal, (B) LL4341-grouped, (C) LL4361 equally-spaced, and (D) LL4381-continuous. The colour-coded regions are repeating segments that were simulated independently: R1 (red), R2 (yellow), R3 (green), R4 (cyan), R5 (blue), and R6 (magenta). (E) LLM dimensions in mm (direction of flow is left to right)

2.2.2. Governing equations

2.2.2.1. Reynolds-averaged Navier-Stokes equations and turbulence modelling

The equations required to simulate single-phase flow of an incompressible Newtonian fluid under isothermal conditions are the continuity equation (Equation (2.1)) and the conservation of linear momentum equation (Equation (2.2)). For simulation of turbulent flows, these equations are usually Reynolds-averaged and solved for the mean velocity and pressure fields as follows:

$$\nabla \cdot \overline{\mathbf{U}} = 0 \tag{2.1}$$

$$\rho \frac{D\overline{\mathbf{U}}}{Dt} = \rho \left(\frac{\partial \overline{\mathbf{U}}}{\partial t} + \overline{\mathbf{U}} \cdot \nabla \overline{\mathbf{U}} \right) = -\nabla \bar{P} + \rho \mathbf{g} + + \nabla \cdot \mu [\nabla \overline{\mathbf{U}} + (\nabla \overline{\mathbf{U}})^T] - \nabla \cdot \left(\rho \, \overline{\mathbf{U}' \, \mathbf{U}'} \right) \tag{2.2}$$

where ρ denotes the density of the fluid (kg/m^3), $\nabla \bar{P}$ is the mean pressure gradient (Pa), $\nabla \overline{\boldsymbol{U}}$ and $(\nabla \overline{\mathbf{U}})^T$ are the mean velocity gradient and its transpose (s^{-1}), $\mathbf{g}$ is the gravity vector (m/s^2), μ is the dynamic viscosity of the fluid (Pa·s), $\overline{\mathbf{U}}$ is the mean velocity vector, and $\mathbf{U}'$ is the velocity fluctuation (m/s).

Since energy and momentum are subjected to small-scale temporal and spatial variations in turbulent flow, Reynolds averaging eliminates the need to use very fine computational grids and small time steps that would otherwise be required to resolve these high-frequency variations in time and space [59, 60]. However, the last term on the right-hand side of the Reynolds-averaged Navier-Stokes equation (Equation (2.2)) contains a nonlinear term known as the Reynolds stress $-\rho \, \overline{\mathbf{U}' \, \mathbf{U}'}$. Since this term contains the fluctuating velocity, it cannot be calculated directly. Therefore, a turbulence model must be adopted to relate this term to the mean properties of the flow. Conventionally, the Boussinesq hypothesis is used to define the Reynolds stress in terms of the strain tensor and a turbulent viscosity [59]:

$$\frac{\partial \overline{\mathbf{U}}}{\partial t} + \overline{\mathbf{U}} \cdot \nabla \overline{\mathbf{U}} = -\frac{1}{\rho} \nabla \bar{P} + \mathbf{g} + \nabla \cdot (\nu + \nu_t) [\nabla \overline{\mathbf{U}} + (\nabla \overline{\mathbf{U}})^T] \tag{2.3}$$

where $\nu = \mu / \rho$ is the molecular kinematic viscosity of the fluid (m^2/s), and ν_t is the turbulent kinematic viscosity of the fluid (m^2/s).

A variety of turbulence models are available to predict the turbulent kinematic viscosity [61, 62]. Although the operating flow rates simulated in this study (10–100 g/min) and their

associated Reynolds number at the LLM contraction (214–2140) would yield a laminar flow regime in an equivalent straight channel, the complexity of the LL reactor geometry generates small-scale eddies and flow instabilities via flow separation and vortex shedding around the obstacle. It was concluded in this study that, in the absence of a turbulence model, flow fields became unstable at flow rates above approximately 28 g/min due to the emergence of small-scale fluctuations (Figure B-2.1, Appendix B). After examining velocity and turbulent viscosity fields, as well as comparing pressure drop predictions to experimental results (Figure B-2.2 of Appendix B and Table C-2.1 of Appendix C, respectively), it was concluded that the Langtry-Menter four-equation transitional SST (*k*-ω SSTLM) turbulence model [61–63] was best suited to provide a global solution for incompressible flow in the LL microreactors.

The SSTLM model is based on the *k*-ω SST model with two additional components: a generic infrastructure provided by two transport equations and experimental correlations based on transition regime data [61–63]. The two additional transport equations are for the intermittency (γ_{int}) and the momentum thickness Reynolds number ($Re_{\theta,t}$). The former triggers the transition process by controlling the production of turbulent kinetic energy, while the latter represents a user-defined transition onset criterion. The transport equation associated with $Re_{\theta,t}$ takes a non-local empirical correlation and transforms it into a local quantity that can be compared to the local vorticity Reynolds number (Re_v). At every location where Re_v exceeds $Re_{\theta,t}$, a source term in the intermittency equation is activated and turbulence is produced. This is possible since the intermittency function is coupled to the traditional *k*-ω SST model, which computes the turbulent viscosity (ν_t in m^2/s), turbulent kinetic energy (*k* in m^2/s^2), and turbulent power dissipation (ω in s^{-1}). More information pertaining to the development of the *k*-ω SSTLM turbulence model is described in literature [59, 61–63].

For a developing flow, the inlet value of $Re_{\theta,t}$ can have a significant effect on the results. For the range of conditions used in this study, the inlet value of $Re_{\theta,t}$ was found to have no significant impact ($\sigma < 1\%$) on the pressure drop or mean residence time; however, it did influence the broadness of the dimensionless RTD curve modelled via the Peclet (*Pe*) number (Figure B-2.4, Appendix B). Since the impact of the $Re_{\theta,t}$ inlet value is mainly on the first one or two mixers before the flow becomes fully established, the actual shape of the dimensionless RTD through a long series of mixers was relatively insensitive to the chosen value, as shown in Figure B-2.4D.

Nonetheless, $Re_{\theta,t}$ was slightly tuned to obtain a better fit to experimental RTD data relative to Pe. An $Re_{\theta,t}$ value of 100 was specified for flow simulations at 40 g/min or lower, whereas $Re_{\theta,t}$ was decreased to 50 for higher flow rates in which greater amplitude of recirculation and secondary flow structures characterizing the turbulent regime would occur.

2.2.2.2. Direct numerical simulation

Since the SSTLM model is rarely used for flow predictions in microreactors at relatively low Reynolds numbers, direct numerical simulations (DNS) were performed to further evaluate its performance. The DNS results were obtained for a cyclic geometry involving two of the LLMs shown in Figure 2.1E in series because this represents a repeating unit in the reactors. The DNS data was obtained at flow rates of 20, 50, and 100 g/min. In these simulations, the mesh was specified to maintain a dimensionless wall distance of $y^+ = \frac{\Delta y\sqrt{\nu \nabla_n \mathbf{U}}}{\nu} < 1$, where Δy is the distance from the wall to the first cell center and $\nabla_n \mathbf{U}$ is the velocity gradient normal to the wall. Cells away from the wall in the rest of the domain were at most five times the Kolmogorov length scale [64]. The time-averaged velocity and turbulent kinetic energy fields from DNS were compared to the predictions from the SSTLM model. A comparison of the DNS and SSTLM results for the 100 g/min flow rate is given in section 2.3.1.1, and comparisons for the 20 and 50 g/min flow rates are provided in Figure B-2.3 of Appendix B.

2.2.2.3. Residence time distribution of a passive scalar

The RTD was predicted numerically by simulating the transport of a passive tracer using the advection-diffusion equation:

$$\frac{\partial C_T}{\partial t} + \nabla \cdot (\overline{\mathbf{U}}\, C_T) - \nabla^2 (D_T\, C_T) - \nabla^2 \left(\frac{\nu_t}{Sc_t} C_T\right) = 0 \tag{2.4}$$

where C_T represents the dimensionless tracer concentration; D_T is the molecular diffusion coefficient of the tracer, which was assumed to be 4.2×10^{-10} m^2/s in this study; and Sc_t is the turbulent Schmidt number, which was assumed to be unity in this study.

2.2.3. Numerical approach

OpenFOAM is an open-source platform for CFD simulations and the solution of partial differential equations. In OpenFOAM, the simpleFoam solver is designed to simulate laminar or

turbulent single-phase incompressible steady-state flow and was used in this study for all flow simulations. The simpleFoam solver uses the semi-implicit-method-for-pressure-linked-equations (SIMPLE) algorithm to iteratively solve for the pressure and velocity fields. The transport quantities associated with the turbulence model are computed by solving the selected turbulence model. In the SIMPLE algorithm, the momentum equation (Equation (2.3)) is discretized to obtain an equation for velocity and combined with the continuity equation (Equation (2.1)) to obtain an explicit equation for pressure. The resulting equations are solved iteratively in a segregated manner to converge on the pressure and velocity fields [57, 65, 66]. The simpleFoam solver was used to perform all SSTLM flow simulations in this study. Unlike the SSTLM simulations, DNS requires a transient solution of the flow field. Therefore, the pimpleFoam solver, which uses a combination of the pressure-implicit with splitting of operators (PISO) and SIMPLE algorithms to obtain time-accurate results, was employed for DNS. The DNS results were obtained by solving Equation (2.3) with $\nu_t = 0$.

The transient transport of a passive scalar must be predicted to simulate the RTD. The scalarTransportFoam solver simulates the transport of a passive scalar by solving the advection-diffusion equation (Equation (2.4)). In this study, the solver was renamed to scalarTurbTransportFoam and modified to directly access the turbulent kinematic viscosity determined by the flow simulation. RTD simulations were performed using the converged steady-state velocity field predicted using simpleFoam.

Pressure and velocity fields were solved using the geometric-algebraic multi-grid (GAMG) and the stabilized preconditioned biconjugate gradient (PBiCGStab) solvers, respectively. The latter solver was also used to compute the concentration field in the RTD determination. Turbulence model transport quantities were calculated via smoothSolver, with a symmetric Gauss-Seidel smoother. For steady-state simulations, an under-relaxation factor of 0.3 was used for pressure and 0.5 was used for all other variables to limit oscillations between iterations. No under-relaxation was used for DNS. The scaled residuals for pressure, velocity, and turbulence variables were converged to at least 10^{-4}, and changes in the pressure and velocity fields were monitored to ensure convergence to steady profiles. The scaled residuals for concentration were converged to at least 10^{-8}. The numerical solvers used herein are summarized in Table C-2.2 of Appendix C.

High-order numerical discretization schemes are preferred to minimize artificial diffusion, but they can introduce instability when used in the advection term [66]. Therefore, discretization schemes should be chosen carefully to ensure accuracy and a stable solution, and upwind-weighted schemes are usually used to ensure numerical stability for the advection term. In this study, second-order-accurate schemes were employed for the discretization of all spatial derivatives to minimize artificial diffusion. The second-order accurate Crank-Nicolson time integration scheme was used for DNS and RTD simulations. For DNS, the time step size was chosen to limit the Courant number $Co = \frac{U\Delta t}{\Delta x}$ to at most 0.5. The time step size for the RTD computations was selected so that the RTD was independent of time step size for a given flow rate. The numerical schemes used in this study are summarized in Table C-2.3 of Appendix C.

2.2.4. Computational mesh

The computational domain of the LL microreactors was discretized in a stepwise manner, beginning with the mixing module (Figure 2.2A-B). For the mixing region comprised exclusively of LLMs, 2D unstructured grids were built in the SALOME pre-processing platform by means of a NETGEN 1D-2D algorithm. The mesh was then completed in OpenFOAM by extruding the 2D mesh on the symmetry plane in the depth direction (depth of 1.25 mm with 20 cell layers), where an expansion factor of 1.05 was used from bottom to center plane. The bulk of the LLM 2D grid is composed of triangular cells with a viscous layer of quadrangle cells contouring the walls and obstacle. In 3D, the mesh for one LLM is composed of 145 640 cells and, since it is symmetrical in depth, only the bottom half of the mixing module was modelled and simulated over a symmetry-plane boundary. Mesh quality metrics are as follows: a maximum aspect ratio of 7.6, an average non-orthogonality of 5.7, and a maximum skewness of 1.97. The coarsest mesh for which the pressure drop results were approximately independent of cell size was chosen for all simulations. When validating the 2D resolution of the LLM, the number of faces spanning its 33.06 mm^2 base was varied between 5 804 and 28 806. In addition, the average layer thickness in depth from wall to symmetry plane (0.625 mm) was varied separately between 0.0625 and 0.0156 mm. A tolerance of < 2% was used to analyze mesh independence with respect to pressure drop as well as the first moment of age distribution. It was then concluded that the results were not significantly influenced by higher levels of mesh refinement than 7 282 faces × 20 layers. The minimum and maximum cell sizes in the chosen LLM domain were 2.3×10^{-6} mm^3 and 4.8×10^{-4} mm^3, respectively. The

3D mesh of a RTR is shown in Figure 2.2C-D and further visualization and information pertaining to the 3D mesh of other repeating segments can be found in Figure B-2.5 of Appendix B. The breakdown of the total number of control volumes used in R1–R6 of each reactor is presented in Table C-2.4 of Appendix C. As mentioned in section 2.2.2.2, the mesh for DNS was specified to maintain a dimensionless wall distance of at most 1, and cells away from the wall in the rest of the domain were at most five times the Kolmogorov length scale. No symmetry plane was used for DNS.

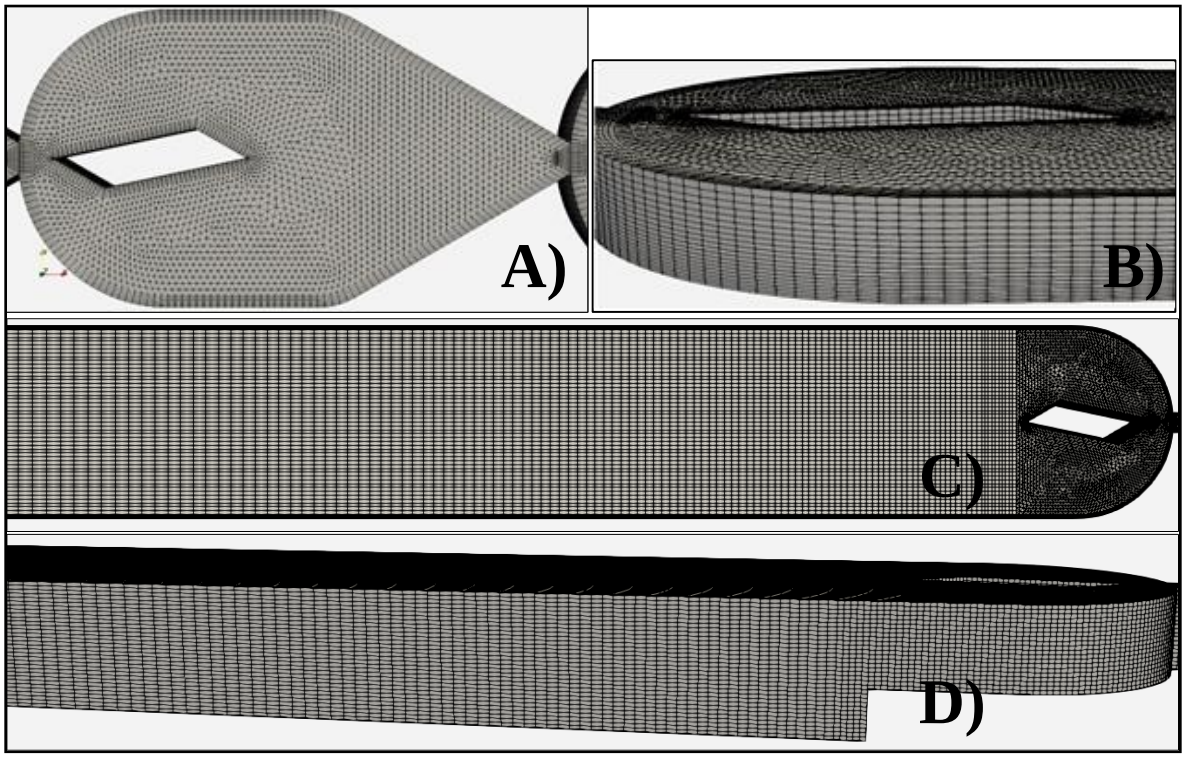

Figure 2.2. Top and side view of the 3D mesh of the LLM composed of 145 640 cells (A and B) and longest RTR composed of 1 409 512 cells (C and D). Direction of flow is left to right for A) and B), and right to left for C) and D)

2.2.5. Boundary conditions

The boundary conditions used in all CFD simulations are summarized in Table C-2.5 of Appendix C. Low-Reynolds-number wall functions were employed for k, ω, and ν_t to modify the shear stress at the wall such that a realistic velocity profile could be modelled. The low-Reynolds-number modifications were incorporated in the model to add effects of molecular viscosity to the diffusion terms and to account for anisotropy in the dissipation rate term [59, 62]. For RTD determination, steady-state velocity and turbulent viscosity fields were used as initial conditions for the transient simulation of passive scalar transport.

2.2.6. Manipulation and analysis of simulation data

CFD simulation results were validated using experimental data collected by Hopley *et al.* [17]. Experimental RTD data was collected via pulse experiments, wherein an optimal concentration of dye was injected at the reactor inlet and probed at the outlet using an optic blue-LED sensor (Ocean Optics, LS-450). Light absorption measurements were read at a wavelength of 460 nm and the average concentration at the outlet plane was computed via a mixing-cup method using integration time intervals of 3 ms, while assuming the absorbance to be linearly proportional to the concentration ($R^2 = 0.9958$). Pressure drop measurements were taken at the inlet and outlet of the reactor using pressure transducers (Wika M-11).

CFD simulations performed in this study were done with operating conditions and physical properties to match experimental conditions. Water flow rates of 10 to 100 g/min were used at ambient temperature; therefore, the kinematic viscosity was specified as 8.92×10^{-7} m^2/s, and the density was assumed to be 997 kg/m^3. The CFD model was validated by comparing pressure drop and RTD predictions to experimental data, particularly for the LL4381 and LL4351 reactor configurations. For computational RTD determination, an inlet pulse of 1.4 ms was chosen such that the concentration variance at the reactor inlet would be as small as possible, but not less than the simulation time step.

Each LL configuration contains six repeating segments, as shown in Figure 2.1, meaning it was possible to simulate flow in these regions separately and subsequently deduce the pressure drop and RTD of the full reactor by convolution. Convolution of several RTD curves in series is a valid approach if the flow fields in consecutive modules are independent of one another, which means the fluid must lose its memory passing from segment to segment [67]. More information pertaining to the manipulation and analysis of RTD data may be found in Appendix A.

2.3. Results and Discussion

2.3.1. Validation of CFD model

The following sections detail the validation of reactor configurations at opposite extrema in terms of macromixing: continuous mixing (LL4381) and minimal mixing (LL4351). Details pertaining to the validation of the LL4341 and LL4361 plates are included in Appendix B and C (Figure B-2.6, Figure B-2.7 and Figure B-2.8; Table C-2.8, Table C-2.9, Table C-2.12, and Table C-2.13).

2.3.1.1. LL4381: Continuous mixing

CFD predictions of pressure drop ($-\Delta P$) in the LL-continuous reactor as a function of flow rate are presented in Figure 2.3 and are overlapped by experimental data points. A numerical comparison is summarized in Table C-2.6 of Appendix C. The modelled trend is in clear conformance to experimental pressure loss measurements, wherein the latter fits the CFD model to an R^2 of 0.997 over eight data points.

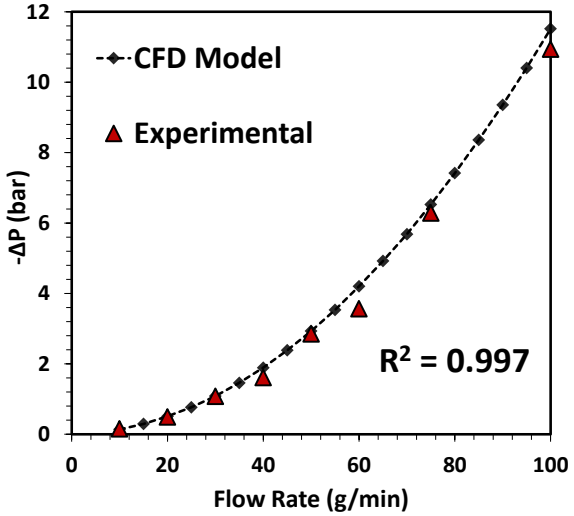

Figure 2.3. Validation of pressure drop predictions in LL4381 as a function of flow rate

CFD predictions of the RTD were also validated against experimental results, which are available at flow rates ranging from 15 to 95 g/min for all four LL reactors except the LL-continuous, whose RTD was determined experimentally up to 55 g/min. The RTD curves for the LL-continuous are shown in Figure 2.4 and are normalized with respect to the mean residence time ($\bar{t}$), such that E_θ is the dimensionless RTD and θ is the dimensionless time. The experimental data was fit to a deterministic axial dispersion (AD) model that is known to adequately represent the

RTD of flow patterns showing slight deviations from plug flow [67], as demonstrated by systems with co-existing turbulent and laminar regions such as packed beds [68] and micromixers [69]. At flow rates of 35 and 55 g/min (Figure 2.4B-C), the modelled E_θ curves line up impeccably with the experimental curves ($R^2 > 0.99$). At 15 g/min (Figure 2.4A), they are also in good agreement with one another ($R^2 = 0.979$), with slightly more scatter near the peak due to experimental background noise. The numerical validation of the LL4381 RTD predictions is expanded upon in more detail, with respect to the mean residence time and variance, in Table C-2.10 of Appendix C. Figure 2.4D compares the dimensionless RTD curves of the LL4381 at all simulated flow rates. At 35 g/min and higher, the RTD is symmetrical and fits to an AD model very well with $R^2 > 0.99$. A sharp increase in peak is observed from 35 to 55 g/min. However, the RTD at 55, 75, and 95 g/min are virtually identical, indicating that the relative degree of fluid bypassing and recirculation is constant above 55 g/min.

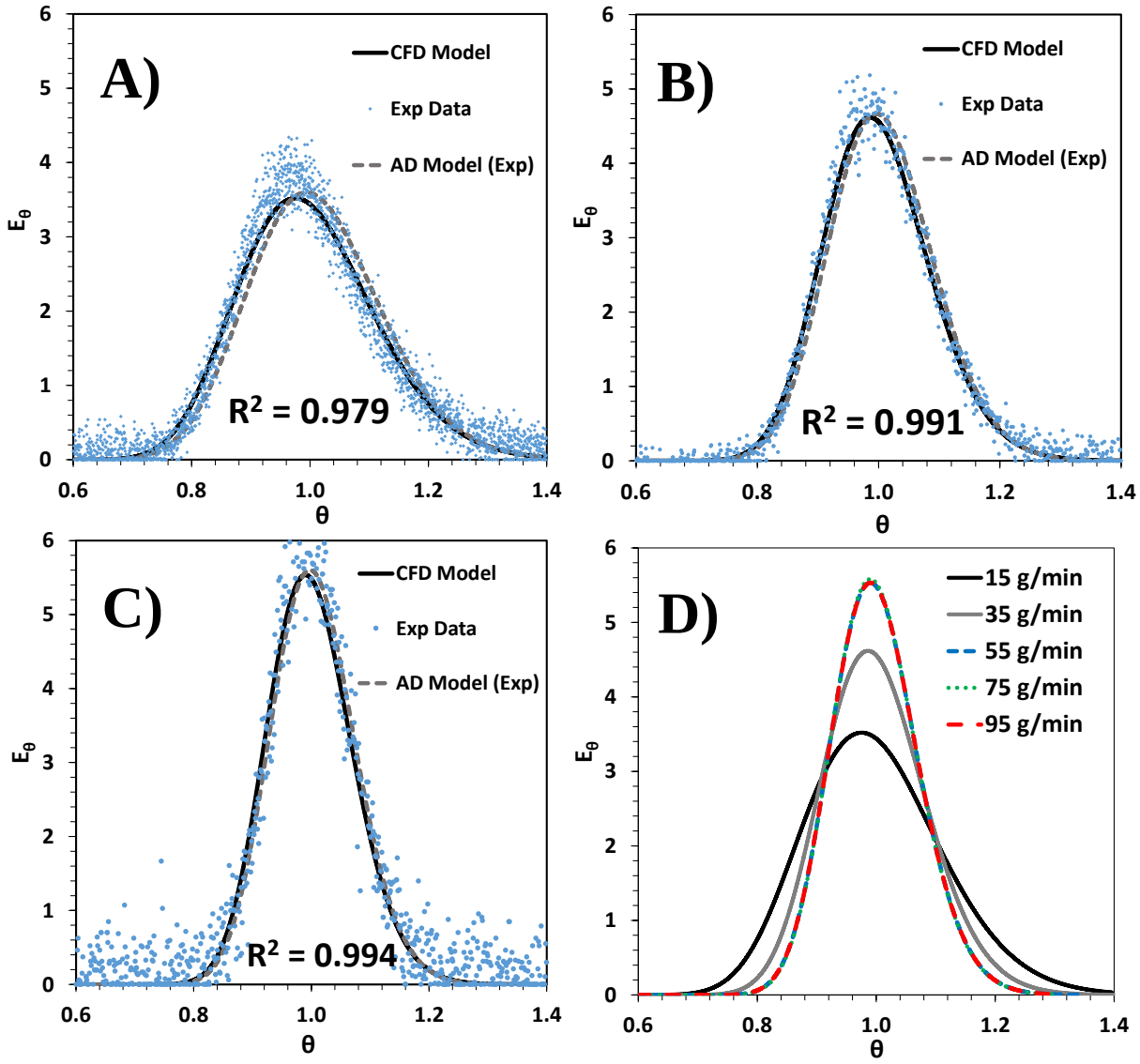

Figure 2.4. Validation of macromixing performance in LL4381 via dimensionless RTD (E_θ) predictions at flow rates (g/min) of A) 15, B) 35, C) 55, and D) all

The time-averaged velocity and turbulent kinetic energy fields from DNS are compared to the steady-state SSTLM results in Figure 2.5 for a flow rate of 100 g/min. In both cases, the results were obtained for a cyclic geometry involving two of the LLMs in series. A comparison of the DNS and SSTLM results for the time-averaged velocity and turbulent kinetic energy fields for the 20 and 50 g/min flow rates is provided in Figure B-2.3 of Appendix B. The pressure drop predictions using DNS and SSTLM for 20, 50, and 100 g/min were within 12, 11, and 6 %, respectively, with the DNS prediction being higher in all cases. Figure 2.5 shows that there is good general agreement between the time-averaged velocity fields obtained from the SSTLM model and DNS for the 100 g/min flow rate, both in terms of the peak velocity and the size of the recirculation

zones. Similarly, there is also good general agreement between the turbulent kinetic energy fields obtained from the SSTLM model and DNS, although the predicted peak values are slightly higher from DNS. The instantaneous velocity profile obtained from DNS shows the presence of a high level of chaotic mixing for a flow rate of 100 g/min.

The comparison of the time-averaged velocity fields for the 20 and 50 g/min flow rates provided in Figure B-2.3 shows good general agreement in terms of the peak velocity and level of recirculation. However, although the scales of the turbulent kinetic energy predictions match relatively well for the 50 g/min flow rate, the SSTLM results show an overprediction of the peak value relative to DNS, particularly at the leading edges of the obstacle. The instantaneous velocity profile indicates that this is due to the flow becoming less chaotic at these lower flow rates. Furthermore, the 20 g/min SSTLM predictions of turbulent kinetic energy show an even greater overprediction relative to DNS. This is likely due to the flow becoming even less chaotic at this low flow rate, as shown in the instantaneous velocity field. However, as shown in Figure 2.8, the SSTLM model predicted negligible turbulent kinematic viscosity at 10 g/min. Therefore, the SSTLM model appears to provide good predictions of turbulence levels at low and high flow rates, but more deviation is expected in the intermediate range of flow rates where the flow transitions from laminar to turbulent.

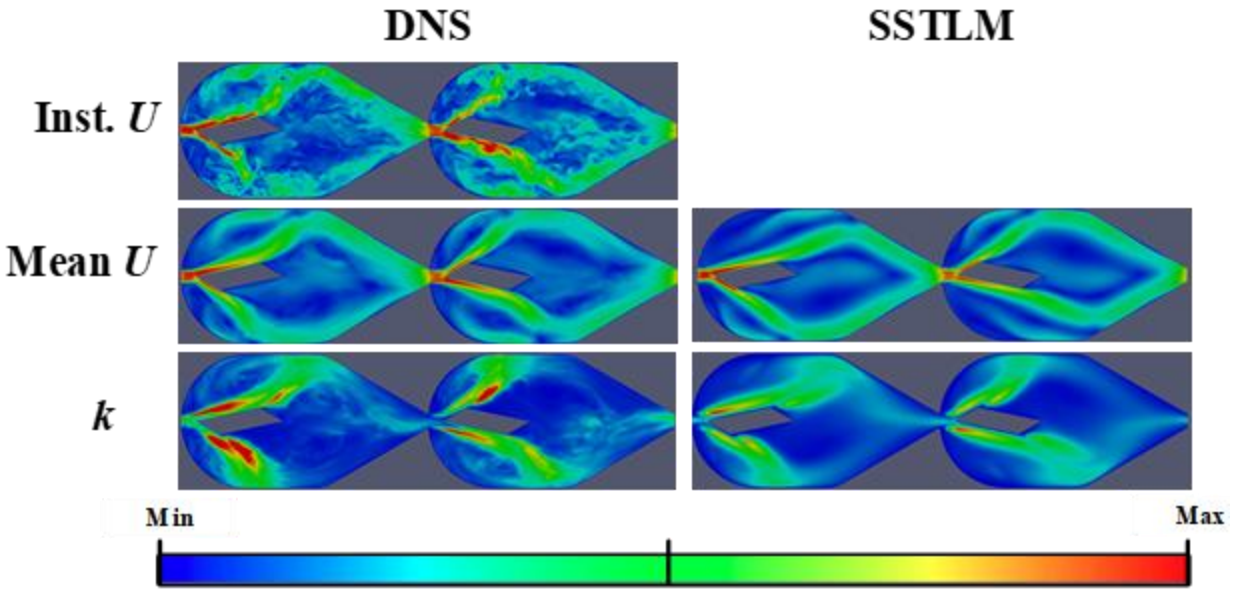

Figure 2.5. 2D colour plots of velocity magnitude and turbulent kinetic energy over the center plane (z = 0.625 mm) for a flow rate of 100 g/min obtained using SSTLM (right) and DNS (left). U_{min} = 0 (blue) and U_{max} = 3.5 m/s (red). k_{min} = 0 (blue) and k_{max} = 0.75 m^2/s^2 (red). DNS results were time averaged over 0.025 s. Direction of flow is from left to right

2.3.1.2. LL4351: Minimal mixing

A similar comparison approach, described previously for the LL4381, was also undertaken for validating CFD results obtained in the minimal-mixing configuration (LL4351). Graphical comparisons of CFD pressure loss predictions to experimental measurements in the LL4351 are shown in Figure B-2.9 of Appendix B for flow rates ranging from 10 to 150 g/min, while numerical comparisons are summarized in Table C-2.7 of Appendix C.

Figure 2.6A-E shows the validation of RTD results in the LL-minimal at flow rates ranging from 15 to 95 g/min. As was the case in the LL4381, the CFD predictions are valid throughout this range, with $R^2 > 0.992$ at every flow rate. A detailed numerical validation of RTD predictions in the LL4351 is summarized in Table C-2.11 of Appendix C. The mean residence time predicted through CFD ($\bar{t}$) is slightly lower than the space residence time (τ) from 15-55 g/min, yet greater at higher flow rates. This delayed exit of fluid at higher flow rates is due to the presence of recirculation zones of greater amplitude, whereas at low flow rates, the presence of recirculation and secondary flow patterns are not enough to offset fluid bypassing. Figure 2.6F compares the dimensionless RTD curves of the LL4351 simulated at all five flow rates used in the validation. An AD model could not be fit to any of the RTD curves generated in the LL-minimal due to the lack of a plug-flow profile caused by the near-parabolic velocity profile in the RTC [67]. Back-end tailing is observed at each flow rate, most notably at 15 g/min, which is reasonable given that there are more RTCs than mixing regions in this configuration.

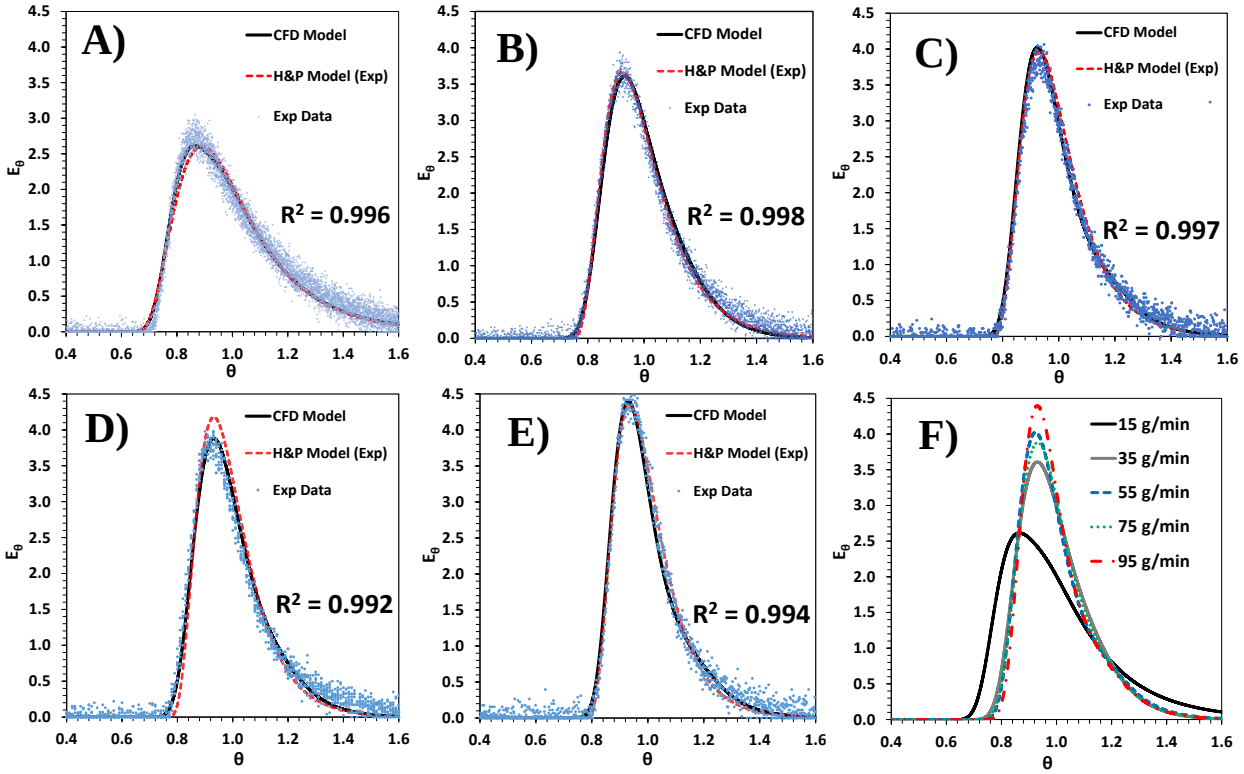

Figure 2.6. Validation of macromixing performance in LL4351 via dimensionless RTD (E_θ) predictions at flow rates (g/min) of A) 15, B) 35, C) 55, D) 75, E) 95, and F) all

2.3.2. Local characterization of fluid dynamics

Simulations were completed through a geometry comprised of 13 LLMs in series (i.e., the mixing region common to each LL configuration) in order to determine the number of modules needed to establish fully developed flow. The velocity in the axial direction (U_x) was taken at four different points within the LLM across several modules for flow rates of 10, 50, and 100 g/min (Figure 2.7). Since the orientation of the mixing obstacle is axially flipped by 180° at every repeating module, the position of certain probes needed to be flipped accordingly. It was found that the velocity at each point remained constant from module to module, only with slight differences encountered in the first LLM. In this first module, the maximum velocity (i.e., the centerline velocity at the LLM contraction) was 48%, 29% and 21% greater than the steady value for flow rates of 10, 50 and 100 g/min, respectively. Upon attaining a fully developed profile, the deviation in velocity data from module to module drops below 2%. Moreover, the pressure drop was also computed through several LLMs in series and was found to be constant (deviation less than 0.5%) after the first module (Table 2.2). Thus, fully developed flow appears to be established

in the second LLM in series; wherein all subsequent modules behave identically. An alternative steady-state analysis is presented in the Supporting Information with respect to turbulent viscosity (Figure B-2.11) and as a function of depth (Figure B-2.10), in order to support this notion.

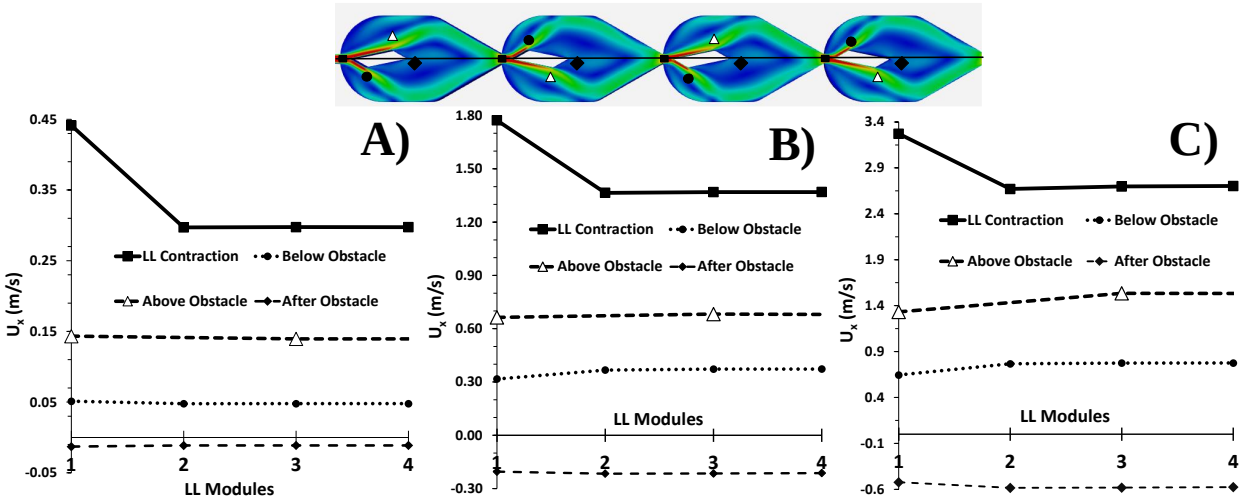

Figure 2.7. Local velocity computations at four locations inside the LLM for several modules in series at flow rates (g/min) of A) 10, B) 50, and C) 100. Velocity taken at center-plane depth (z = 0.625 mm) and direction of flow is left to right

Table 2.2. Pressure drop predictions through several LLM in series

Q	**-ΔP (kPa) per LLM**					
(g/min)	1	2	3	4	5	6
10	0.038	0.058	0.058	0.058	0.058	0.058
50	0.724	1.246	1.244	1.245	1.245	1.246
100	2.742	4.899	4.887	4.893	4.897	4.899

Figure 2.8 displays the fully-developed 2D velocity profiles within a single LLM at center-plane depth (z = 0.625 mm) as a function of flow rate. The maximum velocity is always achieved at the contraction of the module: at 10 g/min, U_{max} = 0.335 m/s and at 100 g/min, U_{max} = 3.41 m/s. At both extrema, the maximum velocity is roughly 28% greater than the average velocity at the contraction—the latter of which represents the planar initial condition value of the steady-state simulation. 2D streamlines were superimposed over the velocity profiles to show advective recirculation. A similar streamline pattern is observed at each flow rate: the liquid encounters the rhombus obstacle and splits into two streams. Both stream channels within the LLM maintain a

velocity magnitude of about half the maximum velocity, before eventually reuniting at the contraction of the next module. A small recirculation zone behind the obstacle begins to form at 20 g/min, and turbulent diffusion also begins to appear at this flow rate. At 30 g/min, three recirculation zones are observed behind the obstacle: two in between the bypass streams and one at the top wall. At 50 g/min, the latter moves closer to the obstacle, yielding two recirculation zones in the center of the module behind the obstacle and another two adjacent to the obstacle walls. The 3D depiction of streamlines indicates that the recirculation zones are non-uniform in depth, where the amplitude of these zones is greater at the center plane than it is closer to the bottom wall. The relative size of the four main recirculation zones is roughly the same from 50 to 100 g/min. Overall, stagnant fluid located at the center of the recirculation zones occupies roughly 5% and 10% of the total LLM volume at 20 and 100 g/min, respectively.

The turbulent viscosity, which is indicative of mass transport due to time-averaged fluctuations in turbulent flow, increases with flow rate. At 10 g/min, a purely laminar regime is evident given that the turbulent viscosity is effectively 0 and there are no recirculation zones of considerable amplitude. At 20 g/min, much of the LLM is devoid of turbulent flow patterns, and the turbulent viscosity is mostly of less or equal magnitude to the molecular viscosity (10^{-6} m^2/s). As flow rate is further increased, the turbulent dissipation grows stronger, and above 50 g/min, it is at least an order of magnitude greater than the molecular viscosity at any given point.

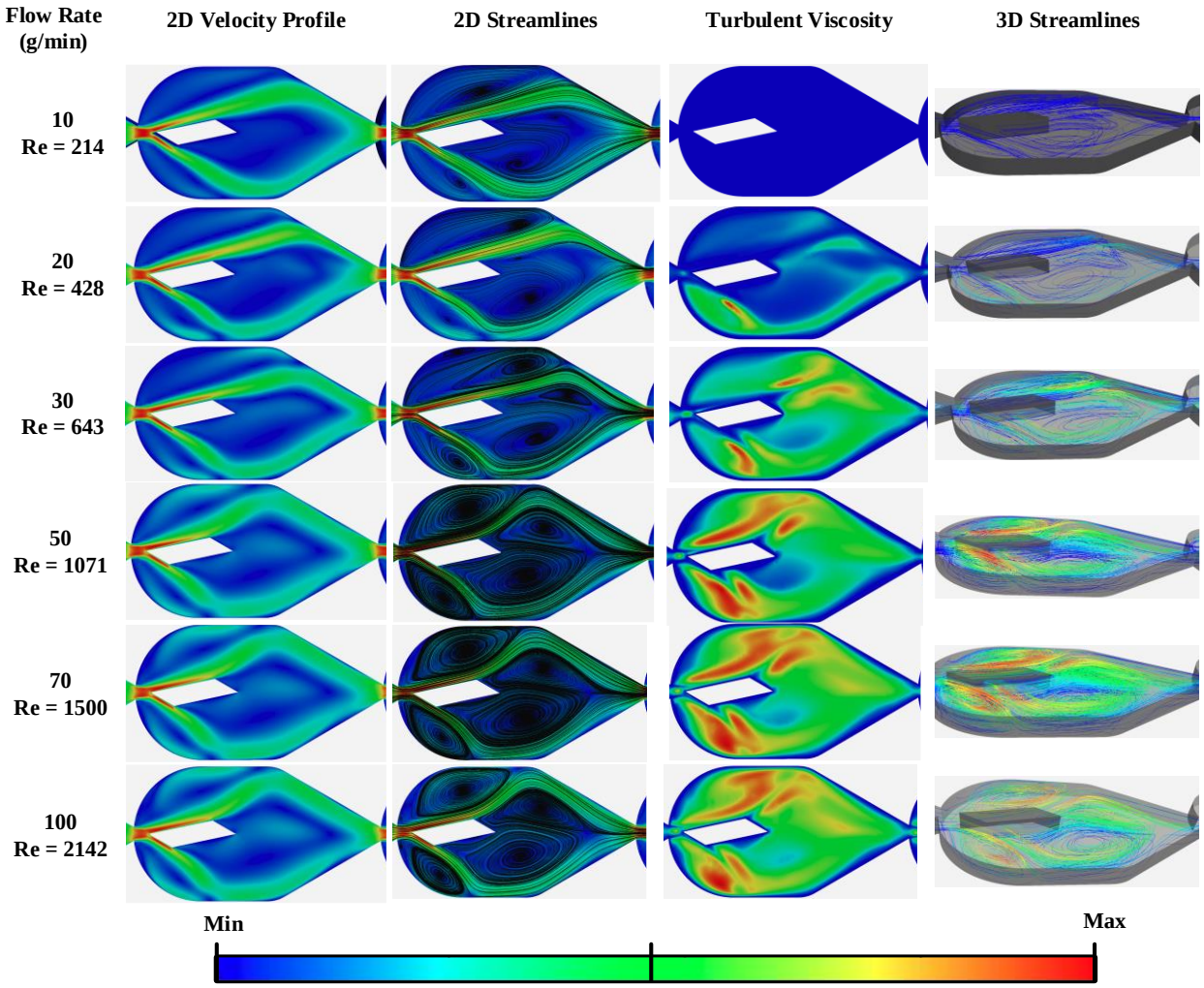

Figure 2.8. Velocity magnitude profiles, streamlines, and turbulent viscosity fields in the LLM at symmetry plane (z = 0.625 mm). U_{min} = 0 (blue) for each flow rate, whereas U_{max} (red) varies as follows (m/s): 0.335 (10 g/min), 0.676 (20 g/min), 1.00 (30 g/min), 1.67 m/s (50 g/min), 2.36 (70 g/min) and 3.41 (100 g/min). The turbulent viscosity (m^2/s) is also scaled, wherein $\nu_{t,min}$ = 0 (blue) for each flow rate and $\nu_{t,max}$ (red) varies as follows (m^2/s): 0 (10 g/min), 2×10^{-6} (20 g/min), 7×10^{-6} (30 g/min), 2.0×10^{-5} (50 g/min), 2.4×10^{-5} (70 g/min), and 3.0×10^{-5} (100 g/min). 3D streamlines are coloured according to turbulent viscosity

The dimensionless RTDs of the LLM as a function of flow rate are shown in Figure 2.9 along with a non-ideal flow model used to fit the high-flow curves. The latter is comprised of a) a time delay at $\theta < 0.18$ (breakthrough time), b) two AD models that represent the bypass streams (Pe >500), and c) a perfectly mixed system with a 50% bypass at $\theta > 0.46$. At each flow rate simulated in the LLM, two peaks are observed between $0.2 < \theta < 0.4$, which represent the two bypass streamlines that flow around the obstacle. The asymmetry of the obstacle causes one streamline to reach the outlet faster than the other, causing the generation of two distinct peaks. At lower flow rates, the peaks corresponding to the streamlines appear to be sharper because there is

significantly less recirculation to counteract the streamlining of the tracer. Between $0.6 < \theta < 2$, more peaks appear in the RTD. This can likely be attributed to the tracer entering and subsequently leaving different recirculation zones, which causes a delayed arrival of the tracer. This notion would explain why these peaks are not noticeable at 10 g/min, why they begin to develop at 30 g/min, and why they are distinguishable at 50 g/min and higher.

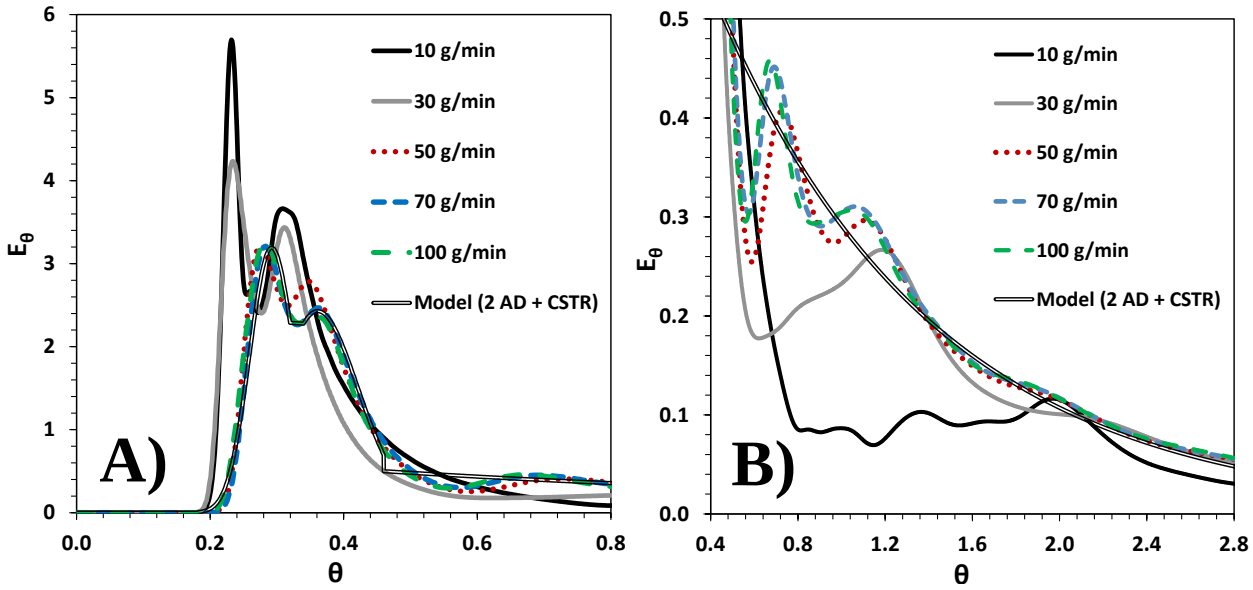

Figure 2.9. Dimensionless RTD (E_θ) of a double-AD model (Pe > 500) + perfectly-mixed CSTR in comparison to a single LLM at different flow rates (g/min): 10 (black), 30 (grey), 50 (red), 70 (blue), and 100 (green). (A) $0 < \theta < 0.8$; (B) $0.4 < \theta < 2.8$

Figure 2.11 plots the pressure drop across a single LLM as a function of flow rate. The 19 data points were fit to a power law in order to quantify the degree of turbulence based on the exponent value. As mentioned, the Reynolds number computed at the smallest cross-section of the LLM would suggest a laminar flow regime in an equivalent straight channel at flow rates below 90 g/min (Re < 2000). However, a nonlinear dependence modelled by a power law of $-\Delta P = Q^{1.933}$ is conferred. The non-linearity of this correlation confirms the presence of chaotic secondary flow patterns in the majority of the LLM at flow rates greater than 30 g/min (Re > 643), as shown in Figure 2.8. Frictional losses through the mixing module can thus be attributed to a) expansion/contraction, b) recirculation dissipation, and c) flow separation around the sharp obstacle. It should also be noted that the "critical" Reynolds number (Re_c) at which chaotic eddies begin to emerge in the LL is roughly 600, which corresponds to a flow rate of 28 g/min. This value was first deduced by the fact that, in the absence of a RANS turbulence model, simulations did not

reach steady state above 28 g/min due to the presence of temporal fluctuations in the velocity profile around the obstacle (Figure B-2.1 of Appendix B). The critical value was then confirmed by determining that the turbulent viscosity exceeds the molecular viscosity everywhere in the LLM at 30 g/min and above. Several authors have reported Re_c values in this same range for incompressible flow in micromixers that induce passive mixing, such as Wu (Re_c = 350–900) [70], Peng *et al.* (Re_c = 200-700) [71], and Mala and Li (Re_c = 300–900) [72]. As a result, other CFD studies completed in micromixers have also utilized turbulence modelling to model fluid dynamics at Re < 2000 since there is often a co-existence of laminar and turbulent regions in these types of systems [39, 73].

The residence-time region is comprised of a rhombus obstacle, followed by a straight residence-time channel (RTC). The latter contains a hydraulic expansion at the start and a hydraulic contraction at the end of the channel. The purpose of adding RTCs between mixing regions—as employed in three of the four LL configurations—is to gain reaction volume (i.e., residence time) without the excessive power dissipation conferred by the LLM. However, too long of an RTC without mixing modules leads to the attenuation of chaotic secondary flow patterns generated by passive mixing elements, which compromises the degree of advective mixing and overall transport performance of the reactor. Thus, an estimate of the optimal spacer length was sought. Figure 2.10 displays the turbulent viscosity and velocity profile through the RTR of the LL4351 at flow rates of 10, 50, and 100 g/min. As seen in the LLM, at the lowest flow rate, the turbulent viscosity is effectively zero and velocity streamlines suggest a unidirectional laminar regime with little recirculation. Above 50 g/min, turbulent dissipation extends into the straight channel and recirculation zones form adjacent to the obstacle. However, even at 100 g/min, the turbulent flow patterns attenuate well before the exit.

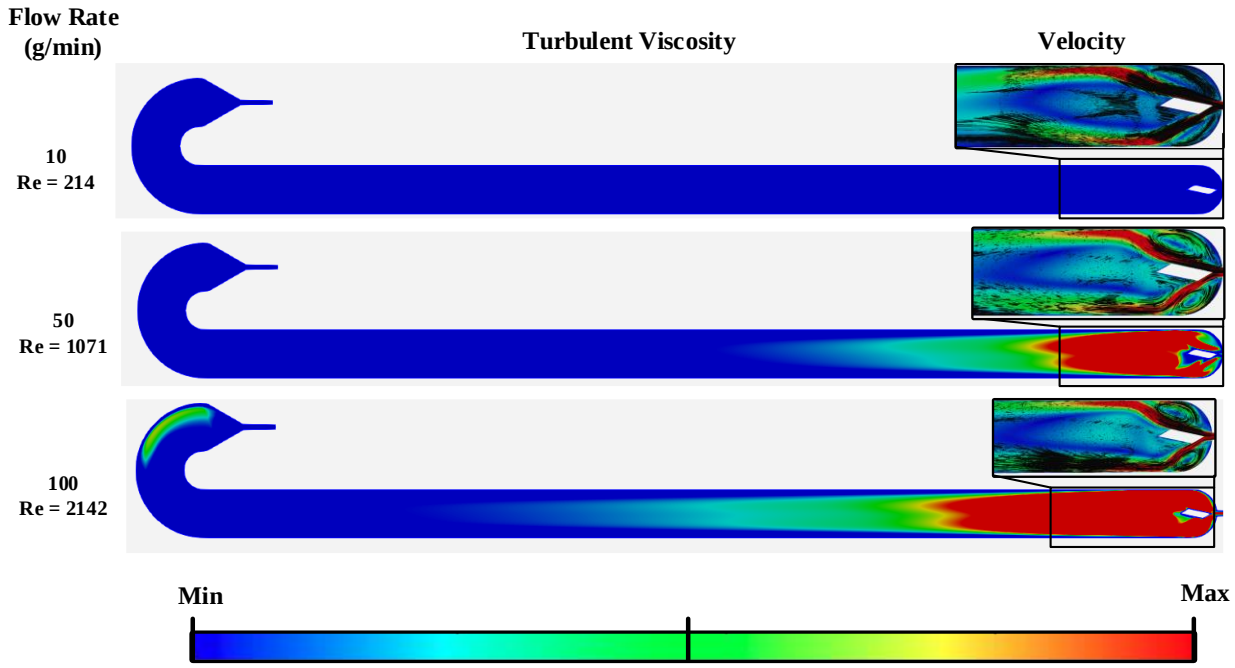

Figure 2.10. Turbulent viscosity and velocity fields in RTR of LL4351 (direction of flow is right to left). U_{min} = 0 (blue) for each flow rate, whereas U_{max} (red) varies as follows (m/s): 0.335 (10 g/min), 1.67 m/s (50 g/min), and 3.41 (100 g/min). The turbulent viscosity is also scaled, wherein $\nu_{t,min} = 8 \times 10^{-7}$ m^2/s (blue) and $\nu_{t.max} = 4 \times 10^{-6}$ m^2/s (red) for each flow rate

It should be noted that the pressure drop curves of the LLM and longest RTR (LL4351) are comparable because pressure loss is mostly attributed to flow separation, recirculation around the obstacle, and the sudden contraction. Negligible frictional losses occur in the RTC, which is confirmed by the fact that the RTR in the LL4351 and LL4341 confer virtually the same pressure drop, even though the former is 12% longer than the latter. In fact, a greater pressure loss is computed in the LLM compared to the RTR at flow rates greater than 30 g/min because a) there is greater recirculation dissipation in the LLM compared to the RTR since the former yields four recirculation zones while the latter confers two smaller ones; and b) the streamlining into the contraction is turbulent in the LLM and laminar in the RTR. Streamlines for key parts of the hydraulic regions are shown in Figure B-2.12 of Appendix B and the RTD of the LL4351 RTR as a function of flow rate is shown in Figure B-2.13.

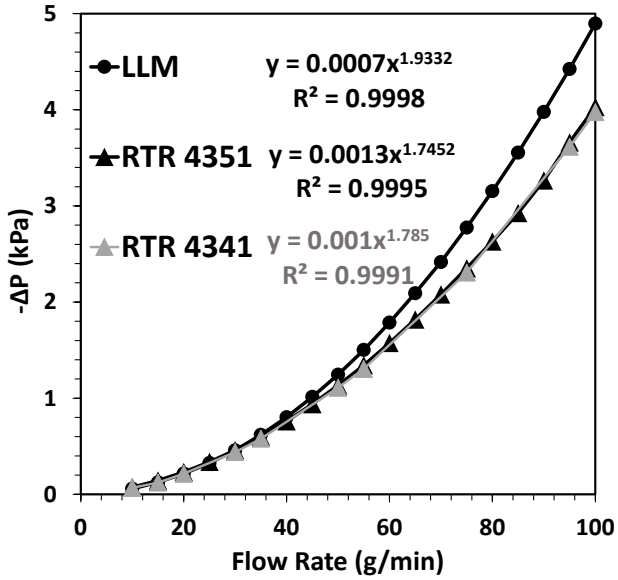

Figure 2.11. Comparison of pressure drop in the LLM, the RTR of the LL4351, and the RTR of the LL4341 (grey), as a function of flow rate

The final objective with respect to the RTR was to estimate the fluid dynamic entrance length downstream of the mixing region at different flow rates, which represents the axial distance travelled prior to redeveloping a laminar flow regime. Existing empirical correlations developed by Han [74], Costaschuk *et al.* [75], and Kockmann [58] would suggest that the entrance length in laminar flow through a rectangular microchannel can be estimated via Equation (2.5), (2.6) and (2.7), respectively:

$$\Delta x_{ent} = 0.06 \cdot d_h \cdot Re \tag{2.5}$$

$$\Delta x_{ent} = d_h(0.026 \cdot Re + 10.7) \tag{2.6}$$

$$\Delta x_{ent} = d_h\left(\frac{0.89}{1+0.1843 \cdot Re} + 0.164 \cdot Re\right); 10 < \frac{\Delta x_{ent}}{d_h} < 60 \tag{2.7}$$

where Δx_{ent} is the entrance length and d_h is the hydraulic diameter.

The optimal RTC length was also estimated via CFD simulations by means of two different methods: a) by computing the distance after which the turbulent viscosity is less than the molecular viscosity of water (Figure 2.12A); and b) by plotting the axial velocity profile through the channel and locating the distance after which the maximum velocity plateaus (Figure 2.12B). The former shows that the turbulent viscosity effectively attenuates to less than the molecular viscosity as flow

moves deeper into the RTC. On the other hand, the centerline axial velocity profile shows that, once passed the recirculation zone behind the obstacle (shown as a negative U_x), the fluid reaches its maximum velocity once its flow pattern is fully developed. Entrance length values estimated through CFD were then compared against values obtained via the empirical correlations, which are summarized in Table 2.3.

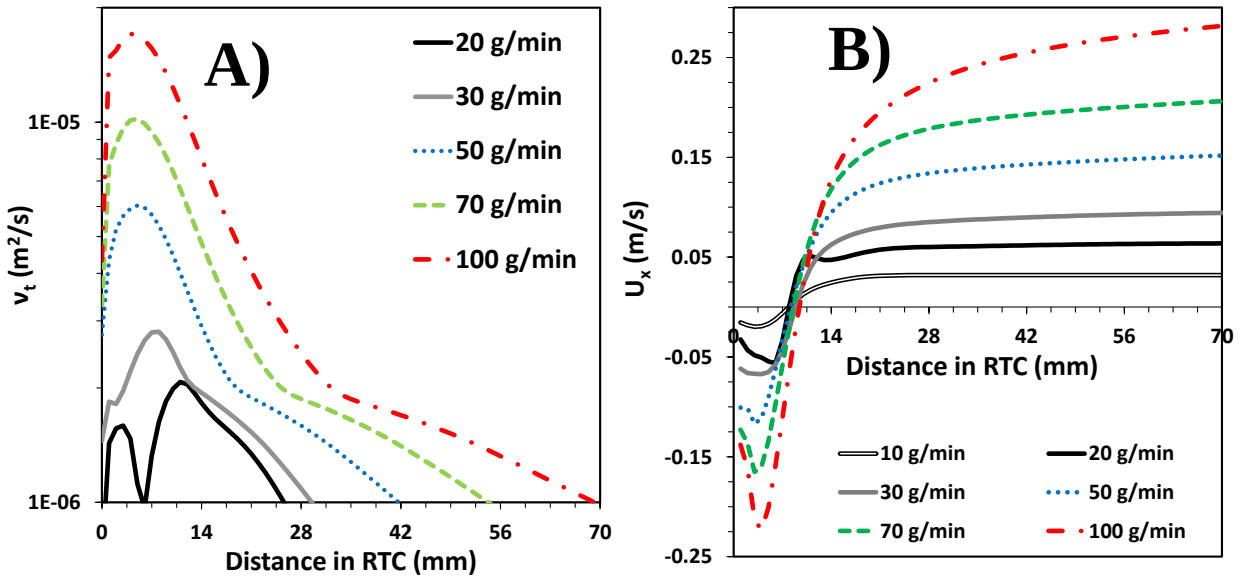

Figure 2.12. Turbulent viscosity (A) and axial velocity (B) profiles computed at the centreline of the RTC at different flow rates (g/min): 10, 20, 30, 50, 70, and 100

Table 2.3. Summary of the estimation of entrance length in the RTC via three different approaches

Q (g/min)	Entrance Length (mm)				
	Han [74]	Costaschuk [75]	Kockmann [58]	CFD: $\nu_t < \nu$	CFD: $U_x = 0.95U_{x,max}$
10	9	35	29	-	18
20	18	39	50	26	18
30	28	43	75	30	22
50	46	50	125	43	31
70	64	58	171	55	50
100	92	70	171	71	73

The approximate entrance length values listed in Table 2.3 would suggest that—downstream of the continuous-mixing region of the reactor—several of these mixing modules may be removed in order to mitigate pressure loss while maintaining a certain degree of radial mixing. For example, at 100 g/min, a near plug-flow profile can be maintained so long as the RTC is shorter

than ~ 70 mm, which would thus allow the turbulent flow structures to remain effective in promoting radial transport.

2.3.3. Effect of reactor configuration

CFD predictions of pressure drop (Figure 2.13) and RTD (Figure 2.14) reported in the validation are expanded upon in this section by means of comparing and contrasting results from four different configurations of LL reactors.

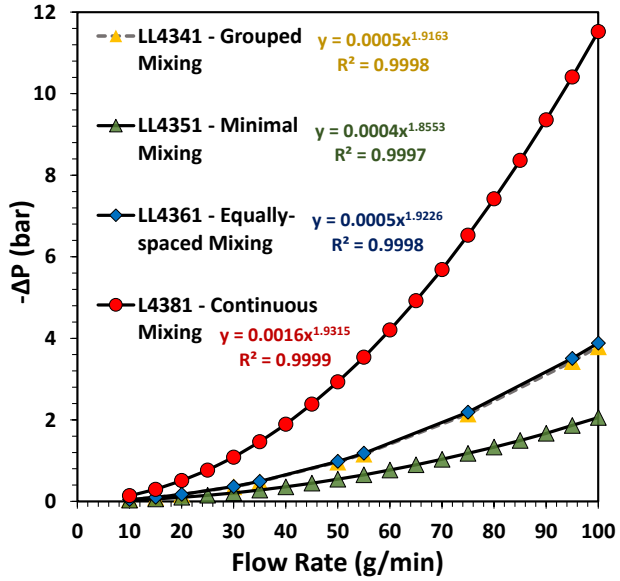

Figure 2.13. Comparison of pressure loss as a function of flow rate for different LL configurations: grouped (yellow); minimal mixing (green); equally-spaced (blue); and continuous (red)

The continuous mixing arrangement confers a pressure dependence that is most similar to a fully turbulent regime, with a power law exponent of 1.93. Pressure losses are nearly identical in the LL4341 and LL4361 given that they are comprised of the same number of obstacles and contractions. However, there is slightly more dissipation in the latter because it contains additional hydraulic regions. Lowest pressure drops are observed in the LL4351, which also fits a power law of exponent 1.85.

When LLMs are configured in a continuous series (i.e., LL4381), the RTD fits a near plug-flow profile in terms of symmetry and narrowness, which fits adequately to an AD model. This is because, as more mixing modules are added in series, the breakthrough point shifts to a greater θ value and eliminates skewness, albeit at a greater energy dissipation rate. This would not typically be expected in systems that exhibit heavy fluid bypassing, but the configuration of the LLM is

such that the streamlines leaving one LLM may be subjected to a recirculation zone in the following module due to the inversion of obstacle orientation. It is apparent when comparing the LL4381 and LL4361 RTD curves in Figure 2.14 that the use of spacing between mixing modules can effectively mitigate the rate of energy dissipation while maintaining radial transport. This observation can be attributed to the length of the RTC in the LL4361 (32 mm) relative to the estimated entrance length predicted in Table 2.3. At 30 g/min or lower, the channel length exceeds the entrance length, which leads to flow relaminarization and back-end tailing in the RTD. Even though the LL4341 and LL4361 are comprised of the same number of obstacles and contractions, the RTD of the former is much more asymmetric because its RTC (82 mm) is more than twice as long.

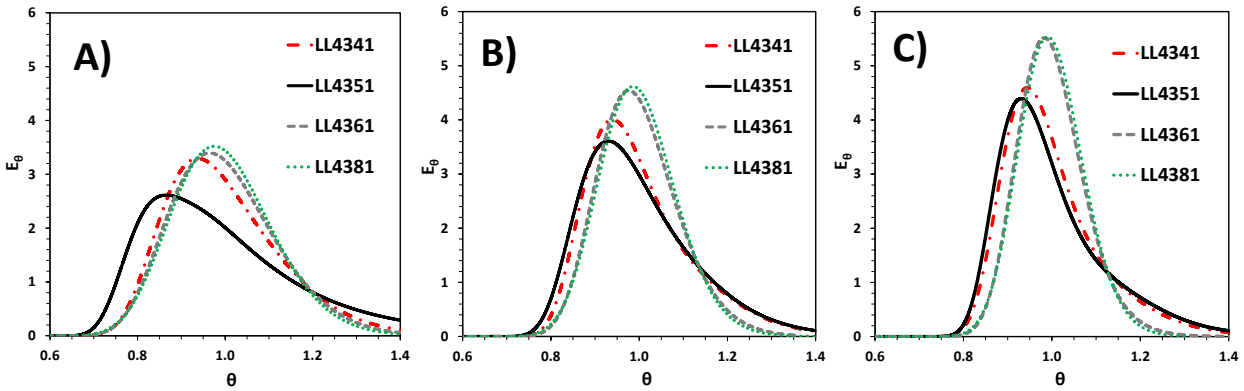

Figure 2.14. Comparison of dimensionless RTD as a function of flow rate for different LL configurations: A) 15 g/min; B) 35 g/min; and C) 95 g/min

The disparity in the plug-flow pattern between all four configurations was further analyzed by means of plotting the dimensionless variance ($\sigma^2/\bar{t}^2$) over the average specific energy dissipation rate ($\varepsilon = \frac{-\Delta P}{\rho \bar{t}}$, in W/kg), as shown in Figure 2.15. The former characterizes the narrowness of the RTD curve (i.e., approach to plug flow), whereas the latter is computed as the pressure drop over the mean residence time and density.

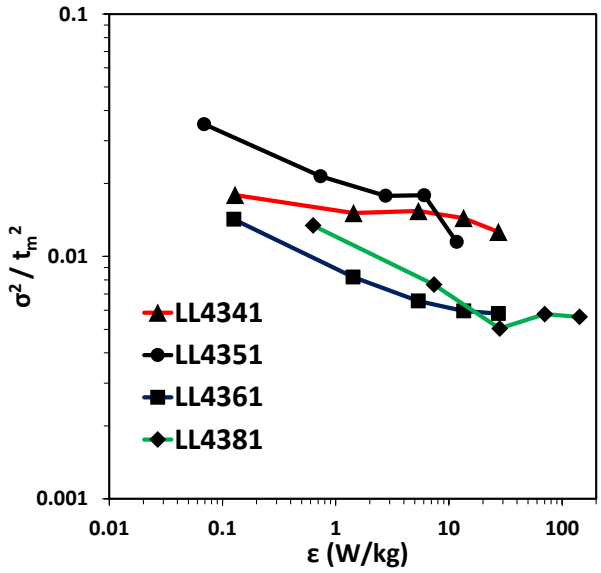

Figure 2.15. Dimensionless variance as a function of the average energy dissipation rate for different LL configurations: grouped (red); minimal mixing (black); equally-spaced (blue); and continuous (green)

Figure 2.15 confirms the comparable macromixing performance of the LL4341 to the LL4351, and of the LL4361 to the LL4381, at higher flow rates (seen previously with respect to the dimensionless RTD). At higher energy dissipation rates, which corresponds to higher flow rates, the LL4361 curve begins to concur with that of the LL4381. In addition, although the LL4351 displays a much broader RTD at low flow, it approaches the LL4341 curve more and more at high flow rate.

2.4. Conclusions

The purpose of the present study was to a) develop and validate a CFD model for predicting the fluid dynamic characteristics of single-phase flow in LL microreactors, b) locally predict streamlining, velocity, pressure, and turbulent viscosity profiles in the repeating reactor segments, and c) analyze the effect of mixing/spacing configuration on power dissipation and RTD. CFD simulations were completed in OpenFOAM at flow rates ranging from 10 to 100 g/min using a *k*-ω SSTLM turbulence model. The model predictions were in excellent agreement with experimental pressure drop ($R^2 > 0.997$) and residence time distribution (RTD) results ($R^2 > 0.97$) for four different reactor configurations.

The velocity profile of the base LL mixing module (LLM) confirmed that it effectively generates chaotic flow structures by means of its passive mixing elements. The pressure loss endured through the residence-time channel (RTC) is negligible compared to that in a single LLM. However, longer RTCs between LLMs tend to dampen the secondary flow patterns developed in the mixing region, particularly at low flow rates, which has an adverse effect on radial transport and the near-plug-flow profile in the overall reactor. Based on the effect of different mixing/spacing configurations on the RTD, channels of 35 mm or shorter (e.g., in the LL4361) appear to yield the same degree of advective transport as a continuous series of LLMs given that the RTD of the LL4381 and LL4361 are nearly identical at flow rates greater than 35 g/min. For LL plates comprised of fewer mixing modules and longer RTCs (e.g., LL4341 and LL4351), the RTD appears to broaden and exhibit back-end tailing because the longer RTCs in these configurations allow the chaotic flow patterns to attenuate before reaching the next LLM.

A near plug-flow profile (*Pe* >100) was achieved in both the LL4381 and LL4361 at all flow rates, allowing for their RTD curves to fit an AD model. In addition, the correlation between RTD narrowness (i.e., $\sigma^2/\bar{t}^2$) and average power dissipation for these two reactor configurations appear to collapse over one another. The RTD of the LL4341 and LL4351 also approach one another above 35 g/min; however, they were not narrow or symmetrical enough to fit an AD model.

2.5. Nomenclature

$-\Delta P$	pressure drop (kg/(m·s^2))
Δt	time step (s)
Δx	computational mesh cell dimension (m)
Δx_{ent}	entrance length (m)
$\nabla \bar{P}$	mean pressure gradient vector (kg/(m·s^2))
$\nabla \bar{\mathbf{U}}$	mean velocity gradient vector (s^{-1})
$\nabla_n \mathbf{U}$	velocity gradient normal to the wall (1/s)
A	cross-sectional area of reactor outlet (m^2)
C_{out}	average tracer concentration across reactor outlet (-)
Co	Courant number
C_T	tracer concentration (-)
d_h	hydraulic diameter (m)
D_T	molecular diffusion coefficient of the tracer (4.2×10^{-10} m^2/s)
E	residence time distribution (s^{-1})
E_θ	dimensionless residence time distribution (-)
$\mathbf{g}$	gravity vector (m/s^2)
k	turbulent kinetic energy (m^2/s^2)
M	parameter of the Ham & Platzer model (-) [76]
$\bar{P}$	mean pressure (Pa)
Pe	Peclet number (-)
Q	flow rate (g/min)
R^2	coefficient of determination (-)
Re	Reynolds number (-)
$Re_{\theta,t}$	local momentum thickness Reynolds number

Re_c	critical Reynolds number
Re_v	local vorticity Reynolds number
Sc_t	turbulent Schmidt number (unity)
t	time (s)
$\bar{t}$	mean residence time (s)
$\overline{\mathrm{U}}$	mean velocity (m/s)
$\overline{\mathbf{U}}$	mean velocity vector (m/s)
$\mathbf{U}'$	velocity fluctuation vector (m/s)
U_{min}	minimum velocity magnitude (m/s)
U_{max}	maximum velocity magnitude (m/s)
U_x	axial velocity (m/s)
V	reactor volume (mm^3)
$\dot{v}$	volumetric flow rate (mm^3/s)
y^+	dimensionless wall distance (-)
Δy	distance from the wall to the first cell center (m)

Abbreviations

AD	Axial dispersion (model)
AutoCAD	Computer-aided design (software)
BP	Bypassing
CFD	Computational fluid dynamics
FVM	Finite volume method
GAMG	Geometric-algebraic multi-grid (solver)
LL4341	LL w/ grouped mixing

LL4351	LL w/ minimal mixing
LL4361	LL w/ equally-spaced mixing
LL4381	LL w/ continuous mixing
LL	Liquid-liquid
LLM	LL mixing module
NETGEN 1D-2D	Mesh generation algorithm
OpenFOAM	Open-source field operation and manipulation
PBiCGStab	Stabilized preconditioned biconjugate gradient (solver)
PISO	Pressure-implicit with splitting of operators (algorithm)
R1, R2, R3, R4, R5, R6	Repeating domains of the LL plates
RTC	Residence-time channel
RTD	Residence time distribution
RTR	Residence time region
SALOME	CFD pre-processing software
SIMPLE	Semi-implicit-method-for-pressure-linked-equations (algorithm)
SST	Shear-stress transport
SSTLM	SST w/ transition improvements by Langtry and Menter [61–63]

Greek Letters

ε	average energy dissipation rate (W/kg)
γ_{int}	turbulence intermittency (-)
k	turbulent kinetic energy (m^2/s^2)
μ	fluid dynamic viscosity (kg/(m·s))
ν	molecular kinematic viscosity of the fluid (8.92×10^{-7} m^2/s)
ν_t	turbulent kinematic viscosity of the fluid (m^2/s)

$\nu_{t,min}$	minimum turbulent kinematic viscosity of the fluid (m^2/s)
$\nu_{t,max}$	maximum turbulent kinematic viscosity of the fluid (m^2/s)
ω	turbulent dissipation rate (s^{-1})
ρ	fluid density (kg/m^3)
σ^2	variance (s^2)
$\sigma^2/\bar{t}^2$	dimensionless variance
τ	space residence time (s)
θ	dimensionless time (-)
θ_{min}	dimensionless breakthrough time (-)
θ_{max}	dimensionless end time (-)

Chapter 3. Impact of micromixer geometry on residence time and mixing time distributions in the interest of competitive reaction yield

Antonio O. D'Orazio [1], Jan B. Haelssig [2*], Dominique M. Roberge [3], Arturo Macchi [1*]

[1] *Department of Chemical and Biological Engineering, University of Ottawa, Ottawa, ON, Canada*

[2] *Department of Process Engineering and Applied Science, Dalhousie University, Halifax, NS, Canada*

[3] *Chemical Manufacturing Technologies, Lonza AG, CH-3930, Visp, Switzerland*

Abstract

Computational fluid dynamics (CFD) was used to study the impact of microreactor geometry and flow rate on the local velocity fields, advective transport performance and ultimately reaction yield. Simulations of single-phase liquid flow were completed at flow rates between 10 and 100 g/min in three different types of micromixers: an LL mixer (LLM), an SZ mixer, and a tangential (TG) mixer. Based on the prediction of turbulent viscosity and fluid recirculation, it was concluded that the emergence of chaotic secondary flow patterns occurred at a characteristic Reynolds number between 500 and 1000. Contour plots of the velocity magnitude coupled with the computation of residence time distributions (RTD) showed that the SZ virtually mimics a plug-flow profile over a volume of 77 mm^3 or greater at 50 g/min. The RTD of the LLM and TG resembled that of a mixed flow pattern given that approximately 65-80% of their fluid volume is occupied by recirculation zones. As such, it required 65 LLMs in series (3105 mm^3) and 80 TGs (1142 mm^3) to approach the same pattern as 10 SZs (77 mm^3) from a macromixing perspective. Micromixing time distributions (MTD) were also characterized by locally computing the decay time of small-scale segregation (t_{SSS}) as a function of flow rate, wherein higher flow rates generated lower characteristic mixing times. The TG and LLM conferred the broadest range of mixing times, spanning nearly four orders of magnitude in the range of [0.02 ms, 10 ms], whereas the SZ generated a much narrower MTD ranging between [0.024 ms, 0.69 ms].

Keywords: Microreactors, Computational fluid dynamics (CFD), Transitional flow, Residence time distribution, Mixing time distribution, Competitive reaction

3.1. Introduction

The use of microreactor technology has become increasingly prevalent for process development and intensification in the pharmaceutical industry. Microreactors are microfluidic devices that rely on small spatial dimensions and geometrical artifacts to promote efficient mixing, particularly for fast reactions which are prone to mass-transfer limitations. Geometric features often include fixed obstacles, curvature, as well as expansions/contractions in series that passively promote intimate contact between reacting species, thereby eliminating the need for mechanical agitation [77–79]. In general, the miniaturization of chemical reactors is a favourable option for undertaking the synthesis of fine chemicals because this results in smaller diffusion lengths for heat and mass transport, as well as shorter characteristic mixing times. As such, it often translates into improved reaction control and selectivity over a more controlled residence time [4–6, 58].

Several FlowPlate® microreactors comprised of passive mixing elements, be it for single-phase, liquid-liquid or gas-liquid reactions, have been designed and benchmarked for fine chemical synthesis [1, 12, 18]. For example, liquid-liquid (LL) mixing modules were designed for undertaking fast multiphase reactions, but they are also versatile enough for fast single-phase liquid reactions in which the inherent reaction kinetics could lead to mass transfer limitations [16, 17]. This research group has recently developed a computational fluid dynamics (CFD) model and has validated RTD and power dissipation predictions for flow fields in which there is coexistence of both laminar and chaotic regions (Chapter 2). This was achieved using the Langtry-Menter four-equation transitional k-ω shear-stress-transport (SST) turbulence model [61, 63]. The application of CFD as a tool for microreactor design, optimization and scale-up allows for the mathematical prediction of local fluid dynamics and associated transport processes in various systems. As such, CFD has the potential to considerably mitigate environmental as well as economic impact tied to performing hazardous and/or costly experiments [15, 37–41].

An abundance of CFD research has also been published on the modelling of mixing at the microscopic/molecular scale in various reactors due to the importance of these phenomena in scaling of stirred-tank reactors [42], packed beds [43, 44], and micromixers [45–48]. Micromixing models aim to reproduce small-scale transport phenomena, which facilitates prediction of apparent reaction rates for both kinetically and mass-transfer limited reactions, thereby providing a better indication of how applicable a given geometry might be for undertaking a particular reaction

pathway. Quantification of mixing efficiency via computational methods is now becoming a feasible alternative to experimentally using competitive reaction schemes to deduce mixing times. For example, the research by Fox and collaborators throughout the early 2000s led to the development and validation of a direct-quadrature-method-of-moments (DQMOM) coupled with an interaction-by-exchange-with-the-mean (IEM) model for locally computing small-scale and large-scale segregation time constants [49–52]. This DQMOM-IEM model was subsequently used to simulate competitive reactions for characterizing reactive mixing [52–54]. Since then, increasingly sophisticated models for characterizing the mixing time computationally have been published, such as the hybrid approach proposed by Rizzotto *et al.* that combines a laminar rate model with a multiple time-scale model [55].

The aim of the present study was to extend and utilize the existing CFD model to conduct a computational analysis of single-phase flow and mixing in three FlowPlate® microreactor geometries: the LL mixing module (LLM), an SZ mixer, and a tangential (TG) mixer. The impact of these different geometrical elements for promoting macroscopic blending and micromixing was studied at various Reynolds numbers to deduce the impact of flow regime. Pressure drop and power dissipation were estimated for reactor geometries comprised of identical mixing modules in series and predictions were compared to experimental data. Similarly, macromixing was assessed through characterization of residence time distributions (RTD), and flow patterns were compared to ideal plug-flow and mixed-flow profiles. In addition, the micromixing performance was assessed in each mixing module by incorporating a mathematical framework into the model for locally computing the characteristic mixing times, and for generating a distribution of these mixing times. Furthermore, predicted conversion of the finite-rate reaction within a competitive-parallel reaction scheme involving an infinitely fast reaction was used to assess the effect of reactor geometry and flow conditions on reaction yield. This comparative study provides detailed information about flow patterns, RTDs, local blending, local micromixing time distributions (MTD), and conversion of competitive-parallel reactions in three micromixer geometries, including a discussion of advantages and limitations. This information will help to guide future scaling and geometric optimization studies. All CFD simulations were completed using OpenFOAM (open-source field operation and manipulation) [56].

3.2. Methodology

3.2.1. Microreactor geometries and computational mesh

The LLM, SZ and TG mixing modules were selected for analysis because they are key components of a toolbox of FlowPlate® microreactors. Each geometry was modelled in AutoCAD and discretized in 2D using the SALOME pre-processing platform [80]. The dimensions, mesh and mesh quality characteristics are summarized in Table 3.1. The hydraulic diameter at the smallest cross-section in all three modules is 0.71 mm (0.5 × 1.25 mm). In this study, the hydrodynamics and mixing performance of each module was assessed via simulation through a continuous series of mixers, thereby eliminating the effects of entrance and exit regions as well as the residence-time channels that would typically be present on the full reactor plate. This domain of the reactor is termed the mixing region (MR) and is typically placed at the inlet to promote early mixing, as shown in Figure B-3.1 of Appendix B.

The 3D mesh of each mixing domain was generated in OpenFOAM by extruding the 2D mesh on a symmetry plane in the depth direction (depth of 1.25 mm with 20 cell layers), where an expansion factor of 1.05 was used from bottom to center plane. The bulk of the LLM 2D grid is composed of triangular cells, resulting in triangular prisms when extruded, whereas most of the 2D SZ and TG meshes are composed of quadrangle cells, which results in hexahedral-dominant meshes when extruded. Viscous layers of quadrangle cells were used along the walls of each geometry. The impact of mesh resolution for each geometry was tested by analyzing flow and tracer simulation results as a function of cell size. The mesh resolution for each geometry was ultimately chosen as the coarsest mesh in which pressure drop and the first moment of age distribution became independent of further refinement within a tolerance of 2%. Mesh quality metrics are summarized in Table 3.1.

Table 3.1. Micromixer dimensions (in mm), 2D mesh and 3D mesh quality metrics. Direction of flow is from left to right. Geometries are not drawn to scale

	LLM	SZ	TG
Dimensions	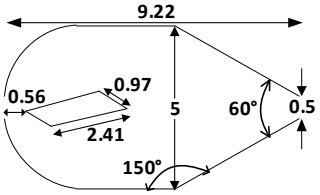	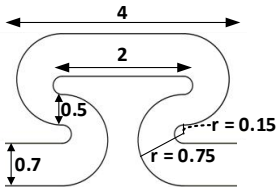	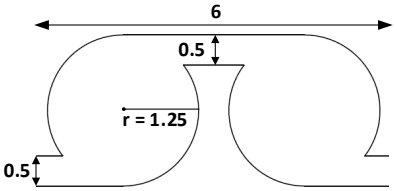
Mesh	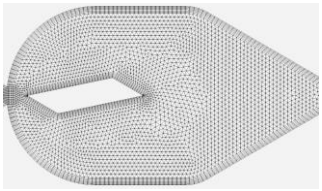	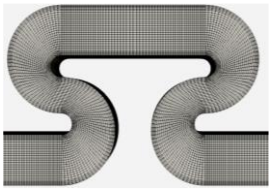	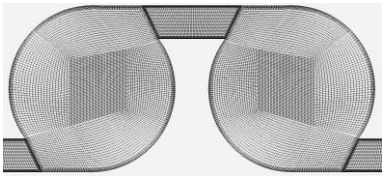
# 2D Faces	7 282	8 064	18 296
# 3D Cells	145 640	161 280	365 920
Max. Aspect Ratio	7.6	5.1	11.6
Ave. Non-orthogonality	5.7	8.5	14.8
Max. Skewness	1.97	0.31	3.0
Volume	41.3 mm^3	7.7 mm^3	14.3 mm^3

3.2.2. Governing equations

In this study, local fluid dynamics, pressure drop and RTDs were analyzed to characterize macromixing in the mixer geometries. Additionally, micromixing performance was assessed by computing mixing times and simulating a set of competitive-parallel reactions. The description of the equations used are divided into sections to explain the approaches used to predict (1) the flow field, (2) RTDs, (3) mixing times, and (4) conversion in the competitive reaction scheme.

3.2.2.1. Flow field and turbulence modelling

The continuity equation (Equation (3.1)) and the conservation of linear momentum equation are both employed for simulating flow of an incompressible Newtonian fluid. Given that the microreactors being investigated typically operate in a regime of chaotic advection at Reynolds

numbers of 500 or greater, momentum is subjected to small-scale spatial and temporal variations that make the flow fields challenging to resolve computationally [60, 81]. Thus, to eliminate the need for very fine computational meshes and small time steps, these equations were Reynolds-averaged and solved with respect to the mean velocity and pressure fields. Reynolds-averaging results in a nonlinear term known as the Reynolds stress that must be closed before the momentum equations can be solved. Conventionally, the Boussinesq hypothesis is used to define the Reynolds stress in terms of the strain tensor and a turbulent viscosity [81], which results in the following form of the Reynolds-averaged Navier-Stokes equations:

$$\nabla \cdot \bar{\mathbf{U}} = 0 \tag{3.1}$$

$$\frac{\partial \bar{\mathbf{U}}}{\partial t} + \bar{\mathbf{U}} \cdot \nabla \bar{\mathbf{U}} = -\frac{1}{\rho}\nabla \bar{P} + \mathbf{g} + \nabla \cdot (\nu + \nu_t)[\nabla \bar{\mathbf{U}} + (\nabla \bar{\mathbf{U}})^T] \tag{3.2}$$

where ρ denotes the density of the fluid (kg/m^3), $\nabla \bar{P}$ is the mean pressure gradient (Pa), $\nabla \bar{\mathbf{U}}$ and $(\nabla \bar{\mathbf{U}})^T$ are the mean velocity gradient and its transpose (s^{-1}), $\mathbf{g}$ is the gravity vector (m/s^2), $\nu = \mu/\rho$ is the molecular kinematic viscosity of the fluid (m^2/s), ν_t is the turbulent kinematic viscosity of the fluid (m^2/s), μ is the molecular dynamic viscosity of the fluid (Pa·s), $\bar{\mathbf{U}}$ is the mean velocity vector (m/s), and t is time (s).

A variety of turbulence models are available to predict the turbulent kinematic viscosity [62, 82–84], but selection of a model is challenging because previous studies on the LLM have shown that the flow regime varies from laminar to turbulent for typically encountered flow rates. The *k*-ω SSTLM model, derived by Langtry and Menter based on the classical *k*-ω model [61–63], was employed in the present study based on its previous application for the simulation of macromixing in LL microreactors. In Chapter 2, it was concluded that the SSTLM model was well-suited for providing a global solution for the transitional and chaotic flow regimes through the LLM. The model is comprised of two components: a generic infrastructure provided by two transport equations as well as experimental correlations based on transition regime data. The two transport equations are for the intermittency (γ_{int}) and the momentum thickness Reynolds number ($Re_{\theta,t}$). The former triggers the transition process by controlling the production of turbulent kinetic energy (k, in m^2/s^2), while the latter represents a transition onset criterion. More information

pertaining to the development of the *k-ω* SSTLM turbulence model is described in literature [61–63].

3.2.2.2. Residence time distribution

The RTD was predicted numerically by simulating the transport of a passive tracer using the advection-diffusion equation:

$$\frac{\partial C_T}{\partial t} + \nabla \cdot (\overline{\mathbf{U}}\, C_T) = \nabla \cdot (D_T\, \nabla C_T) + \nabla \cdot \left(\frac{\nu_t}{Sc_t}\, \nabla C_T\right) \tag{3.3}$$

where C_T represents the dimensionless tracer concentration; D_T is the molecular diffusion coefficient of the tracer, which was assumed to be 4.2×10^{-10} m^2/s in this study based on the typical value for an experimental system [17]; and Sc_t is the turbulent Schmidt number, which was assumed to be unity in this study. More information related to the manipulation and analysis of RTD data may be found in Appendix A.

3.2.2.3. Mixing times

A numerical approach for simulating micromixing and competitive-parallel reactions developed by Fox and collaborators [49, 51, 85] was implemented in OpenFOAM to predict characteristic mixing times and conversion for a given reaction rate constant in the competitive-parallel reactions. Mixing times can be determined by first solving Equations (3.1) and (3.2) along with the SSTLM model for the steady-state flow field and turbulence parameters. The distribution of micromixing time scales can then be calculated locally as a function of the mixture fraction (a_1) and its variance (a_2), which can be computed via the following equations:

$$\frac{\partial a_1}{\partial t} + \nabla \cdot (\overline{\mathbf{U}}\, a_1) = \nabla \cdot (D_T\, \nabla a_1) + \nabla \cdot \left(\frac{\nu_t}{Sc_t}\, \nabla a_1\right) \tag{3.4}$$

$$\frac{\partial a_2}{\partial t} + \nabla \cdot (\overline{\mathbf{U}}\, a_2) = \nabla \cdot (D_T\, \nabla a_2) + \nabla \cdot \left(\frac{\nu_t}{Sc_t}\, \nabla a_2\right) + 2\frac{\nu_t}{Sc_t}|\nabla a_1|^2 - 2\gamma a_2 \tag{3.5}$$

In Equation (3.5), $2\gamma a_2$ is a dissipation term due to micromixing, and the turbulent viscosity (ν_t) is computed from the SSTLM model.

As described by Liu and Fox [51], two types of segregation that characterize mixing can be defined based on a_1 and a_2: large-scale segregation (LSS), and small-scale segregation (SSS). The former represents deviations of the mixture fraction from the mean as follows:

$$a_3 = (a_1 - \bar{a})^2 \tag{3.6}$$

where $\bar{a}$ is the global mean mixture fraction, which is equal to 0.5 when two streams with equal flow rates are mixed. Based on Equations (3.4) and (3.6), the characteristic time of LSS variance decay (t_{LSS}) can be defined as follows:

$$t_{LSS} = \frac{a_3}{2\left(\frac{\nu_t}{Sc_t}\right)|\nabla a_1|^2} \tag{3.7}$$

In theory, once complete mixing is achieved at a certain point in the system from a macromixing perspective, t_{LSS} approaches zero and leads to the production of SSS. This leads to the definition of the decay time of SSS (t_{SSS}) as follows:

$$t_{SSS} = \frac{1}{2\gamma} \tag{3.8}$$

The micromixing time parameter (γ, in s^{-1}) is modelled as a function of the turbulent kinetic energy (k, in m^2/s^2), and either ε (turbulent kinetic energy dissipation rate, in m^2/s^3) or ω (specific turbulent kinetic energy dissipation rate, in s^{-1}):

$$\gamma = \frac{C_\phi}{2}\frac{\varepsilon}{k} = 0.5 C_\phi C_\mu \omega \tag{3.9}$$

where C_ϕ is an empirical mixing coefficient that describes the mechanical-to-scalar-time-scale ratio [50], and $C_\mu \approx 0.09$. For high-Reynolds-number flow $C_\phi \approx 2$, but for liquids it is necessary to evaluate C_ϕ based on the local turbulent Reynolds number (Re_t). Liu and Fox [51] provide the following expression:

$$\begin{aligned} C_\phi = {} & 0.4093 + 0.6015(\log_{10} Re_t) + 0.5851(\log_{10} Re_t)^2 + 0.09472(\log_{10} Re_t)^3 \\ & -0.3903(\log_{10} Re_t)^4 + 0.1461(\log_{10} Re_t)^5 - 0.01604(\log_{10} Re_t)^6 \end{aligned} \tag{3.10}$$

where

$$Re_t = \frac{k}{(\varepsilon\nu)^{0.5}} \tag{3.11}$$

The distribution of t_{SSS} scales throughout a given mixing module was subsequently used to compute a mean characteristic mixing time ($\overline{t_{mix}}$).

3.2.2.4. Competitive-parallel reactions

Competitive reaction schemes are often used as a chemical method for determining the characteristic mixing time of a system. In the present study, competitive-parallel reactions were simulated in each geometry to further assess their micromixing performance based on the predicted conversion of the slower reaction. The reaction scheme adopted in this study consists of an infinitely fast reaction (I) coupled with a second finite-rate reaction (II):

$$\mathrm{A} + \mathrm{B} \xrightarrow{k_1 \approx \infty} \mathrm{P}_1 \tag{I}$$

$$\mathrm{A} + \mathrm{D} \xrightarrow{k_2} \mathrm{A} + \mathrm{P}_2 \tag{II}$$

where both reactions are described by elementary (i.e., second-order) rate laws. The adopted scheme is representative of the commonly used fourth Bourne reaction, where the slower reaction is catalytic with respect to component A. However, in this study, the rate constant of reaction (II), k_2, was varied based on the mean characteristic mixing time for each geometry to assess micromixing numerically.

The mixing-limited reactions were modelled using the two-environment DQMOM model coupled with an IEM model [51]. The former solves composition probability density function (PDF) transport equations whereas the latter serves to close the conditional molecular diffusion term. In this study, the two-environment DQMOM-IEM model of Liu and Fox [51] was implemented in OpenFOAM and used to simulate the reactive mixing process. In this model, one conservation equation is required to track the mixing of the two environments:

$$\frac{\partial \alpha_1}{\partial t} + \nabla \cdot (\overline{\mathbf{U}}\, \alpha_1) = \nabla \cdot (D_T\, \nabla \alpha_1) + \nabla \cdot \left(\frac{\nu_t}{Sc_t}\, \nabla \alpha_1 \right) \tag{3.12}$$

where α_1 is the volume fraction of the first environment, and $\alpha_2 = 1 - \alpha_1$ is the volume fraction of the second environment.

Two additional conservation equations are required for the mixture fraction in the two environments:

$$\frac{\partial \alpha_1 X_1}{\partial t} + \nabla \cdot (\overline{\mathbf{U}}\, \alpha_1 X_1) = \nabla \cdot \left(D_T\, \nabla (\alpha_1 X_1) \right) + \nabla \cdot \left(\frac{\nu_t}{Sc_t}\, \nabla (\alpha_1 X_1) \right) + \gamma \alpha_1 \alpha_2 (X_2 - X_1) \tag{3.13}$$

$$\frac{\partial \alpha_2 X_2}{\partial t} + \nabla \cdot (\bar{\mathbf{U}}\, \alpha_2 X_2) = \nabla \cdot \left(D_T\, \nabla(\alpha_2 X_2)\right) + \nabla \cdot \left(\frac{\nu_t}{Sc_t}\, \nabla(\alpha_2 X_2)\right) + \gamma \alpha_1 \alpha_2 (X_1 - X_2) \quad (3.14)$$

where X_1 and X_2 are the mixture fractions in environments 1 and 2, respectively. The last term in these equations is responsible for micromixing.

Additional conservation equations are required to track the reaction-progress variable of reaction (II) in each of the two environments:

$$\frac{\partial \alpha_1 Y_{21}}{\partial t} + \nabla \cdot (\bar{\mathbf{U}}\, \alpha_1 Y_{21}) = \nabla \cdot \left(D_T\, \nabla(\alpha_1 Y_{21})\right) + \nabla \cdot \left(\frac{\nu_t}{Sc_t}\, \nabla(\alpha_1 Y_{21})\right)$$
$$+\gamma \alpha_1 \alpha_2 (Y_{22} - Y_{21}) + \alpha_1 S_{2\infty}(X_1, Y_{21}) \quad (3.15)$$

$$\frac{\partial \alpha_2 Y_{22}}{\partial t} + \nabla \cdot (\bar{\mathbf{U}}\, \alpha_2 Y_{22}) = \nabla \cdot \left(D_T\, \nabla(\alpha_2 Y_{22})\right) + \nabla \cdot \left(\frac{\nu_t}{Sc_t}\, \nabla(\alpha_2 Y_{22})\right)$$
$$+\gamma \alpha_1 \alpha_2 (Y_{22} - Y_{21}) + \alpha_2 S_{2\infty}(X_2, Y_{22}) \quad (3.16)$$

where Y_{21} and Y_{22} are the are the reaction-progress variables for reaction (II) in environments 1 and 2, respectively. The reaction source terms in the first ($S_{2\infty}(X_1, Y_{21})$) and second ($S_{2\infty}(X_2, Y_{22})$) environment are given by the following equation:

$$S_{2\infty}(a_k, Y_{2k}) = c_{A0} k_2 \left(1 - \frac{X_k}{X_{sk}}\right)\left(\frac{X_k}{X_{sk}} - Y_{2k}\right) \quad \text{if } 0 \le X_k \le X_{sk} \text{ and } 0 \le Y_{2k} \le X_k / X_{sk} \quad (3.17)$$

where $k = 1$ or 2 represents the mixing environment.

Since reaction (I) is considered instantaneous, its progress variable in the two environments can be calculated explicitly from the following expression:

$$Y_{1k} = \min\left(\frac{X_k}{X_{sk}}, \frac{1 - X_k}{1 - X_{sk}}\right) \quad (3.18)$$

where

$$X_{s1} = \frac{c_{A0}}{c_{A0} + c_{B0}} \quad (3.19)$$

$$X_{s2} = \frac{c_{A0}}{c_{A0} + c_{D0}} \quad (3.20)$$

and c_{A0}, c_{B0} and c_{D0} are the inlet concentrations (mol/L) of components A, B and D.

After obtaining the solution of the mixture fraction and reaction progress variables, the reactant concentrations in each environment (c_{Ak}, c_{Bk} and c_{Dk}) can be determined using the following equations:

$$c_{Ak} = c_{A0}(1 - X_k - Y_{1k}[1 - X_{s1}]) \tag{3.21}$$

$$c_{Bk} = c_{B0}(X_k - X_{s1}Y_{1k}) \tag{3.22}$$

$$c_{Dk} = c_{D0}(X_k - X_{s2}Y_{2k}) \tag{3.23}$$

The average concentrations of the reactants ($\overline{c_A}$, $\overline{c_B}$ and $\overline{c_D}$) can then be determined from the local concentrations and the volume fractions of the two environments using the following expressions:

$$\overline{c_A} = \alpha_1 c_{A1} + \alpha_2 c_{A2} \tag{3.24}$$

$$\overline{c_B} = \alpha_1 c_{B1} + \alpha_2 c_{B2} \tag{3.25}$$

$$\overline{c_D} = \alpha_1 c_{D1} + \alpha_2 c_{D2} \tag{3.26}$$

The conversion of reactant D in the finite-rate reaction (X_D) can be used as a measure of the mixing quality:

$$X_D = 1 - \frac{\overline{\overline{c_D}}}{\overline{a} c_{D0}} \tag{3.27}$$

where $\overline{\overline{c_D}}$ is the mass-weighted outlet concentration of D, and the global mean mixture fraction $\overline{a}$ is 0.5 for mixing of streams with equal flow rates.

3.2.3. Simulation sequence

All simulations were completed using OpenFOAM, which is an open-source platform for CFD simulations and the solution of partial differential equations [56]. All simulations used the kinematic viscosity and density of water at 25°C (8.92×10^{-7} m^2/s and 997 kg/m^3). The molecular diffusion coefficient was 4.2×10^{-10} m^2/s in all simulations based on the typical value for an experimental system, but this value had minimal impact in simulations with higher levels of turbulence.

3.2.3.1. Steady-state flow field

The simpleFoam solver in OpenFOAM is designed to simulate incompressible steady-state flow by employing the semi-implicit-method-for-pressure-linked-equations (SIMPLE) algorithm to iteratively solve for the pressure and velocity fields. In the SIMPLE algorithm, the momentum equation (Equation (3.2)) is discretized to obtain an equation for velocity and combined with the continuity equation (Equation (3.1)) to obtain an explicit equation for pressure. The resulting equations are solved iteratively in a segregated manner to converge on the pressure and velocity fields [57, 65, 66]. The simpleFoam solver was used in conjunction with the SSTLM turbulence model to compute the steady-state pressure, velocity, turbulent kinetic energy, specific turbulent kinetic energy dissipation rate and turbulent kinematic viscosity fields.

3.2.3.2. Residence time distribution

The RTD can be predicted by solving Equation (3.4) to simulate the transport of a passive tracer. In this study, a custom OpenFOAM solver named scalarTurbTransportFoam was created to solve Equation (3.3) and directly access the steady-state velocity and turbulent kinematic viscosity fields from the converged simpleFoam flow simulation. The RTD was determined by monitoring the mass-weighted concentration at the outlet after injection of a tracer pulse at the inlet for 1.4 ms. The second-order-accurate Crank-Nicolson scheme was used for time integration, and the time step was chosen to be small enough so that the RTD was independent of time step size for each flow rate and geometry. More information related to the manipulation and analysis of RTD data may be found in Appendix A.

3.2.3.3. Mixing times

To predict mixing times, the simpleFoam solver was again used to determine the converged steady-state velocity and turbulent kinematic viscosity fields. A custom OpenFOAM solver named scalarMicroMixingFoam was created to solve Equations (3.4) and (3.5) for the mixture fraction of a passive scalar and its variance along with the auxiliary relationships in Equations (3.6)–(3.11) to determine the characteristic time of small- and large-scale segregation (t_{SSS} and t_{LSS}). In the simulations, a fluid containing a passive tracer (a_1= 1) was introduced at one inlet of a T-junction leading to a series of mixers, while an equal flow of the same fluid without tracer (a_1= 0) was introduced at the other inlet.

3.2.3.4. Competitive-parallel reactions

Competitive-parallel reaction simulations were performed using a two-step procedure. First, the quasi-steady-state velocity, environment volume fraction, and turbulence variable fields were initialized by solving Equations (3.1), (3.2) and (3.12) along with the SSTLM model. In OpenFOAM, this was achieved by using the built-in twoLiquidMixingFoam solver. Second, the reactant concentration fields and conversion of D were computed using the quasi-steady-state velocity, turbulence, and environment volume fraction fields by solving Equations (3.13)–(3.27) combined with the auxiliary relationships in Equations (3.9)–(3.11). This was accomplished by implementing a custom solver named twoLiquidIEMFoam, which was developed by extending the twoLiquidMixingFoam solver. Although the twoLiquidIEMFoam can also simultaneously solve Equations (3.1), (3.2) and (3.12) along with the SSTLM model, initialization using twoLiquidMixingFoam improved stability and reduced computation time.

In the simulations, fluid streams containing A ($\alpha_1 = 1$, $X_1 = X_2 = Y_{21} = Y_{22} = 0$) and B + D ($\alpha_1 = X_1 = Y_{21} = Y_{22} = 0$, $X_2 = 1$) were introduced at opposite ends of a T-junction leading to a series of mixing modules at equal flow rates. The only parameters that need to be defined to simulate reactive mixing in addition to those required for flow simulations involving a passive tracer are the inlet concentrations of the reactants, c_{A0}, c_{B0} and c_{D0}, as well as the finite reaction rate constant, k_2. The inlet reactant concentrations were kept constant in all simulations with an equimolar feed ratio of A:D and B fed in 5% excess.

3.2.4. Numerical solvers, schemes and boundary conditions

The numerical solvers employed to solve the discretized transport equations are summarized in Table C-3.1 of Appendix C. Steady-state pressure and velocity fields were solved using the geometric-algebraic multi-grid (GAMG) and the stabilized preconditioned biconjugate gradient (PBiCGStab) solvers, respectively. The latter solver was also used to determine the concentration field for RTD computations as well as the mixture fraction and reaction progress fields for reactive mixing computations. Turbulence model transport quantities ($k, \nu_t, \omega, \gamma_{int}, Re_{\theta,t}$) as well as the volume fraction of environment 1 (Equation (3.12)) were calculated via smoothSolver with a Gauss-Seidel smoother. For steady-state simulations, an under-relaxation factor of 0.3 was used for pressure and 0.7 was used for all other variables to limit

oscillations between iterations. The scaled residuals for pressure, velocity and turbulence variables were converged to at least 10^{-4}, and changes in the pressure and velocity fields were monitored to ensure convergence to steady-state profiles. The scaled residuals for concentration, mixture fraction and reaction progress were converged to at least 10^{-9}.

High-order numerical discretization schemes are necessary to minimize artificial diffusion, but they can introduce instability when used in the advection term [66]. Therefore, discretization schemes should be chosen carefully to ensure accuracy and a stable solution, and upwind-weighted schemes are usually used to ensure numerical stability for the advection term. In this study, second-order-accurate schemes were employed for the discretization of all spatial derivatives to minimize artificial diffusion. Similarly, the second-order-accurate Crank-Nicolson scheme was used for time integration when solving Equation (3.3) to determine RTDs. However, a first-order-accurate implicit Euler method was used in reactive mixing simulations because only the steady-state results were desired in this case. The numerical schemes used in this study are summarized in Table C-3.2 of Appendix C.

The boundary conditions used in all CFD simulations are summarized in Table 3.2. Low-Reynolds-number wall functions were employed for k, ω and ν_t to modify the shear stress at the walls in case the viscous layers at the boundary were not fully resolved for direct integration. The low-Reynolds-number modifications were incorporated in the model to add effects of molecular viscosity to the diffusion terms and to account for anisotropy in the dissipation rate term [59, 62]. In these wall functions, the values of k and ω are switched between estimations for their values in the viscous and inertial sublayer based on whether the dimensionless wall distance (y^+) at the first cell center at the wall is less or greater than 11.

Table 3.2. Boundary conditions used in CFD simulations completed in OpenFOAM

Purpose	Variable	Boundary Patch	Specification
Steady-state flow	Velocity	Inlet	fixed flat profile
		Walls	no slip
		Outlet	zero gradient
	k	Inlet	fixed value
		Walls	kLowReWallFunction
		Outlet	zero gradient
	ω	Inlet	fixed value
		Walls	omegaWallFunction
		Outlet	zero gradient
	ν_t	Inlet	calculated
		Walls	nutLowReWallFunction
		Outlet	calculated
	γ_{int}	Inlet	fixed value
		Walls	zero gradient
		Outlet	zero gradient
	$Re_{\theta,t}$	Inlet	fixed value
		Walls	zero gradient
		Outlet	zero gradient
	Pressure	Inlet	zero gradient
		Walls	zero gradient
		Outlet	fixed value
RTD computation	Concentration	Inlet	fixed value (time-dependent pulse)
		Walls	zero gradient
		Outlet	zero gradient
Characterization of $\boldsymbol{t_{SSS}}$ and $\boldsymbol{t_{LSS}}$	a_1	Inlet 1	fixed value = 1
		Inlet 2	fixed value = 0
	a_2	Both inlets	fixed value = 0
Competitive reaction	α_1	Inlet 1	fixed value = 1
		Inlet 2	fixed value = 0
	X_1	Both inlets	fixed value = 0
	X_2	Inlet 1	fixed value = 0
		Inlet 2	fixed value = 1
	Y_{2k}	Both inlets	fixed value = 0

3.3. Results and Discussion

3.3.1. Local characterization of fluid dynamics

This section details the impact of flow rate on the local fluid dynamic characteristics of the LL, SZ and TG microreactor geometries. The *k-ω* SSTLM model was used in this study for predicting both laminar and chaotic flow based on previous application for the simulation of macromixing in LL microreactors presented in Chapter 2. CFD simulations were completed through domains comprised of several mixing modules in series at flow rates ranging from 10 to 100 g/min. The flow fields in both the LLM and TG become fully established, with less than 2% deviation between modules at any given point, after roughly two modules in series. The SZ requires roughly three modules in series before reaching an established flow profile, which is comparable to the LLM on a volumetric basis.

Figure 3.1 displays the fully-developed contour plots of the 2D velocity magnitude within the LLM, SZ and TG mixers at center-plane depth (z = 0.625 mm) as a function of flow rate. The velocity scale is consistent between geometries at a given flow rate and the characteristic Reynolds numbers are calculated at the constriction of each geometry (0.5 × 1.25 mm). The velocity magnitude throughout the LLM is generally much lower than that of the other modules because of its larger expansion (5 × 1.25 mm at largest cross-section) and volume (41.32 mm^3) relative to the SZ (7.74 mm^3) and TG (14.27 mm^3). In the LLM, the fluid is split into two streams by an obstacle, each maintaining roughly half of its kinetic energy before re-converging upon one another at the orifice of the next module. The SZ velocity profile at 10 g/min appears to be completely dictated by viscous forces given that it is nearly parabolic along its entire length, except for small pockets of stagnant fluid underneath the main streamline. In general, this geometry exhibits the least dead volume (roughly 10% of the total volume) because the width of its channel only expands to 0.7 mm. However, small fluid recirculation zones form below the main channel in the straight region as well as near the concave wall of each SZ bend, particularly at *Re* greater than 640. As flow rate is increased, the SZ flow begins to transition to a more plug-flow-like pattern due to the emergence of Dean vortices in the curved zones of the mixer (as shown in Figure B-3.2 of Appendix B), thereby improving the quality of radial transport perpendicular to the primary direction of flow.

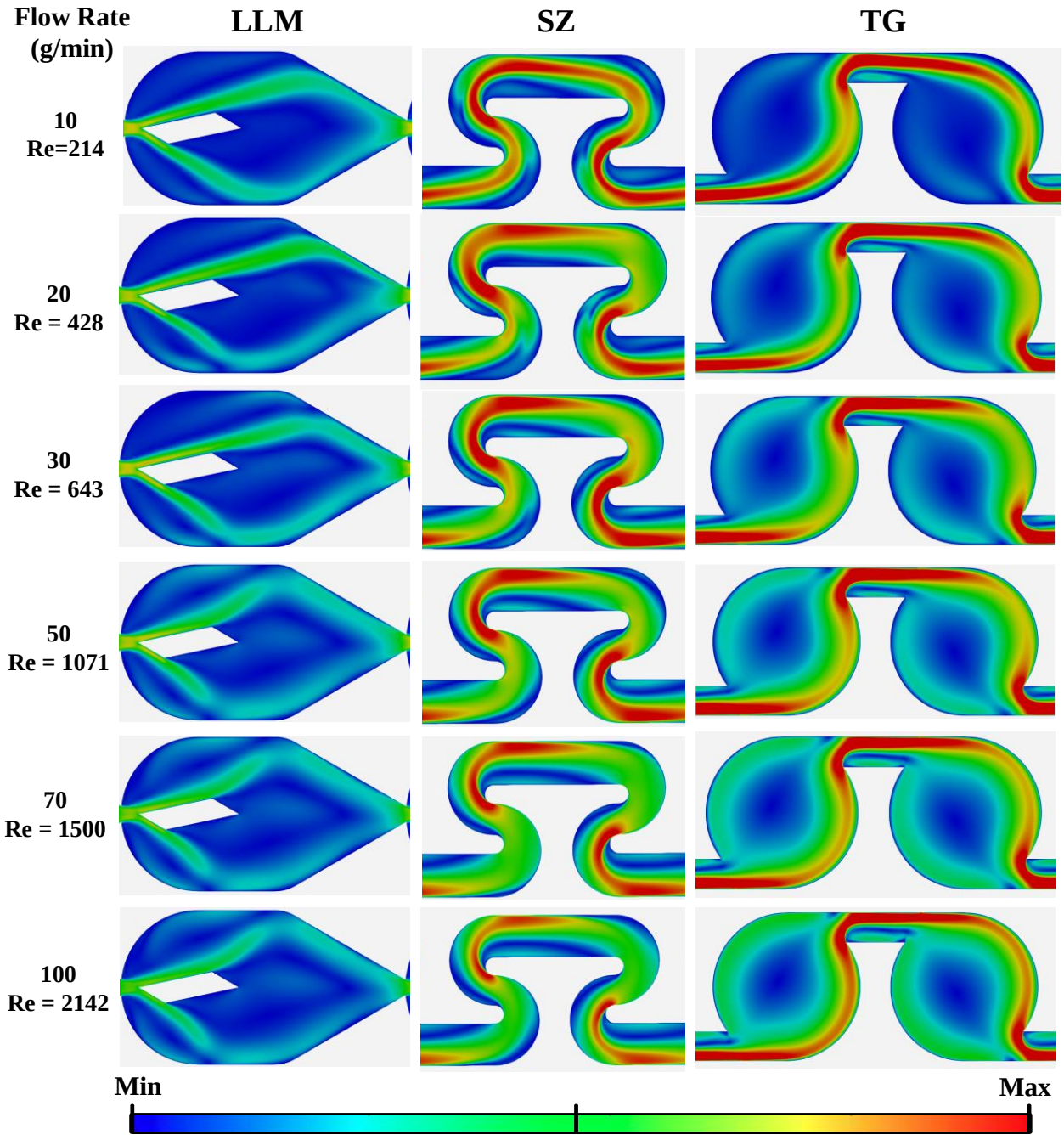

Figure 3.1. Velocity magnitude profiles in the LLM, SZ and TG at symmetry plane (z = 0.625 mm). U_{min}= 0 (blue) for each flow rate, whereas U_{max} (red) varies as follows (m/s): 0.45 (10 g/min), 0.91 (20 g/min), 1.28 (30 g/min), 2.21 m/s (50 g/min), 3.39 (70 g/min) and 5.37 (100 g/min)

The TG module aims to promote strong fluid recirculation via two circular regions connected through a short channel. As flow rate is increased in any of the geometries, the relative kinetic energy within the bypass zones begins to dissipate towards other parts of the module, as the dead volume (dark blue) appears to recede considerably from 10 to 50 g/min. This is most

pronounced in the TG, where the dead zone at the center of the recirculation region continues to shrink as flow is increased to 100 g/min, but it is also noticeable in the LLM where the fluid begins to gain more momentum behind the obstacle in the opposite direction of flow. The aforementioned transition occurring in the velocity field as a function of flow rate is generally most evident between 20 and 50 g/min, which would indicate that the onset of chaotic secondary flows is somewhere between a characteristic Reynolds number of 500 and 1000. In the TG, it is likely that this critical Reynolds number is on the low end of that range as the volume of fluid bypassing relative to recirculation remains consistently around 70–80% from 20 to 100 g/min.

Figure 3.2 shows 2D streamlines superimposed over the velocity magnitude profiles presented in Figure 3.1 for better perception of advective recirculation. In the LLM, four distinct recirculation vortices begin to emerge at 30 g/min (Re = 643): two in between the bypass streams, and another two adjacent to the obstacle walls. Some stagnant fluid is found in the eye of these zones, but the amplitude of recirculation grows stronger with flow rate and begins to distort the bypass streams. The TG flow field resembles the LLM in that there is coexistence of bypassing streamlines with strong recirculation patterns, which occupy 65–75% of the volume in the TG and 70–80% of the volume in the LLM. The TG velocity magnitude profiles and streamlines confirm that its recirculating fluid gains more kinetic energy relative to the bypassing fluid as flow rate increases. Conversely, the primary stream of flow in the SZ gains more volume as flow rate is increased.

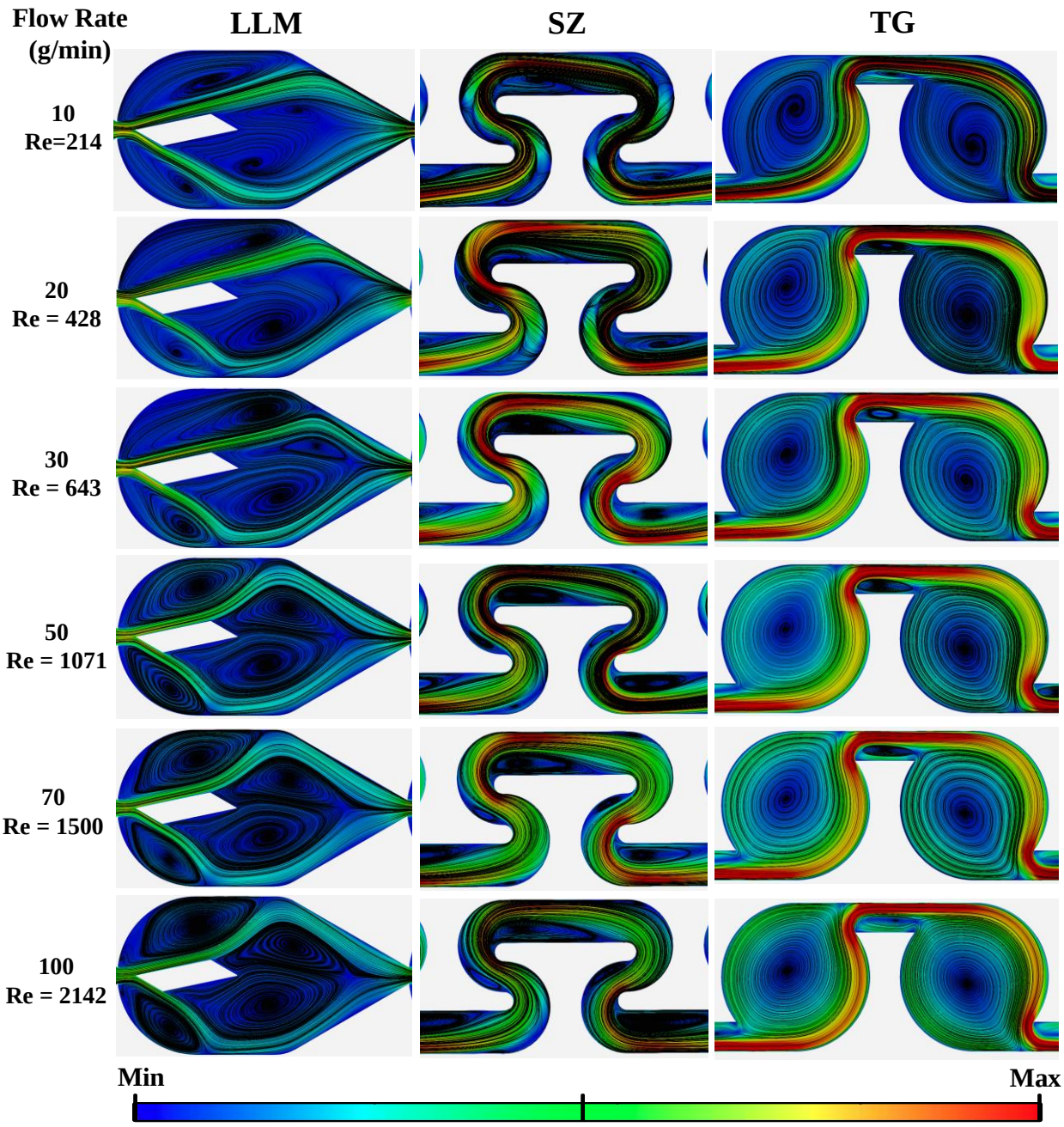

Figure 3.2. Streamline maps in the LLM, SZ and TG at symmetry plane (z = 0.625 mm). U_{min} = 0 (blue) for each flow rate, whereas U_{max} (red) varies as follows (m/s): 0.45 (10 g/min), 0.91 (20 g/min), 1.28 (30 g/min), 2.21 m/s (50 g/min), 3.39 (70 g/min) and 5.37 (100 g/min)

The turbulent kinematic viscosity (ν_t) field, which provides a measure of the relative mass transport rate due to time-averaged fluctuations, is presented in Figure 3.3 for each geometry as a function of flow rate. At 10 g/min, the flow regime is purely laminar in each geometry given that the turbulent viscosity is effectively 0 (i.e., no turbulent diffusion). Even though ν_t begins to

increase considerably in the SZ and TG at 20 g/min, the maximum value of ν_t in all geometries is still less than the molecular kinematic viscosity of the fluid (8.92×10^{-7} m^2/s). However, mass transport due to turbulent diffusion would already be considerable given the low value of the molecular diffusion coefficient in liquids (assumed to be 4.2×10^{-10} m^2/s in this study). Beyond 30 g/min, the turbulent viscosity in the SZ is virtually uniform throughout its volume, indicating a clear emergence of radial momentum transport. This emergence is also evident in the TG at that same flow rate, but with a broader distribution of ν_t, as there appears to be considerably more advective transport at the boundary of the recirculation zone and bypass line. In general, the TG appears to generate the most chaotic advection, which can be attributed to the relative size of its recirculation zones rotating in opposite directions. In the LLM, the turbulent viscosity map shows that most of the energy dissipation appears to originate from the boundary of the bypass streams (as shown at 30 g/min), before eventually transitioning to a more uniform distribution at 70 g/min or greater.

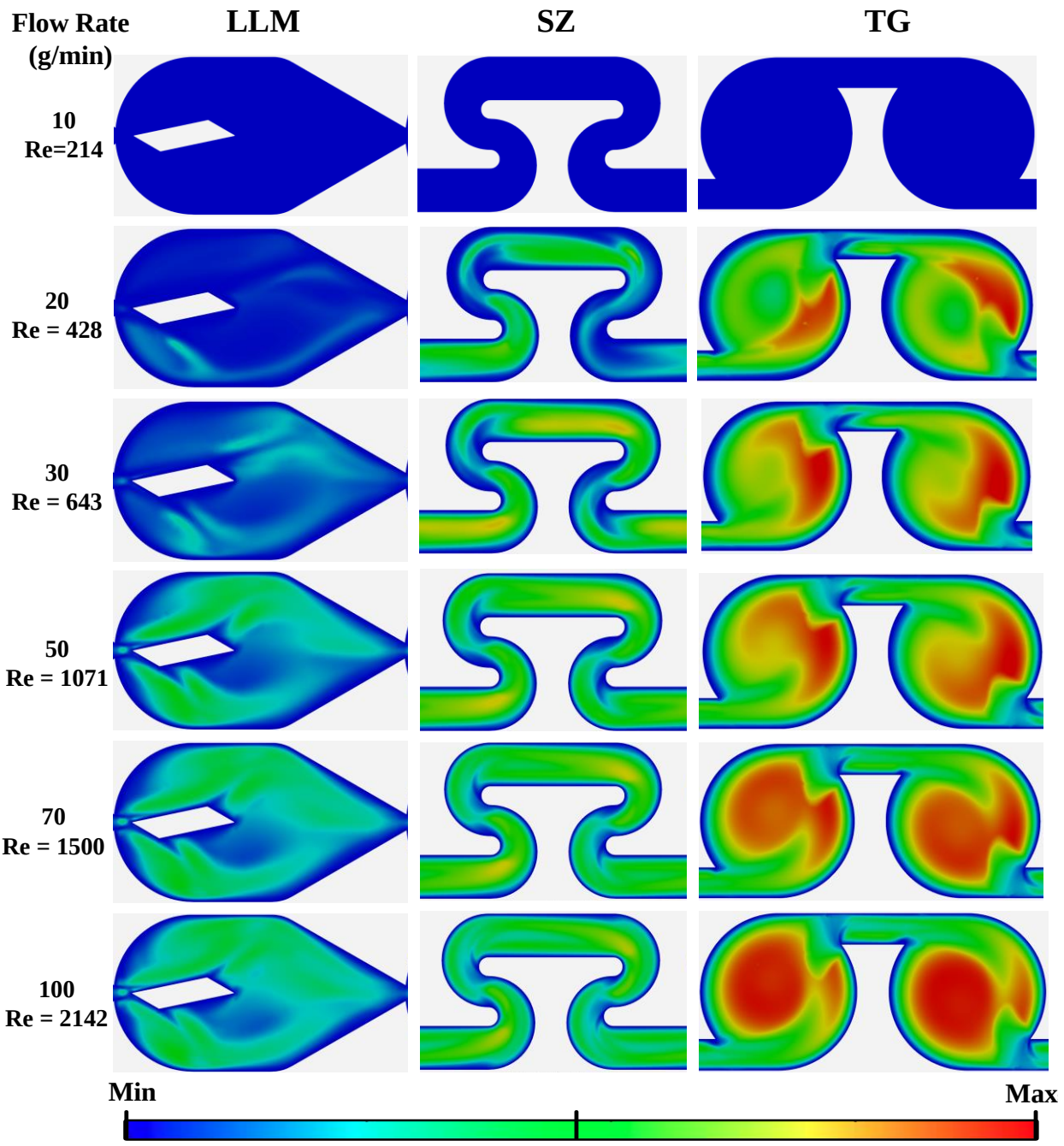

Figure 3.3. Turbulent viscosity fields in the LLM, SZ and TG at symmetry plane (z = 0.625 mm). $\boldsymbol{\nu_{t_{min}}}$ = 0 (blue) for each flow rate, whereas $\boldsymbol{\nu_{t_{max}}}$ (red) varies as follows (m^2/s): 0 (10 g/min), 6.7×10^{-6} (20 g/min), 2.2×10^{-5} (30 g/min), 4.1×10^{-5} (50 g/min), 5.0×10^{-5} (70 g/min) and 6.2×10^{-5} (100 g/min))

3.3.2. Pressure drop and RTD computations (macromixing)

This section details the comparative analysis of the LLM, SZ and TG mixing modules from a macromixing perspective by analyzing the pressure loss, RTD and rate of energy dissipation. The validation of the CFD model predictions of pressure loss in comparison to experimental data was completed extensively in previous simulation studies (Chapter 2) and is shown in Figure B-3.3 of Appendix B. The steady-state pressure drop ($-\Delta P$, in kPa) per module as a function of flow rate is presented in Figure 3.4 with each curve fitted to a power law ($R^2 > 0.994$).

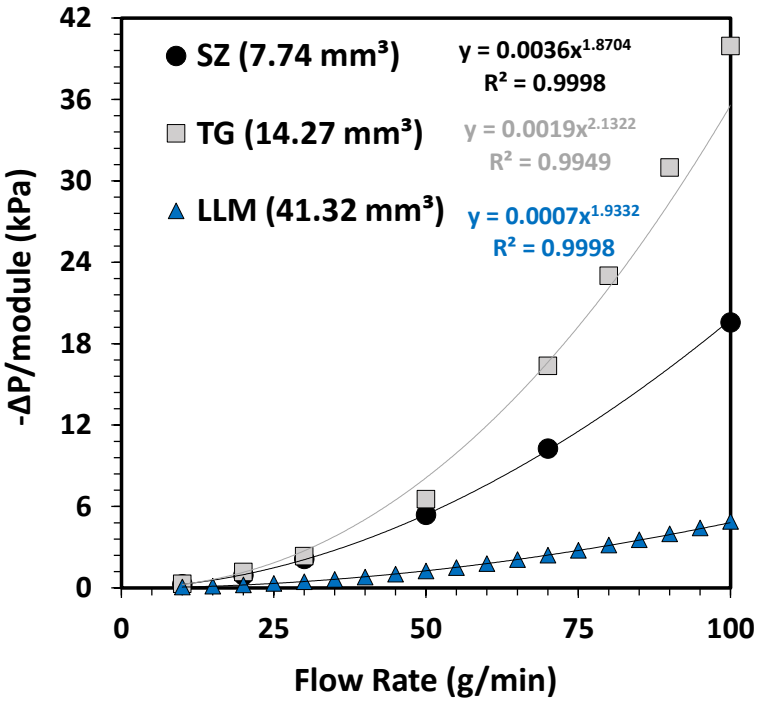

Figure 3.4. Pressure drop predictions through the LLM, SZ and TG mixers as a function of flow rate

The LLM dissipates the least energy since it is much less geometrically constricted compared to other mixers. Despite the separation and recombining of flow around the obstacle, roughly 65% of the liquid in the LLM at any given moment is found in the expanded region of the module, where the width is an order of magnitude greater (5 mm) than at the contraction. The pressure loss per module in the SZ is much greater because the cross-section only expands from a hydraulic diameter of 0.71 mm (0.5 × 1.25 mm) to 0.9 mm (0.7 × 1.25 mm). The impact of volume is another important component to consider when evaluating pressure loss and blending at a macroscopic level, especially when considering the impact of macromixing on fast reactions. The impact of volume is not displayed in Figure 3.4 but becomes evident when characterizing the

macromixing as a function of power dissipation (see Figure 3.7). It should be noted that a TG module is comprised of two identical (yet opposite in terms of the angular direction of flow that they confer) recirculation units that have roughly the same volume as an SZ. The pressure loss incurred in a TG is always greater than that incurred in an SZ, but the difference between the two grows much larger above 30 g/min. This concurs with the observations drawn from Figure 3.3, which showed that the volume of "hot spots" for turbulent viscosity in the TG increased much more with flow rate relative to that in the SZ, exceeding it virtually by an order of magnitude at 100 g/min. The pressure loss trend for the SZ can also be explained by the streamlines presented in Figure 3.2, which show that the degree of streamline curvature at increasing flow rates is less pronounced in the SZ because most of the fluid is found in a single stream of flow. This suggests that the dissipation of energy in the SZ is dominated by viscous exchange between parallel fluid streamlines rather than by recirculation, as shown in other variations of serpentine micromixers [86, 87]. Conversely, recirculation dissipation appears to be the more dominant phenomenon contributing to pressure loss incurred in the LLM and TG.

The pressure dependence of the SZ and LLM were fit to a power law exponent of 1.87 and 1.93, respectively, which would be comparable to that of a turbulent regime (where $-\Delta P \propto Q^2$). The apparent power law exponent for the TG pressure loss relationship is greater than 2, which even exceeds that of a fully isotropic turbulent regime. Nevertheless, this is not uncommon for geometries that promote intense back-mixing because it implies that the dissipation of energy due to chaotic advection in the recirculation region is greater than that due to viscous exchange in the bypass stream and wall shear stress [88]. The amount of recirculating fluid that is subjected to a delayed exit, compared to the amount of fluid bypassing the well-mixed pockets within the domain, demonstrates the importance of RTD analysis.

The macroscopic blending occurring within a given geometry was characterized by means of the RTD (E, in s^{-1}) as a function of flow rate and total volume. The RTDs were computed via time-dependent simulations of passive scalar transport in a domain comprised of consecutive modules in series, modelled as the mixing region (MR) of a FlowPlate® microreactor (Figure B-3.1 of Appendix B). The distributions were normalized with respect to the mean residence time ($\bar{t}$ in s, the first moment of RTD) in order to be made dimensionless ($E_\theta = E \times \bar{t}$) and plotted as a function of the dimensionless residence time ($\theta = t/\bar{t}$). The RTD of each geometry was then

formally assessed by comparing its spread (second moment) and symmetry (third moment) to the following axial dispersion (AD) model:

$$E_\theta(\theta) = \frac{1}{2}\sqrt{\frac{Pe}{\pi\theta}}\,exp\left\{-\frac{Pe(1-\theta)^2}{(4\theta)}\right\} \tag{3.28}$$

where the dimensionless Peclet number (Pe) is the lone model parameter used to characterize the variance of the RTD (σ^2 in s^2). This model assumes a perfectly symmetrical RTD, and a Pe >100 is indicative of a virtually plug-flow pattern [89]. From a scientific perspective, Pe represents the ratio of advective transport over diffusive transport.

The ratio of the computed mean residence time ($\bar{t}$) over the space time ($\tau = V/\dot{v}$, in s) was used to gain insight on the amount dead volume in each module, where V is the total volume of the mixer (in mm^3) and $\dot{v}$ is the volumetric flow rate (in mm^3/s). As summarized in Table 3.3, it was found that $\bar{t}/\tau$ was slightly lower than unity regardless of flow rate and geometry, which indicates that the fluid leaves the mixer slightly earlier than expected because of stagnant volume. This concurs with the velocity profiles presented in Figure 3.1 which showed that there was some stagnant fluid in each mixer. This is evident especially at 10 g/min for the LLM and TG, where $\bar{t}/\tau$ was found to be 0.972 and 0.944, respectively. As flow rate is increased, the velocity profiles showed that the stagnant fluid volume receded because there was greater fluid exchange between the bypass and recirculation zones. As a result, $\bar{t}/\tau$ increases above 0.98 in the LLM and TG at flow rates of 50 g/min or greater. In the SZ, $\bar{t}/\tau$ is also slightly lower than unity at 10 g/min (0.986 to be exact) since there is some dead volume below the main flow stream. However, at higher flow rates in the SZ, $\bar{t}/\tau$ is virtually equal to 1 (i.e., greater than 0.99) as this dead volume shrinks considerably from 10 to 30 g/min.

The RTD comparison between different mixer geometries was first carried out using the mixing region (MR) of each reactor (13 LLM vs. 18 SZ vs. 12 TG), as shown in Figure B-3.4 of Appendix B, to gain macromixing perspective on currently-benchmarked reactors. These simulation results showed that a domain of 18 SZ (139 mm^3) was enough to virtually mimic a plug-flow profile at flow rates of 20 g/min or greater, showing a slight right-skew due to fluid channeling. Conversely, the LLM and TG confer a much broader and heavily skewed RTD, with the former geometry yielding a slightly lower variance over the same number of mixers. However,

since the reaction conversion depends directly on the mean fluid residence time in addition to macromixing, the much larger volume of the LLM compared to the TG and SZ meant that the analysis needed to be revised to compute the RTD over domains of equivalent volume, as shown in Figure 3.5. The comparison was thus made over a volume of 620 mm^3, which is equivalent to 13 LLM, 80 SZ and 44 TG. For this volume, the SZ gives the closest RTD to an ideal plug-flow reactor, which is a result of the uniformity of the velocity fields shown in Figure 3.1 and Figure 3.2. The TG confers the next best distribution from a macromixing perspective given that it is much more symmetric compared to the LLM, particularly at higher flow rates. However, neither the LLM nor TG can mimic a plug-flow pattern over this volume as their RTDs are much broader compared to the AD model at Pe = 100. Based on a single module, the RTD of the LLM and TG geometries resembles more of a mixed-flow pattern as explained by the large recirculation volume shown in Figure 3.2. However, it was expected that their RTD would start to narrow and become more symmetric around $\bar{t}$ ($\theta = 1$) as more modules were added to the domain, as theoretically described by the tanks-in-series model relating the number of ideal mixed tanks (N) to the Peclet number [89]:

$$Pe = 2N - 1 \tag{3.29}$$

This relationship thereby raises the question of how closely the TG and LLM approach an ideal mixed tank. In other words, how many modules in series are required for these geometries to approach a plug-flow profile?

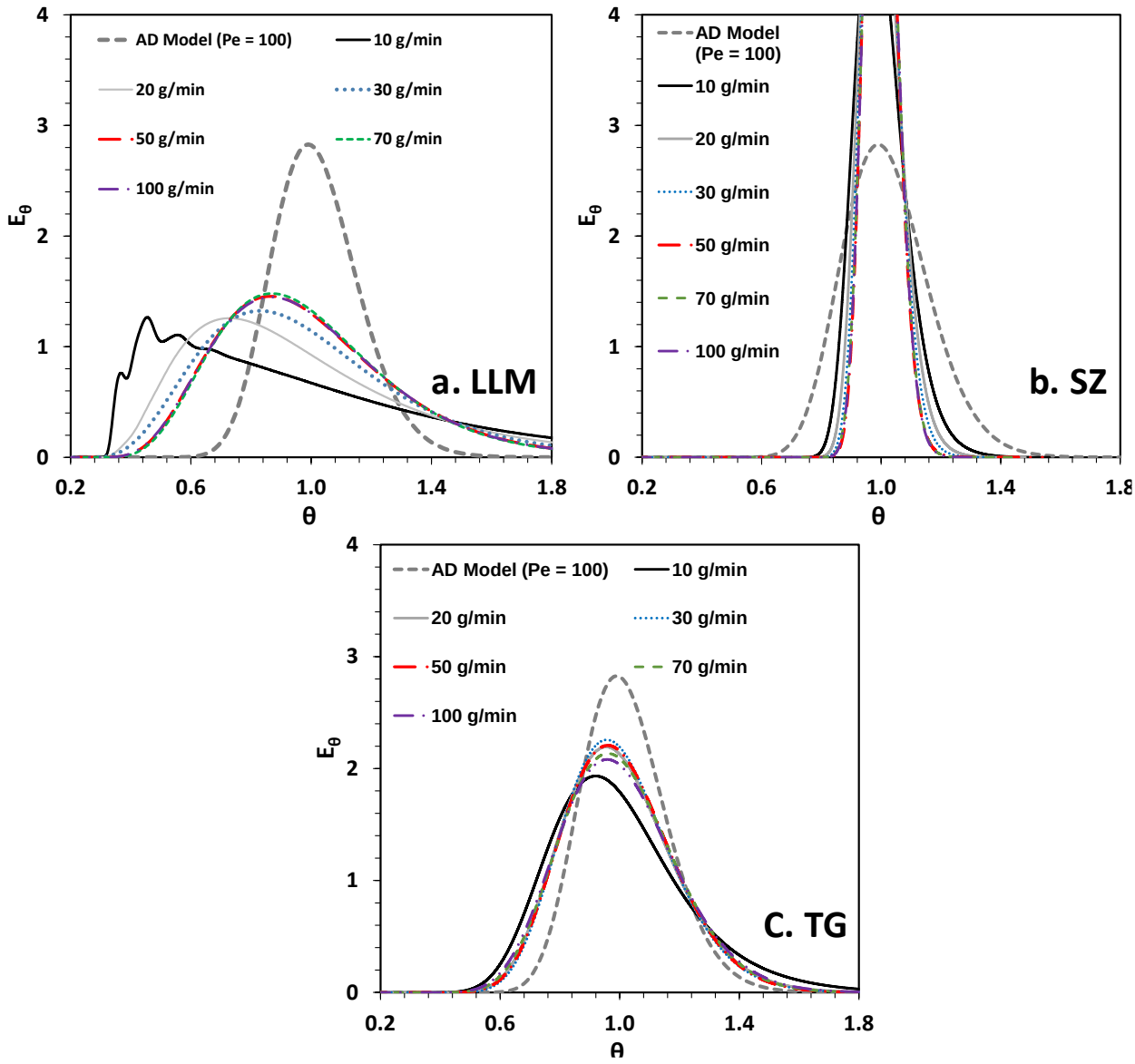

Figure 3.5. CFD predictions of the dimensionless RTD (E_θ) in the LLM (a), SZ (b) and TG (c) at several flow rates ranging from 10 to 100 g/min. The comparison of all three modules was undertaken over an equivalent volume of 620 mm^3. An axial dispersion (AD) model curve mimicking a near-plug-flow profile (*Pe* = 100) is shown for better perception of macromixing performance

The impact of reactor volume on the RTD was analyzed to estimate the minimum number of consecutive mixing modules required for a given microreactor to achieve $Pe \geq 100$. Several studies completed with Lonza's custom-design microreactors, be it experimental [16, 17, 56] or computational (Chapter 2), have revealed the importance of optimizing the configuration of mixing modules juxtaposed with residence-time channels. However, this analysis focused solely on the design of the reactor's mixing region comprised of mixers in series. Figure 3.6 presents the RTD

of each geometry as a function of the number of mixers at flow rates of 10 and 50 g/min. In general, an increase in flow rate from 10 to 50 g/min tends to improve the symmetry and reduce the variance of the RTD. Higher flows are not shown because the RTD proved to be nearly independent of flow rate above 50 g/min for all geometries. As more LLM and TG are added in series, the RTD eventually collapses over the AD model. At 10 g/min, a near-plug-flow profile is achieved after 208 LLM in series (9936 mm^3) and 112 TG in series (1598 mm^3). At 50 g/min, the required number of mixers needed to reach $Pe \geq 100$ is reduced to about 65 LLM (3105 mm^3) and 80 TG (1140 mm^3). At 10 g/min the TG reaches a plug-flow pattern after roughly 1598 mm^3, which is about an order of magnitude less volume compared to the LLM. As flow rate is increased, the difference in required volume to achieve equivalent macromixing performance between the TG and LLM begins to reduce, but the TG is still three times more volume efficient at 50 g/min. At any given flow rate, the flow pattern of the SZ approaches $Pe \geq 100$ over a much shorter residence time compared to the LLM and TG. The impact of reactor volume and flow rate on the RTD is summarized in Table 3.3, where V_{Pe100} is the volume of consecutive mixers needed to reach a *Pe* of 100.

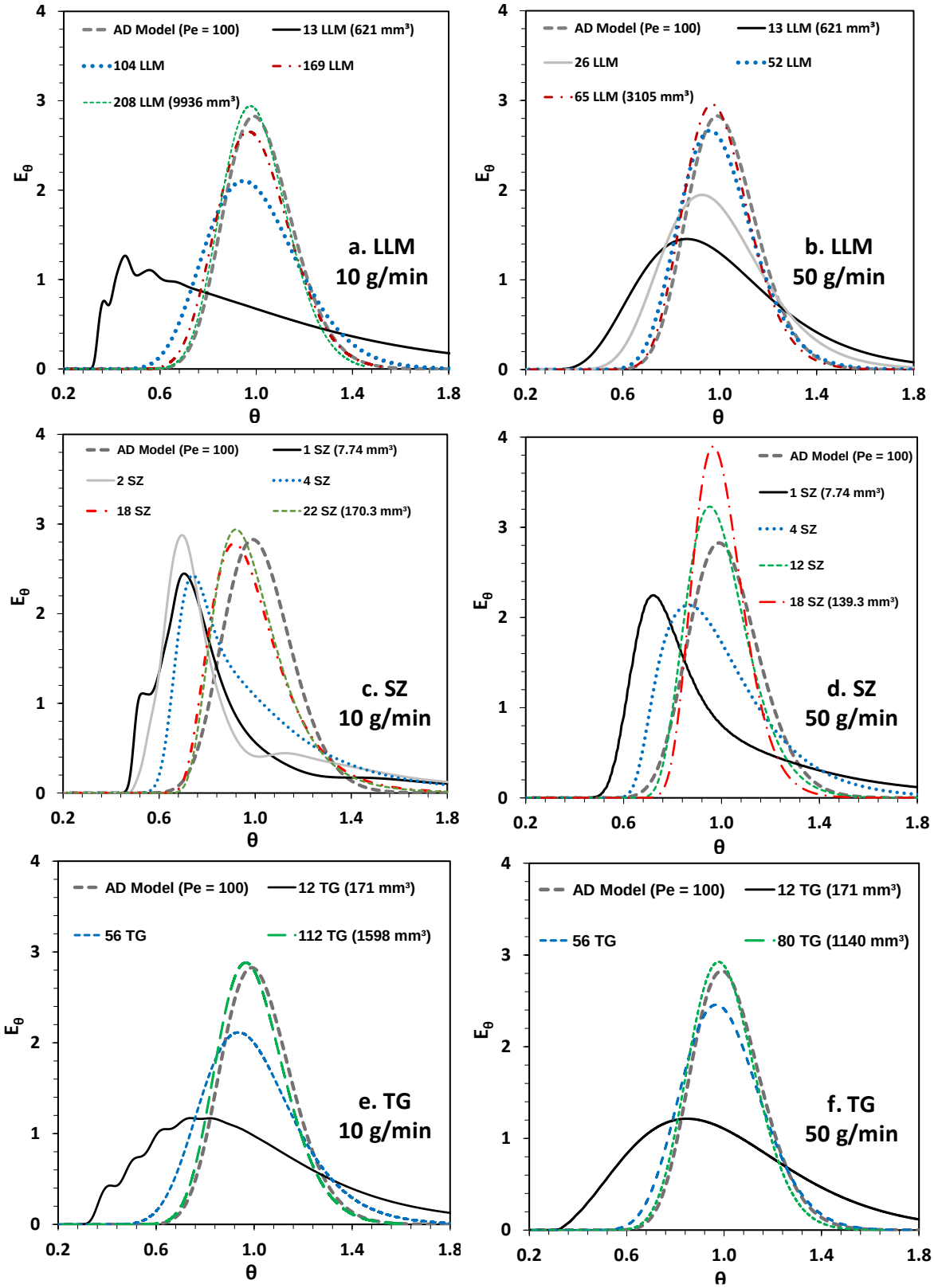

Figure 3.6. The impact of volume on the dimensionless RTD (E_θ) of the LLM (a-b), SZ (c-d) and TG (e-f) at flow rates of 10 and 50 g/min. Each curve represents a different number of modules configured in series and is compared to a near-plug-flow AD model (*Pe* = 100)

Table 3.3. Summary of the residence time, reactor volume and the number of repeating modules in series required to achieve a near-plug-flow profile (*Pe* >100) at 10, 50 and 100 g/min

Flow Rate (g/min)	LLM	SZ	TG
10	$V_{Pe100} \approx 9936$ mm^3 (208 modules) $\bar{t}_{208\ \text{LLMs}} = 59.4$ s $\bar{t}/\tau_{\ 1\ \text{LLM}} = 0.972$	$V_{Pe100} \approx 170.3$ mm^3 (22 modules) $\bar{t}_{22\ \text{SZs}} = 1.04$ s $\bar{t}/\tau_{\ 1\ \text{SZ}} = 0.986$	$V_{Pe100} \approx 1598$ mm^3 (112 modules) $\bar{t}_{112\ \text{TGs}} = 9.56$ s $\bar{t}/\tau_{\ 1\ \text{TG}} = 0.944$
50	$V_{Pe100} \approx 3105$ mm^3 (65 modules) $\bar{t}_{65\ \text{LLMs}} = 3.72$ s $\bar{t}/\tau_{\ 1\ \text{LLM}} = 0.982$	$V_{Pe100} \approx 77.4$ mm^3 (10 modules) $\bar{t}_{10\text{SZs}} = 0.096$ s $\bar{t}/\tau_{\ 1\ \text{SZ}} = 0.996$	$V_{Pe100} \approx 1142$ mm^3 (80 modules) $\bar{t}_{80\ \text{TGs}} = 1.37$ s $\bar{t}/\tau_{\ 1\ \text{TG}} = 0.980$
100	$V_{Pe100} \approx 3105$ mm^3 (65 modules) $\bar{t}_{65\ \text{LLMs}} = 1.86$ s $\bar{t}/\tau_{\ 1\ \text{LLM}} = 0.988$	$V_{Pe100} \approx 92.9$ mm^3 (12 modules) $\bar{t}_{12\ \text{SZs}} = 0.057$ s $\bar{t}/\tau_{\ 1\ \text{SZ}} = 0.994$	$V_{Pe100} \approx 1170$ mm^3 (82 modules) $\bar{t}_{82\ \text{TGs}} = 0.70$ s $\bar{t}/\tau_{\ 1\ \text{TG}} = 0.987$

As an alternative to the Peclet number, the dimensionless variance (σ^2/t_m^2) is another parameter that is used to characterize the spread of the RTD (i.e., its second moment). The impact of the specific average power dissipation ($\varepsilon = \frac{-\Delta P}{\rho \bar{t}}$, in W/kg) on this parameter was plotted in Figure 3.7 for each geometry as an added measure of macromixing comparison over an equivalent volume of 120 $\pm$ 5 mm^3. Again, an equivalent volume was used in this comparison because reaction conversion is controlled by the mean fluid residence time in addition to macromixing. As proven in the characterization of RTD, the SZ confers the narrowest spread of residence time over an equivalent power dissipation, achieving a virtually plug-flow profile over a much smaller volume compared to the TG and LLM. Regardless of geometry, the second moment of the RTD appears uninfluenced by any increase in power dissipation past 100 W/kg (i.e., at flow rates greater than 30 g/min in the SZ and TG, or greater than 70 g/min in the LLM). However, in the range of 0.1 to 100 W/kg, the dimensionless variance appears to decrease linearly with increasing power dissipation, which can be attributed to the increase in radial transport via secondary flow patterns as the flow becomes dominated by chaotic advection. Overall, this analysis appears to confirm that it is ideal to operate at flow rates of at least 30 g/min in these module (perhaps 50 g/min in the LLM), while greater than 70 g/min will dissipate more power with marginal gain towards the quality of macromixing.

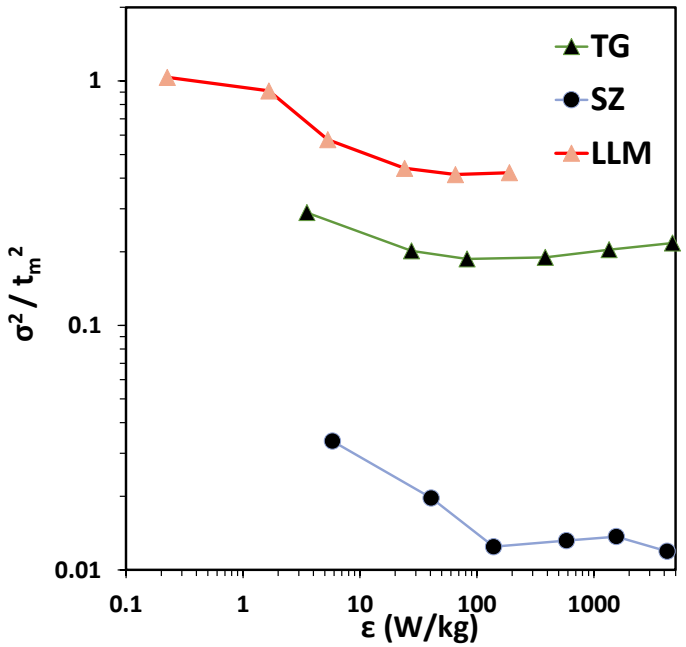

Figure 3.7. Dimensionless variance of the RTD as a function of the average power dissipation for the LLM, SZ and TG computed over an equivalent volume of 120±5 mm^3

3.3.3. Characterization of micromixing efficiency

The mathematical modelling of mixing at the molecular scale of motion is necessary in tandem with the RTD for characterizing non-ideal flow systems and, ultimately, for predicting reactor performance. The distribution of mixing time scales is especially important for fast reaction applications [34, 90]. This section provides an analysis of the computed local mixing time distribution (MTD) of the three microreactor geometries. The local mixing time constants for the decay of large-scale segregation (t_{LSS}) and small-scale segregation (t_{SSS}) are considered. As described in section 3.2.2.3, these parameters are computed by means of the mixture fraction of a passive scalar (a_1) and the mixture fraction variance (a_2), which are determined based on the velocity and turbulence model parameters.

Micromixing simulations were performed by introducing two streams with equal flow rates through a T-junction, where the scalar was introduced into one of two inlets (i.e., unmixed feed conditions). The mixing of the scalar through a quasi-steady-state flow domain of consecutive mixers was then quantified. The system is blending-limited (i.e., limited by t_{LSS}) in the early part of the mixing domain where $a_2 \gg 0$. As a_2 approaches zero and a_1 approaches 0.5, t_{LSS} becomes smaller than t_{SSS}, and the system is then considered to be micromixing-limited. Thus, the first step in characterizing the micromixing efficiency was to estimate the volume needed to achieve

complete blending ($a_2 < 0.02$) from a macroscopic perspective. This was estimated based on the contour plots of the mixture fraction at low and high flow rate, as shown in Figure 3.8. At 10 g/min, the SZ and TG appeared to blend the quickest (~15 mm^3) compared to the LLM (~160 mm^3), whereas at 100 g/min, the system was virtually completely blended as it exited the T-junction, although some additional blending appears to occur in the LLM. Similar macroscopic blending results at 50 g/min are shown in Figure 3.12 to provide better perspective with respect to the impact of LSS on reaction yield.

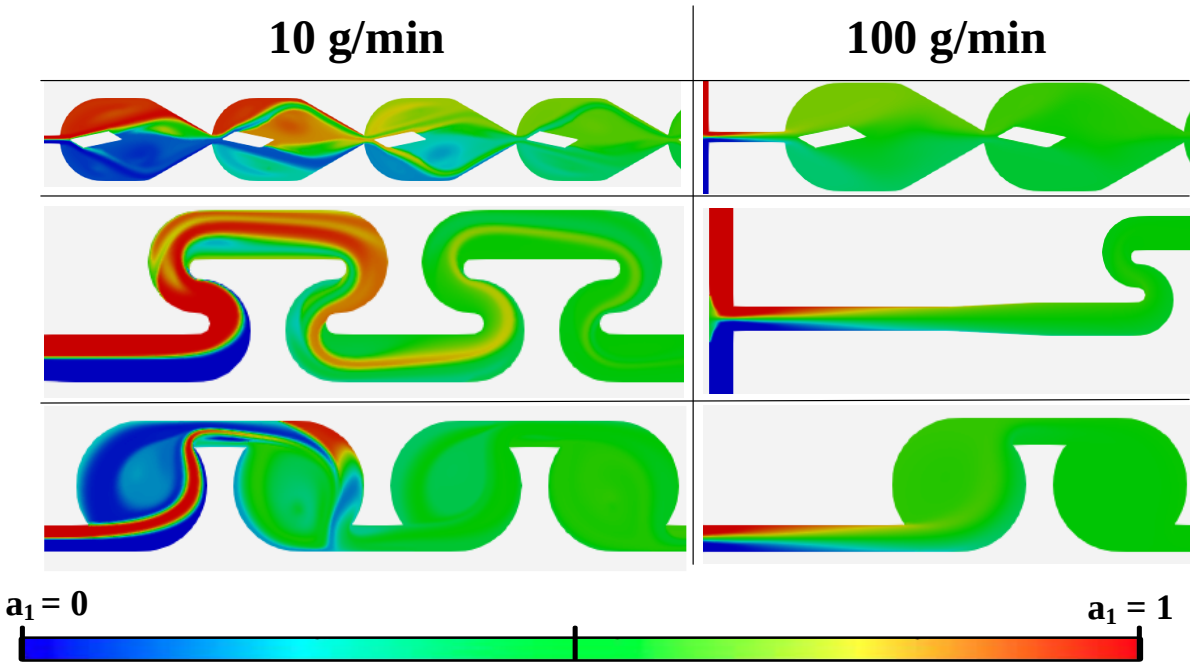

Figure 3.8. Mixture fraction (a_1) contour plots in the LLM, SZ and TG at symmetry plane (z = 0.625 mm) following the introduction of a passive scalar (a_1 = 1) through one T-junction inlet. Flow rates: 10 g/min (left) and 100 g/min (right)

Mathematically, the decay of small-scale-segregation emerges as the limiting mixing phenomenon once the large-scale-segregation variance approaches zero. Thus, t_{LSS} encompasses macromixing as a local quantity, but the true mixing time in much of the microreactor volume is dictated by t_{SSS}. Figure 3.9 presents the contour plots of the local t_{SSS} for different geometries as a function of flow rate. The mixing times are rescaled for each dataset to gain a better perception of the relative mixing quality at different locations within a given mixer. In the LLM and TG, the mixing quality appears to be lowest (red regions) in the eye of the main recirculation regions where there is some stagnant fluid. That characteristic mixing time is roughly an order of magnitude lower in the bypass zones (dark blue) compared to the recirculating volume. For the SZ, the

distribution of mixing times spans a narrower range, as the mixing appears to be most limited in the contracting bends and more efficient entering each straight region, albeit at comparable orders of magnitude.

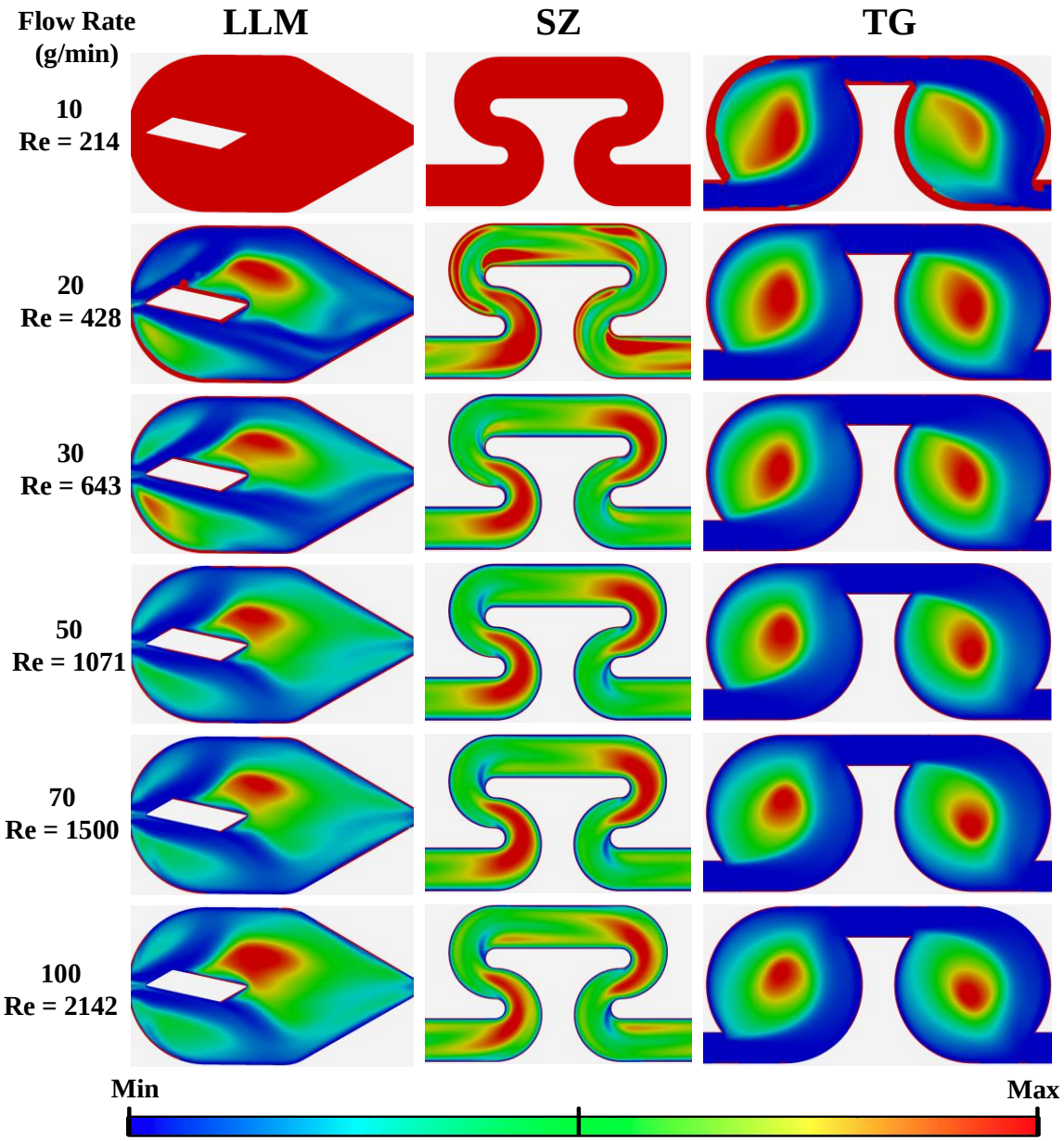

Figure 3.9. Time constant maps for the decay of small-scale segregation (t_{SSS}) in the LLM, SZ and TG at symmetry plane (z = 0.625 mm). The distribution of t_{SSS} is scaled differently for each geometry. For the LLM (in ms): [∞] (10 g/min); [5.1, 72.1] (20 g/min); [1.5, 22.7] (30 g/min); [0.62, 11.0] (50 g/min); [0.43, 7.64] (70 g/min); and [0.25, 4.24] (100 g/min). For the SZ (in ms): [∞] (10 g/min); [0.21, 1.74] (20 g/min); [0.098, 1.09] (30 g/min); [0.057, 0.654] (50 g/min); [0.042, 0.453] (70 g/min); and [0.021, 0.297] (100 g/min). For the TG (in ms): [5.1, 79.0] (10 g/min); [0.9, 16.3] (20 g/min); [0.6, 10.5] (30 g/min); [0.35, 6.18] (50 g/min); [0.23, 4.17] (70 g/min); and [0.15, 2.75] (100 g/min)

The inconsistent normalization of t_{SSS} displayed in Figure 3.9 makes it challenging to evaluate the impact of geometry on the MTD. Conversely, Figure 3.10 presents the logarithmic distribution of t_{SSS} at flow rates of 20, 50 and 100 g/min. It should be noted that the distribution of t_{SSS} in the LLM and SZ at 10 g/min could not be defined because the flow is completely laminar under these conditions. Nevertheless, the distribution shows that the MTD of the three modules resembles a log-normal distribution, spanning 2–4 orders of magnitude. In general, although the average mixing time clearly decreases as flow rate is increased, the distributions also all tend to broaden at higher flow, particularly because the value at the lower-bound tends to decrease. This suggests that certain high-velocity regions improve their mixing efficiency while advective transport in the more stagnant regions lags.

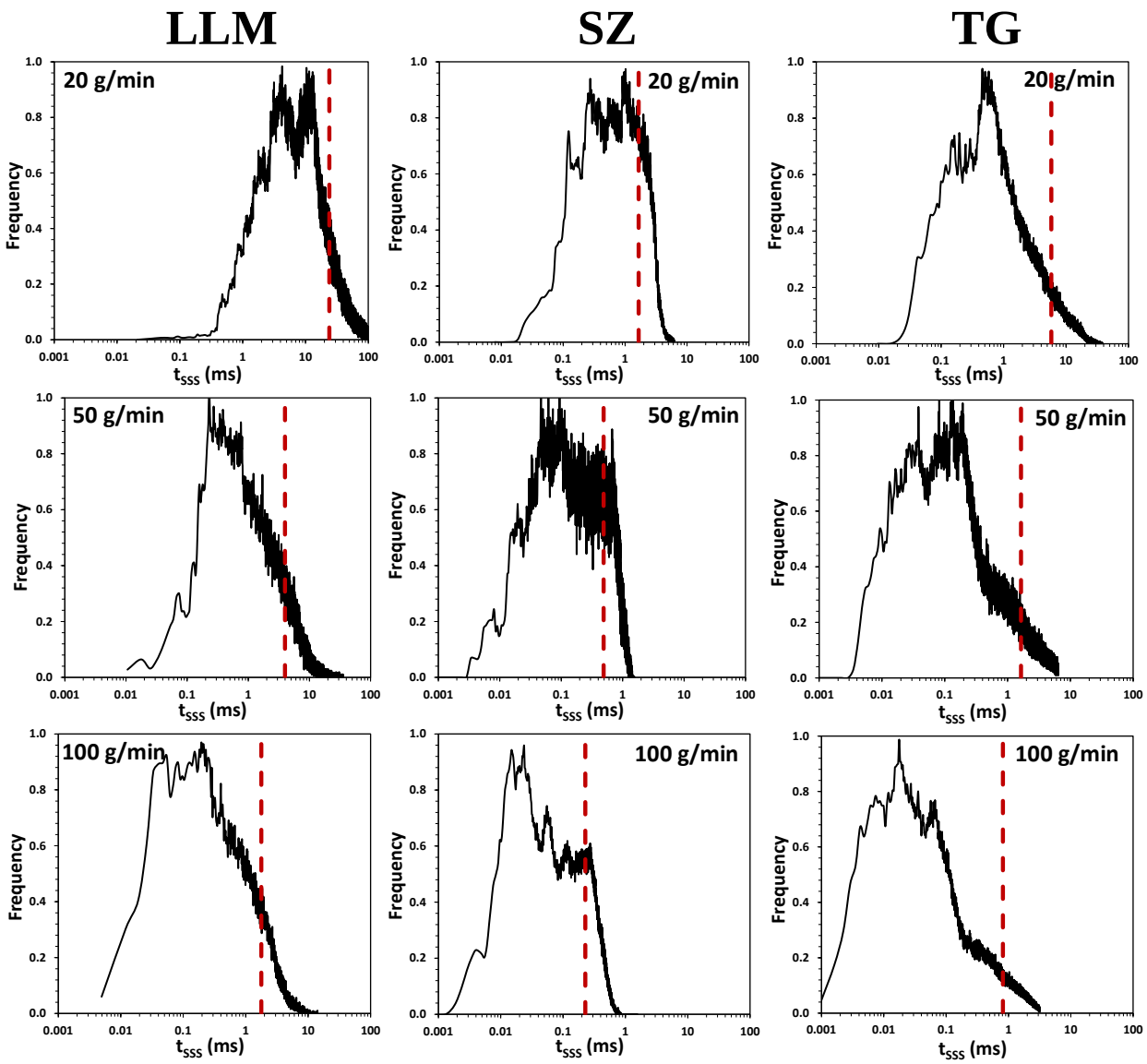

Figure 3.10. Logarithmic micromixing time distribution (t_{SSS}, in ms) conferred by the LLM, SZ and TG at 20, 50 and 100 g/min. Mean values of t_{SSS} are shown as red dashed lines

The mean mixing time constants ($\overline{t_{mix}}$) were computed from the MTD as a volume-weighted arithmetic mean of t_{SSS}. They were subsequently analyzed with respect to the average power dissipation, as shown in Figure 3.11, and validated by comparison to several highly published reduced-order mixing models, all of which stipulate that the mixing time scales inversely proportional to the power dissipation ($t_{mix} \propto 1/\varepsilon^n$) [3, 34, 90, 91]. Bourne and collaborators related the characteristic mixing time in vortex-dominated flow to two phenomena: engulfment and eddy deformation [90]. The following empirical correlations were thus derived from experimental data collected for a competitive-parallel reaction scheme to relate the mixing time

($t_{engulfment}$ or $t_{eddy\ deformation}$, depending on the limiting phenomenon) to the power dissipation:

$$t_{engulfment} = 17\left(\frac{\nu}{\varepsilon}\right)^{0.5} \tag{3.30}$$

$$t_{eddy\ deformation} = 2\left(\frac{\dot{v}}{\pi \bar{U} \varepsilon}\right)^{1/3} \tag{3.31}$$

The engulfment model also considers the molecular kinematic viscosity (ν) in addition to the power dissipation, whereas the eddy deformation model computes mixing quality as a function of volumetric flow rate ($\dot{v}$, in m^3/s). Falk and Commenge proposed an alternative correlation for relating the characteristic mixing time in single-phase flow through various micromixers to the power dissipation, albeit in a laminar flow regime [3]:

$$t_{mix} = 0.15\varepsilon^{-0.45} \tag{3.32}$$

The authors explicitly indicated that the above model fails to accurately quantify the mixing time in regimes of chaotic advection, as confirmed by the discrepancy between the calculated LLM, SZ and TG mixing times and this correlation.

The mixing time data presented in Figure 3.11 for the LLM, SZ and TG are clearly in excellent conformance with published reduced-order models for characterizing micromixing in chaotic or turbulent flow. For the LLM and SZ, the slope resembles that of the engulfment model, whereas the TG data lie closer to the eddy deformation model. However, at the lowest power dissipation, the latter geometry confers a mixing time that is closer to the laminar model due to the flow field being comprised mostly of pure bypassing. Moreover, the decrease in mixing time between 30 and 100 g/min is much less pronounced in the TG. This dampened part of the trend is likely attributed to a mixture of engulfment and eddy deformation in the streamlined bypass/recirculation and core recirculation zones, respectively. The mixing times predicted for each geometry using the present CFD model are all much lower than what is predicted using a laminar model over an equivalent average power dissipation. The overall MTD computations are summarized in Table 3.4.

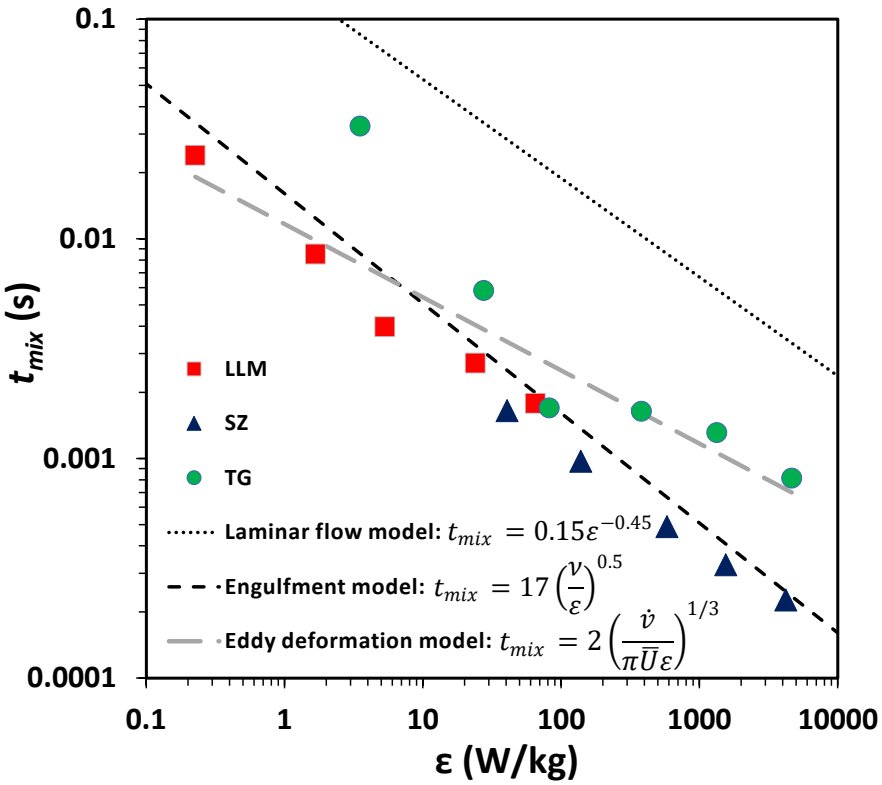

Figure 3.11. CFD predictions of the mean mixing time as a function of average power dissipation in comparison to existing reduced-order models [3, 90]. The laminar flow model was proposed by Falk and Commenge [34]

Table 3.4. Summary of the impact of geometry and flow rate on the characteristic micromixing time distribution. The mean time constant predicted through CFD is compared to an engulfment model proposed by Bourne for chaotic flow [90]

Flow Rate (g/min)	Required volume for $a_2 \rightarrow 0$ (mm^3)	Bounds t_{SSS} (ms)	$\overline{t_{SSS}}$ (ms)	$t_{engulfment}$ (ms)
		LLM		
10	165.3	∞	∞	19.17
20	82.64	[1.43, 75.8]	24.0	9.84
30	82.64	[0.36, 23.9]	8.52	6.69
50	41.32	[0.045, 11.6]	3.98	4.05
70	41.32	[0.035, 8.04]	2.72	2.90
100	41.32	[0.026, 4.46]	1.78	2.04
		SZ		
10	15.48	∞	∞	
20	7.74	[0.12, 1.83]	1.65	7.25
30	3.87	[0.042, 1.15]	0.972	3.80
50	3.87	[0.024, 0.687]	0.490	2.52
70	1.94	[0.020, 0.476]	0.329	1.56
100	1.94	[0.006, 0.312]	0.227	1.13
		TG		
10	14.27	[1.02, 83.1]	32.568	7.68
20	14.27	[0.094, 17.2]	5.812	3.86
30	7.14	[0.046, 11.0]	1.697	2.69
50	7.14	[0.022, 6.50]	1.640	1.61
70	7.14	[0.010, 4.39]	1.310	1.06
100	7.14	[0.0039, 2.89]	0.814	0.70

3.3.4. Simulation of competitive reaction pathway

As described in sections 3.2.2.4 and 3.2.3.4, a two-environment DQMOM-IEM model was used for reactive mixing simulations, wherein each fluid was introduced separately through their respective inlets of a T-junction. The purpose of defining two distinct fluids with identical physical properties was to simultaneously account for the blending time and the micromixing time when solving for the concentration of reacting species. In this study, instead of using the competitive-parallel reactions to estimate a micromixing time, this scheme was used to assess micromixing performance of the different geometries based on the predicted conversion of the slower reaction. The rate constant of reaction (II), k_2, was thus manipulated independently to mimic different conditions of mixing sensitivity defined by the second Damköhler number (Da_{II}):

$$Da_{II} = k_2 \, \overline{t_{mix}} \, C_0^{n-1} \tag{3.33}$$

where C_0 is the inlet concentration of reactant D or A (equimolar feed) after the two inlet streams become blended (but prior to their reaction occurring), and n is the order of the reaction (n = 2). The selection of t_{SSS} as a micromixing time constant is based on the notion that the extent of reaction is marginal prior to the complete decay of LSS (i.e., the reaction does not occur substantially until both fluid environments are blended). However, both t_{SSS} and t_{LSS} impact reactant conversion in truth. The system is said to be controlled by the intrinsic reaction kinetics when $Da_{II} \leq 0.001$, controlled by mixing limitations when $Da_{II} \geq 1000$, and influenced by both micromixing and reaction kinetics in the range of $0.001 < Da_{II} < 1000$ [92]. Each of these reaction conditions was simulated for the three mixers in question over an equivalent residence time of 90 ± 1.8 ms, as shown in Figure 3.12 for a flow rate of 50 g/min (an ideal operating flow rate for these geometries based on the onset of chaotic advection).

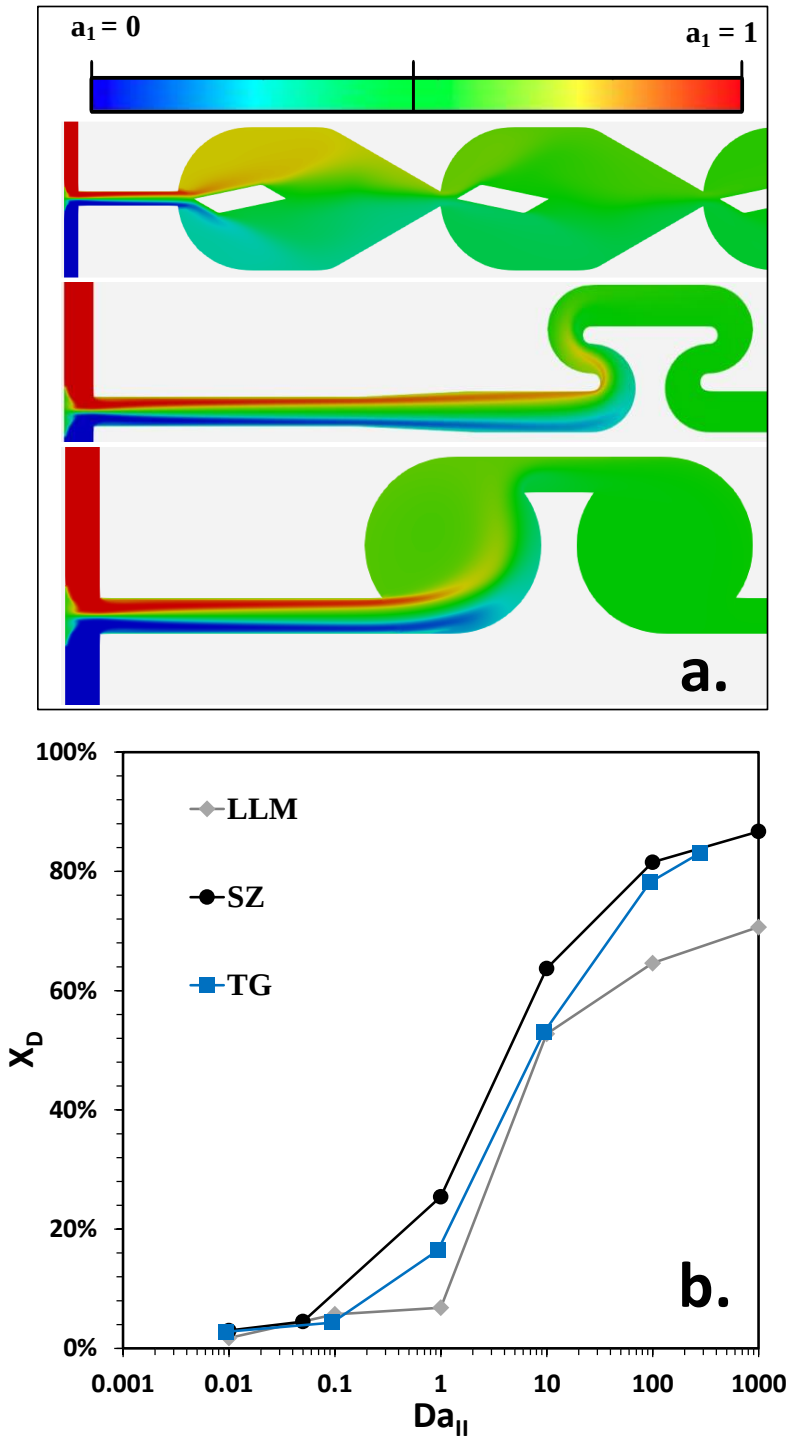

Figure 3.12. At 50 g/min: a. mixture fraction contour plots in the LLM, SZ and TG at symmetry plane (z = 0.625 mm) following the introduction of a passive scalar (a_1 = 1) through one T-junction inlet; b. the impact of mixer geometry on the conversion of reactant D in a second-order competitive-parallel reaction as a function of Da_{II} (i.e., a defined reaction rate constant for a given mixing time). Curves shown in b. are compared over an equivalent residence time of 90 $\pm$ 1.8 ms (V = 75 $\pm$ 1.5 mm^3)

The residence time in these simulations was long enough such that the consumption of species A was always greater than 95%. This was achieved by ensuring that the first Damköhler number (Da_I) was greater than 10, which is described as a ratio of residence time ($\bar{t}$) over the reaction time scale as follows:

$$Da_I = k_{rxn}\,\bar{t}\,C_0^{n-1} \tag{3.34}$$

As confirmed through Figure 3.12, the conversion of species D (X_D) was expected to increase with Da_{II} because, as k_2 increases relative to the quality of mixing, the apparent rate of reaction (II) becomes more comparable to that of reaction (I). For each geometry, there appears to be a different onset value of Da_{II} where the extent of reaction (II) begins to increase, which can be attributed to either LSS, SSS, or a combination of both. For the SZ, TG and LLM, this onset occurs at Da_{II} of 0.05, 0.1 and 1, respectively.

From a micromixing perspective, the MTD appears to be slightly skewed left in the SZ (i.e., more abrupt increase in mixing time frequency at the upper end of the t_{SSS} scale), whereas it is slightly right-skewed in the LLM and TG. This would mean that there is a greater fraction of volume in the SZ that is characterized by mixing times greater than the mean. Since k_2 was defined for each geometry separately based on the mean mixing time, an earlier onset in X_D (i.e., Da_{II}) may be attributed to a greater fraction of volume in the SZ being mixing-limited compared to the LLM and TG at a given Da_{II}. However, macromixing also has an impact on reaction yield.

From a macromixing perspective, the apparent difference in X_D onset may also be linked to the variance in RTD as well as the difference in blending time (i.e., the residence time needed for the mixture fraction to reach 0.5 and for LSS to completely decay). As shown in Figure 3.12a, it takes each geometry a different residence time for the mixture fraction to reach 0.5, and therefore the reaction yield is likely governed by both LSS and SSS. For example, the conversion in the LLM is likely more impacted by LSS given that it requires roughly 5 times more volume than the TG and 10 times more volume than the SZ to approach complete blending ($a_1 = 0.5$). This tends to shift the onset value of Da_{II} to an even larger value for the LLM than it would if SSS was the only mixing phenomenon dictating the reaction.

At the upper end of Da_{II}, X_D in the SZ appears to plateau much more noticeably once $Da_{II} > 100$, in similar to fashion to what occurs in an ideal plug-flow reactor when the residence

time is much greater than the apparent reaction time ($Da_I > 10$). In contrast, the conversion in the TG and LLM continues to increase with Da_{II} past $Da_{II} > 100$, but with a dampened slope compared to the $1 < Da_{II} < 100$ range. Since the TG and LLM promote much more fluid recirculation—and as such, mimic more of a mixed-flow reactor—it is reasonable that X_D continues to increase in these systems even under mixing-limited conditions. For each geometry, there appears to be a clear inflexion in Figure 3.12b in which mixing limitations become dominant over the intrinsic reaction rate. For a given reaction, this operating point and beyond should be avoided in microreactor design so that the apparent rate of reaction remains dictated by its intrinsic kinetics.

3.4. Conclusions

The purpose of the present study was to employ CFD to conduct a comparative analysis of single-phase liquid flow and mixing in different microreactor geometries. CFD simulations were completed in OpenFOAM at flow rates ranging from 10 to 100 g/min using a k-ω SSTLM model suitable for transitional and chaotic flow regimes.

Contour plots of the velocity magnitude show that the SZ promotes very little fluid recirculation at any given flow rate. Conversely, the LLM and TG exhibit coexistence of both streamlined flow and chaotic recirculation zones. The recirculation zones occupy approximately 65-75% of the fluid volume in the TG and 70-80% of it in the LLM. At higher flow rates, fluid recirculation grows larger in these modules, as the stagnant volume shrinks considerably from 10 to 50 g/min. Based on the velocity and turbulent viscosity profiles, the onset of chaotic secondary flows in all three geometries occurs for characteristic Reynolds numbers in the range of 500–1000.

Pressure loss incurred over a single mixing module is greatest in the TG, particularly at 100 g/min where ΔP is roughly 40 kPa. At this same high-end flow rate, the pressure loss in the SZ is approximately half of that in the TG; yet at 10 g/min, they are within 10% of one another. The pressure loss incurred in the LLM is considerably lower at any given flow rate because its fully-expanded zone is much less constricted compared to the SZ and TG. Considering the RTD, the SZ mimics a virtually plug-flow profile (as characterized by a $Pe \geq 100$) over a relatively small volume, as only 10 SZ units in series (77.4 mm^3) are needed to reach this benchmark at 50 g/min. The LLM and TG resemble more of a mixed flow pattern due to their inherent fluid recirculation characteristics. As such, their RTDs are much broader and right-skewed compared to the SZ, and they require several more modules in series to approach a plug-flow profile in terms of symmetry and narrowness. At 50 g/min, 65 LLM units (3105 mm^3) and 80 TG units (1142 mm^3) need to be configured in series to reach a $Pe \geq 100$.

A DQMOM-IEM solver was incorporated into the CFD model to predict the distribution of mixing times as well as reactive mixing in a competitive-parallel reaction scheme. The mean micromixing time decreases considerably from 20 to 100 g/min in any given geometry: dropping from 24 ms to 1.8 ms in the LLM, from 1.7 ms to 0.23 ms in the SZ, and from 5.8 ms to 0.81 ms in the TG. The MTD in the SZ is generally the narrowest, as the distribution spans 1–2 orders of magnitude. In the TG and LLM, the MTD is much broader as the mixing times in the eye of their recirculation

zones can be almost four orders of magnitude greater than at the extremity of this region where there is strong exchange with the high-velocity bypass stream. Overall, the mean mixing times computed through the CFD model provide good agreement with existing reduced-order models for regimes of chaotic advection, which stipulate that the mixing time scales inversely proportional to the average power dissipation. Finally, the predicted reaction yield for the competitive-parallel reaction scheme showed that Da_{II} computed based on the mean t_{SSS} provides useful information about whether the process will be limited by the intrinsic rate of reaction or by the rate of mass transfer, even though the reaction process is controlled by a combination of the RTD as well as loss of LSS and SSS.

3.5. Nomenclature

$-\Delta P$ pressure drop (kg/(m·s^2))

$\nabla \bar{P}$ mean pressure gradient (kg/(m·s^2))

$\nabla \bar{\mathbf{U}}$ mean velocity gradient (s^{-1})

$(\nabla \bar{\mathbf{U}})^T$ transpose of the mean velocity gradient (s^{-1})

a_1 mixture fraction (-)

a_2 mixture fraction variance (-)

a_3 LSS variance (-)

$\bar{a}$ mean mixture fraction (0.5)

C_μ turbulent viscosity coefficient

C_ϕ empirical mixing coefficient

C_T tracer concentration (mol/L)

c_{Ak} local concentration of species A in fluid environment *k* (mol/L)

c_{A0} initial concentration of species A (mol/L)

$\overline{c_A}$ average concentration of species A in both environments (mol/L)

c_{Bk} local concentration of species B in fluid environment *k* (mol/L)

c_{B0} initial concentration of species B (mol/L)

$\overline{c_B}$ average concentration of species B in both environments (mol/L)

c_{Dk} local concentration of species D in fluid environment *k* (mol/L)

c_{D0} initial concentration of species D (mol/L)

$\overline{c_D}$ average concentration of species D in both environments (mol/L)

$\overline{\overline{c_D}}$ mass-weighted average outlet concentration of species D in both environments (mol/L)

D_T molecular diffusion coefficient of the tracer (4.2×10^{-10} m^2/s)

Da_I first Damköhler number (-)

Da_{II} second Damköhler number (-)

E residence time distribution (s^{-1})

E_θ dimensionless residence time distribution (-)

$\mathbf{g}$ gravity vector (m/s^2)

k_2 rate constant of reaction 2 (s^{-1})

N number of ideal mixed tanks (-)

n order of reaction (-)

$\bar{P}$ mean pressure (Pa)

Pe Peclet number (-)

R^2 coefficient of determination (-)

Re Reynolds number (-)

$Re_{\theta,t}$ local momentum thickness Reynolds number (-)

Re_t local turbulent Reynolds number

$S_{2\infty}$ source term for reaction (II) coupled to an infinitely-fast reaction (I) (s^{-1})

Sc_t turbulent Schmidt number (unity)

t time (s)

$\bar{t}$ mean residence time (s)

$t_{eddy\ deformation}$ mixing time based on reduced-order eddy deformation model (s)

$t_{engulfment}$ mixing time based on reduced-order engulfment model (s)

t_{LSS} large-scale segregation decay time (s)

t_{mix} characteristic micromixing time (s)

$\overline{t_{mix}}$ mean micromixing time (s)

t_{SSS} small-scale segregation decay time (s)

$\bar{\mathbf{U}}$ mean velocity vector (m/s)

U_{min} minimum velocity magnitude (m/s)

U_{max} maximum velocity magnitude (m/s)

V reactor volume (mm^3)

V_{Pe100} volume of mixers in series needed to reach a Pe of 100 (mm^3)

$\dot{v}$ volumetric flow rate (mm^3/s)

X_1 mixture fraction in the first environment of the DQMOM-IEM model (-)

X_2 mixture fraction in the second environment of the DQMOM-IEM model (-)

X_D conversion of reactant D (%)

y^+ dimensionless wall distance (-)

$Y_{r,n}$ reaction progress variable for reaction r in environment n (-)

z depth coordinate (m)

Abbreviations

AD Axial dispersion (model)

AutoCAD Computer-aided design (software)

CFD Computational fluid dynamics

DQMOM Direct quadrature method of moments

GAMG Geometric-algebraic multi-grid (solver)

IEM Interaction by exchange with the mean

LL Liquid-liquid

LLM LL mixing module

LSS Large-scale segregation

MR Mixing region of a microreactor

MTD Mixing time distribution

OpenFOAM Open-source field operation and manipulation

PBiCGStab Stabilized preconditioned biconjugate gradient (solver)

PDF Probability density function

RTD Residence time distribution

SALOME CFD pre-processing software

SIMPLE Semi-implicit-method-for-pressure-linked-equations (algorithm)

SSS Small-scale segregation

SST Shear-stress transport

SSTLM SST w/ transition improvements by Langtry and Menter

SZ Type of symmetrical S-shaped mixing module

TG Tangential mixing module

Greek Letters

α_1 volume fraction of the first environment in the DQMOM-IEM model (-)

α_2 volume fraction of the second environment in the DQMOM-IEM model (-)

ε average turbulent kinetic energy dissipation rate (W/kg)

γ micromixing time parameter (s^{-1})

γ_{int} turbulence intermittency (-)

k turbulent kinetic energy (m^2/s^2)

μ molecular dynamic viscosity of the fluid (kg/(m·s))

ν molecular kinematic viscosity of the fluid (8.92×10^{-7} m^2/s)

ν_t turbulent kinematic viscosity of the fluid (m^2/s)

$\nu_{t,min}$ minimum turbulent kinematic viscosity of the fluid (m^2/s)

$\nu_{t,max}$ maximum turbulent kinematic viscosity of the fluid (m^2/s)

ω specific turbulent kinetic energy dissipation rate (s^{-1})

ρ fluid density (kg/m^3)

σ^2 variance (s^2)

$\sigma^2/\bar{t}^2$ dimensionless variance

θ dimensionless residence time (-)

Chapter 4. Conclusions and Future Research

4.1. Conclusions

The purpose of the present study was to a) develop and validate a CFD model for predicting the fluid dynamic characteristics of single-phase flow in microreactors, b) locally predict the velocity patterns and turbulent viscosity profiles in different passive mixing geometries, c) analyze the effect of mixing/spacing configuration on power dissipation and RTD from a global reactor perspective, and d) conduct a comparative analysis of the local macromixing and micromixing efficiency in the LLM, SZ and TG across characteristic Reynolds numbers ranging from 210 to 2140. CFD simulations presented herein were completed in OpenFOAM at flow rates ranging from 10 to 100 ml/min using a *k*-ω SST model suitable for transitional and chaotic flow regimes.

The first two objectives respond to a topic of interest – and perhaps one of debate – surrounding the use of turbulence modelling for simulating flow in microreactors, which presents certain challenges given that these units tend to operate in regimes of transition and chaotic advection. By validating the CFD predictions of pressure drop, RTD and turbulent kinetic energy in comparison to experimental and direct numerical simulation (DNS) results, it would instill more confidence in the use of inexpensive and versatile computational approaches to microreactor engineering in industry and academia. In addition, the latter two points listed above are also of great significance because they are examples of a more detailed investigation of the mixing performance via local velocity fields, blending profiles, RTD and MTD. There is a considerable amount of existing research on the individual characterization of these parameters through CFD, but none have gone about combining all of them to ultimately analyze reactor performance.

The validation study detailed in Chapter 2 concluded that the CFD simulation results were in excellent agreement with experimental pressure drop (R^2 > 0.997) and RTD data (R^2 > 0.97) obtained for four different configurations of LL reactors. These reactors differed with respect to the total number of mixers, as well as the length of the rectangular microchannels that interspaced these mixers. Pressure loss incurred through the microchannels was evidently much less than that endured across the heart of the mixing regions; however, the former tends to dampen the secondary flow patterns generated in the latter and therefore diminishes the radial transport and plug-flow profile of the overall reactor. Based on the effect of different mixing/spacing configurations on the

RTD, channels of 35 mm or shorter (i.e., in the LL4361) appear to yield the same degree of advective transport as a continuous series of LLMs (i.e., the LL4381) given that their RTDs are nearly identical at flow rates greater than 35 ml/min. For LL plates comprised of fewer mixing modules and longer microchannels (e.g., the LL4341 and LL4351), the RTD appears to broaden and exhibit back-end tailing because the longer channels interspacing the LLMs in these configurations allow the chaotic flow patterns to attenuate.

Contour plots of the velocity magnitude and turbulent viscosity show that all three geometries (LLM, SZ and TG) effectively generate chaotic flow structures by means of their unique passive mixing elements. The onset of chaotic advection occurs at Reynolds numbers in the range of 500–1000 for each mixer (i.e., 25–45 ml/min). However, secondary flow patterns are present in these structures across all flow rates studied herein. While the SZ confers very little fluid recirculation at any given flow rate, the LLM and TG exhibit coexistence of both streamlined flow and chaotic recirculation zones. The recirculation zones occupy approximately 65-75% of the fluid volume in the TG and 70-80% of it in the LLM. At higher flow rates, fluid recirculation grows larger in these modules, as the stagnant volume shrinks considerably from 10 to 50 ml/min.

Pressure loss through a single mixing module is greatest in the TG, particularly at 100 ml/min where ΔP is roughly 40 kPa. At this same high-end flow rate, the pressure loss in the SZ is roughly half of that; yet at 10 ml/min, the TG and SZ pressure losses are within 10% of one another. The pressure loss incurred in the LLM is considerably lower because its fully-expanded zone is much less constricted compared to the SZ and TG. The SZ mimics a virtually plug-flow profile (as characterized by a $Pe \geq 100$) over a relatively small volume, as only 10 SZ units in series (77.4 mm^3) are needed to reach this benchmark at 50 ml/min. The LLM and TG resemble more of a mixed-flow pattern due to their inherent fluid recirculation characteristics. As such, their RTDs are much broader and right-skewed compared to the SZ, and they require several more modules in series to approach a plug-flow profile in terms of symmetry and narrowness. At 50 ml/min, 65 LLM units (3105 mm^3) and 80 TG units (1142 mm^3) need to be configured in series to reach a $Pe \geq 100$.

In Chapter 3, a micromixing solver was incorporated into the CFD model to predict the distribution of mixing times as well as reactive mixing in a competitive-parallel reaction scheme. The mean micromixing time decreases considerably from 20 to 100 ml/min in any given geometry:

dropping from 24 ms to 1.8 ms in the LLM, from 1.7 ms to 0.23 ms in the SZ, and from 5.8 ms to 0.81 ms in the TG. The micromixing time distribution (MTD) in the SZ is generally the narrowest, as the distribution spans 1–2 orders of magnitude. The MTD is much broader in the TG and LLM as the mixing times in the eye of their recirculation zones can be almost four orders of magnitude greater than at the extremity of this region where there is strong exchange with the high-velocity bypass stream. Overall, the mean mixing times computed through CFD simulation are in good agreement with existing reduced-order models for regimes of chaotic advection, which stipulate that the mixing time scales inversely proportional to the average power dissipation. Finally, the predicted reaction yield for the competitive-parallel reaction scheme showed that the second Damköhler number (Da_{II}) computed based on the mean small-scale segregation time (t_{SSS}) provides useful information about whether the process will be limited by the intrinsic rate of reaction or by the rate of mass transfer, even though the reaction process is controlled by a combination of the RTD as well as loss of large-scale segregation and small-scale segregation.

In sum, this thesis describes a unique approach to the computational characterization of macromixing and micromixing in industrially-relevant microstructures. The three geometries studied herein encompass most of the passive mixing techniques published in the context of milli-/micro-scale reaction systems. The present CFD model proved to be capable of resolving the scales of mixing and flow structures occurring in these systems in both laminar and turbulent regimes. Moreover, the model is believed to be versatile enough for other passive mixing geometries and can be applied across a broader range of Reynolds number and reaction time scales than the ones investigated here. This research also highlights the advantages of CFD modelling over traditional methods of mixing and reaction characterization, particularly for its ability to locally resolve flow structures and transport processes that are much more challenging to characterize experimentally. As such, the numerical approach described in this work has the potential to be of tremendous value to the field of microreactor engineering, particularly for its ability to predict reaction yield through the computation of RTD and MTD for given kinetic data. The relationship between these parameters remains convoluted to some degree, even following the results in Figure 3.12, and is to be investigated further in future work. However, it is believed that the MTD and reaction yield should conform to one another, and that any deviation in their relationship is due to reactant blending effects in the entrance region.

4.2. Future research objectives

Future CFD studies will focus on the scale-up of micromixing geometries up to flow rates relevant across all three phases of clinical trials (i.e., 1–600 ml/min). Previous experimental work in LL microreactor scale-up concluded that the $3/7^{th}$ rule for scaling the flow rate over equivalent power dissipation was applicable under a fully isotropic turbulent regime. However, in the transitional flow regime, it was shown that the relative contribution of chaotic advection towards the overall friction factor increased proportionally to the Reynolds number. Therefore, this future work will provide added information pertaining to microreactor development and scale-up across a wider range of Reynolds numbers (i.e., flow regimes).

The present CFD model may also be applied to the simulation of oscillatory flow in coil reactors, which are often applied to reactions needing longer residence times. Coil flow reactors are said to dissipate energy at a rate that is an order of magnitude lower than LL micromixers at equivalent macromixing efficiency. Thus, by applying this same CFD model to different reactor geometries, it can potentially widen the scope of the existing toolbox approach for the development of microreactors suitable for a variety of reaction kinetics and reacting phases.

References

1. Plouffe P, Macchi A, Roberge DM (2014) From batch to continuous chemical synthesis-a toolbox approach. Org Process Res Dev 18:1286–1294 . https://doi.org/10.1021/op5001918

2. Raza W, Hossain S, Kim KY (2020) A review of passive micromixers with a comparative analysis. Micromachines 11:455 . https://doi.org/10.3390/MI11050455

3. Zhang J, Wang K, Teixeira AR, Jensen KF, Luo G (2017) Design and Scaling Up of Microchemical Systems: A Review. Annu Rev Chem Biomol Eng 8:285–305 . https://doi.org/10.1146/annurev-chembioeng-060816-101443

4. Jensen KF (2001) Microreaction engineering-is small better? Chem Eng Sci 56:293–303 . https://doi.org/10.1016/S0009-2509(00)00230-X

5. Roberge DM, Zimmermann B, Rainone F, Gottsponer M, Eyholzer M, Kockmann N (2008) Microreactor technology and continuous processes in the fine chemical and pharmaceutical industry: Is the revolution underway? Org Process Res Dev 12:905 . https://doi.org/10.1021/op8001273

6. Roberge DM, Ducry L, Bieler N, Cretton P, Zimmermann B (2005) Microreactor Technology: A Revolution for the Fine Chemical and Pharmaceutical Industries? Chem Eng Technol 28:318–323 . https://doi.org/10.1002/ceat.200407128

7. Kockmann N (2007) Transport Phenomena in Micro Process Engineering. Springer Science & Business Media

8. Bogdan AR, Dombrowski AW (2019) Emerging Trends in Flow Chemistry and Applications to the Pharmaceutical Industry. J Med Chem 62:6422–6468 . https://doi.org/10.1021/acs.jmedchem.8b01760

9. Baumann M, Moody TS, Smyth M, Wharry S (2020) A Perspective on Continuous Flow Chemistry in the Pharmaceutical Industry. https://doi.org/10.1021/acs.oprd.9b00524

10. Mielke E, Plouffe P, Koushik N, Eyholzer M, Gottsponer M, Kockmann N, MacChi A, Roberge DM (2017) Local and overall heat transfer of exothermic reactions in microreactor systems. React Chem Eng 2:763–775 . https://doi.org/10.1039/c7re00085e

11. Pashkova A, Greiner L (2011) Towards Small-Scale Continuous Chemical Production:

Technology Gaps and Challenges. Chemie Ing Tech 83:1337–1342 . https://doi.org/10.1002/cite.201100037

12. Plouffe P, Bittel M, Sieber J, Roberge DM, Macchi A (2016) On the scale-up of micro-reactors for liquid-liquid reactions. Chem Eng Sci 143:216–225 . https://doi.org/10.1016/j.ces.2015.12.009

13. Kockmann N, Gottsponer M, Roberge DM (2011) Scale-up concept of single-channel microreactors from process development to industrial production. Chem Eng J 167:718–726 . https://doi.org/10.1016/j.cej.2010.08.089

14. Taylor RA, Penney WR, Vo HX (2005) Scale-up methods for fast competitive chemical reactions in pipeline mixers. Ind Eng Chem Res 44:6095–6102 . https://doi.org/10.1021/ie040237u

15. Nieves-Remacha MJ, Kulkarni AA, Jensen KF (2015) OpenFOAM Computational Fluid Dynamic Simulations of Single-Phase Flows in an Advanced-Flow Reactor. Ind Eng Chem Res 54:7543–7553 . https://doi.org/10.1021/acs.iecr.5b00232

16. Mielke E, Plouffe P, Mongeon SS, Aellig C, Filliger S, Macchi A, Roberge DM (2018) Micro-reactor mixing unit interspacing for fast liquid-liquid reactions leading to a generalized scale-up methodology. Chem Eng J 352:682–694 . https://doi.org/10.1016/j.cej.2018.07.043

17. Hopley A, Doyle BJ, Roberge DM, Macchi A (2019) Residence time distribution in coil and plate micro-reactors. Chem Eng Sci 207:181–193 . https://doi.org/10.1016/j.ces.2019.06.016

18. Mielke E, Roberge DM, Macchi A (2016) Microreactor mixing-unit design for fast liquid-liquid reactions. J Flow Chem 6:279–287 . https://doi.org/10.1556/1846.2016.00026

19. Metzger L, Kind M (2016) On the mixing in confined impinging jet mixers – Time scale analysis and scale-up using CFD coarse-graining methods. Chem Eng Res Des 109:464–476 . https://doi.org/10.1016/j.cherd.2016.02.019

20. Cheng J, Feng X, Cheng D, Yang C (2012) Retrospect and perspective of micro-mixing studies in stirred tanks. Chinese J Chem Eng 20:178–190 . https://doi.org/10.1016/S1004-9541(12)60378-4

21. Vicum L, Ottiger S, Mazzotti M, Makowski Ł, Bałdyga J (2004) Multi-scale modeling of a reactive mixing process in a semibatch stirred tank. Chem Eng Sci 59:1767–1781 . https://doi.org/10.1016/j.ces.2004.01.032

22. Parvizian F, Rahimi M, Azimi N, Alsairafi AA (2014) CFD Modeling of Micromixing and Velocity Distribution in a 1.7-MHz Tubular Sonoreactor. Chem Eng Technol 37:113–122 . https://doi.org/https://doi.org/10.1002/ceat.201300231

23. Huang PH, Chan CY, Li P, Nama N, Xie Y, Wei CH, Chen Y, Ahmed D, Huang TJ (2015) A spatiotemporally controllable chemical gradient generator via acoustically oscillating sharp-edge structures. Lab Chip 15:4166–4176 . https://doi.org/10.1039/c5lc00868a

24. Huang PH, Chan CY, Li P, Wang Y, Nama N, Bachman H, Huang TJ (2018) A sharp-edge-based acoustofluidic chemical signal generator. Lab Chip 18:1411–1421 . https://doi.org/10.1039/c8lc00193f

25. Nama N, Huang PH, Huang TJ, Costanzo F (2016) Investigation of micromixing by acoustically oscillated sharp-edges. Biomicrofluidics 10:024124 . https://doi.org/10.1063/1.4946875

26. Aref H (1984) Stirring by chaotic advection. J Fluid Mech 143:1–21 . https://doi.org/10.1017/S0022112084001233

27. Stroock AD, Dertinger SKW, Ajdari A, Mezić I, Stone HA, Whitesides GM (2002) Chaotic mixer for microchannels. Science (80-) 295:647–651 . https://doi.org/10.1126/science.1066238

28. Liu RH, Stremler MA, Sharp K V., Olsen MG, Santiago JG, Adrian RJ, Aref H, Beebe DJ (2000) Passive mixing in a three-dimensional serpentine microchannel. J Microelectromechanical Syst 9:190–197 . https://doi.org/10.1109/84.846699

29. Ansari MA, kim KY (2009) Parametric study on mixing of two fluids in a three-dimensional serpentine microchannel. Chem Eng J 146:439–448 . https://doi.org/10.1016/j.cej.2008.10.006

30. Ansari MA, Kim KY (2010) Mixing performance of unbalanced split and recombine micomixers with circular and rhombic sub-channels. Chem Eng J 162:760–767 . https://doi.org/10.1016/j.cej.2010.05.068

31. Hossain S, Kim KY (2015) Mixing analysis in a three-dimensional serpentine split-and-recombine micromixer. Chem Eng Res Des 100:95–103 . https://doi.org/10.1016/j.cherd.2015.05.011

32. Feng X, Ren Y, Jiang H (2013) An effective splitting-and-recombination micromixer with self-rotated contact surface for wide Reynolds number range applications. Biomicrofluidics 7:054121 . https://doi.org/10.1063/1.4827598

33. Hossain S, Kim KY (2016) Parametric investigation on mixing in a micromixer with two-layer crossing channels. Springerplus 5:794 . https://doi.org/10.1186/s40064-016-2477-x

34. Falk L, Commenge JM (2010) Performance comparison of micromixers. Chem Eng Sci 65:405–411 . https://doi.org/10.1016/j.ces.2009.05.045

35. Commenge JM, Falk L (2011) Villermaux-Dushman protocol for experimental characterization of micromixers. Chem Eng Process Process Intensif 50:979–990 . https://doi.org/10.1016/j.cep.2011.06.006

36. Bošković D, Loebbecke S, Gross GA, Koehler JM (2011) Residence Time Distribution Studies in Microfluidic Mixing Structures. Chem Eng Technol 34:361–370 . https://doi.org/10.1002/ceat.201000352

37. Nieves-Remacha MJ, Yang L, Jensen KF (2015) OpenFOAM Computational Fluid Dynamic Simulations of Two-Phase Flow and Mass Transfer in an Advanced-Flow Reactor. Ind Eng Chem Res 54:6649–6659 . https://doi.org/10.1021/acs.iecr.5b00480

38. Shi X, Xiang Y, Wen LX, Chen JF (2012) CFD analysis of flow patterns and micromixing efficiency in a Y-type microchannel reactor. Ind Eng Chem Res 51:13944–13952 . https://doi.org/10.1021/ie300985q

39. An H, Li A, Sasmito A, Kurnia J (2012) Computational fluid dynamics (CFD) analysis of micro-reactor performance: Effect of various configurations. Chem Eng Sci 75:85–95 . https://doi.org/https://doi.org/10.1016/j.ces.2012.03.004

40. Fletcher D, Avila M, Poux M, Xuereb C, Aubin J, Fletcher D (2018) CFD Modelling of Micromixing in a T-mixer with Square Bends. In: European Conference on Mixing

41. Bodla VK, Seerup R, Krühne U, Woodley JM, Gernaey K V. (2013) Microreactors and

CFD as Tools for Biocatalysis Reactor Design: A case study. Chem Eng Technol 36:1017–1026 . https://doi.org/10.1002/ceat.201200667

42. Akiti O, Armenante PM (2004) Experimentally-validated micromixing-based CFD model for fed-batch stirred-tank reactors. AIChE J 50:566–577 . https://doi.org/https://doi.org/10.1002/aic.10051

43. Ouyang Y, Xiang Y, Gao X-Y, Zou H-K, Chu G-W, Agarwal RK, Chen J-F (2019) Micromixing efficiency optimization of the premixer of a rotating packed bed by CFD. Chem Eng Process - Process Intensif 142: . https://doi.org/https://doi.org/10.1016/j.cep.2019.107543

44. Guo TY, Shi X, Chu GW, Xiang Y, Wen LX, Chen JF (2016) Computational fluid dynamics analysis of the micromixing efficiency in a rotating-packed-bed reactor. Ind Eng Chem Res 55:4856–4866 . https://doi.org/10.1021/acs.iecr.6b00213

45. Cheng K, Liu C, Guo T, Wen L (2019) CFD and experimental investigations on the micromixing performance of single countercurrent-flow microchannel reactor. Chinese J Chem Eng 27:1079–1088 . https://doi.org/https://doi.org/10.1016/j.cjche.2018.11.026

46. Zhendong L, Yangcheng L, Jiawei W, Guangsheng L (2012) Mixing characterization and scaling-up analysis of asymmetrical T-shaped micromixer: Experiment and CFD simulation. Chem Eng J 181–182:597–606 . https://doi.org/https://doi.org/10.1016/j.cej.2011.11.105

47. Ouyang Y, Xiang Y, Zou H, Chu G, Chen J (2017) Flow characteristics and micromixing modeling in a microporous tube-in-tube microchannel reactor by CFD. Chem Eng J 321:533–545 . https://doi.org/https://doi.org/10.1016/j.cej.2017.03.151

48. McDonough JR, Oates MF, Law R, Harvey AP (2019) Micromixing in oscillatory baffled flows. Chem Eng J 361:508–518 . https://doi.org/10.1016/j.cej.2018.12.088

49. Wang L, Fox RO (2004) Comparison of micromixing models for CFD simulation of nanoparticle formation. AIChE J 50:2217–2232 . https://doi.org/10.1002/aic.10173

50. Fox RO (2003) Computational Models for Turbulent Reacting Flows. Cambridge University Press

51. Liu Y, Fox RO (2006) CFD predictions for chemical processing in a confined impinging-jets reactor. AIChE J 52:731–744 . https://doi.org/10.1002/aic.10633

52. Liu Y, Cheng C, Liu Y, Prud'homme RK, Fox RO (2008) Mixing in a multi-inlet vortex mixer (MIVM) for flash nano-precipitation. Chem Eng Sci 63:2829–2842 . https://doi.org/10.1016/j.ces.2007.10.020

53. Gavi E, Marchisio DL, Barresi AA (2007) CFD modelling and scale-up of Confined Impinging Jet Reactors. Chem Eng Sci 62:2228–2241 . https://doi.org/10.1016/j.ces.2006.12.077

54. Marchisio DL (2009) Large Eddy Simulation of mixing and reaction in a Confined Impinging Jets Reactor. Comput Chem Eng 33:408–420 . https://doi.org/10.1016/j.compchemeng.2008.11.009

55. Rizzotto M, Florit F, Rota R, Busini V (2019) A CFD hybrid approach to simulate liquid-phase chemical reactors. Chem Eng J 377:120365 . https://doi.org/10.1016/j.cej.2018.11.063

56. Weller H (2015) OpenFOAM | Free CFD Software | The OpenFOAM Foundation. https://openfoam.org/. Accessed 8 May 2020

57. Holvey CP, Roberge DM, Gottsponer M, Kockmann N, Macchi A (2011) Pressure drop and mixing in single phase microreactors: Simplified designs of micromixers. Chem Eng Process Process Intensif 50:1069–1075 . https://doi.org/10.1016/j.cep.2011.05.016

58. Kockmann N (2007) Transport Phenomena in Micro Process Engineering. Springer Science & Business Media

59. Könözsy L (2019) A New Hypothesis on the Anisotropic Reynolds Stress Tensor for Turbulent Flows Volume I : Theoretical Background and Development of an Anisotropic Hybrid k-omega Shear-Stress Transport/Stochastic Turbulene Model. Springer International Publishing, pp 57–66

60. Adrian RJ, Christensen KT, Liu ZC (2000) Analysis and interpretation of instantaneous turbulent velocity fields. Exp Fluids 29:275–290 . https://doi.org/10.1007/s003489900087

61. Menter FR, Langtry RB, Likki SR, Suzen YB, Huang PG, Völker S (2006) A correlation-

based transition model using local variables - Part I: Model formulation. J Turbomach 128:413–422 . https://doi.org/10.1115/1.2184352

62. Menter FR, Langtry R, Völker S (2006) Transition Modelling for General Purpose CFD Codes. Flow, Turbul Combust 77:277–303 . https://doi.org/10.1007/s10494-006-9047-1

63. Langtry RB, Menter FR (2009) Correlation-based transition modeling for unstructured parallelized computational fluid dynamics codes. AIAA J 47:2894–2906 . https://doi.org/10.2514/1.42362

64. Argyropoulos CD, Markatos NC (2015) Recent advances on the numerical modelling of turbulent flows. Appl Math Model 39:693–732 . https://doi.org/10.1016/j.apm.2014.07.001

65. Moukalled F, Mangani L, Darwish M (2016) The finite volume method in computational fluid dynamics :Fluid Mechanics and Its Applications

66. Holzmann T (2017) Mathematics, Numerics, Derivations and OpenFOAM

67. Levenspiel O (1999) Chemical Reaction Engineering, 3rd ed. Industrial & engineering chemistry research

68. Kumar J, Kukreja VK (2019) Analytic solution of a diffusion dispersion model of packed bed of finite thickness. J Interdiscip Math 22:1–16 . https://doi.org/10.1080/09720502.2015.1026466

69. Rojahn P, Hessel V, Nigam KDP, Schael F (2018) Applicability of the axial dispersion model to coiled flow inverters containing single liquid phase and segmented liquid-liquid flows. Chem Eng Sci 182:77–92 . https://doi.org/10.1016/j.ces.2018.02.031

70. Wu HY, Cheng P (2003) Friction factors in smooth trapezoidal silicon microchannels with different aspect ratios. Int J Heat Mass Transf 46:2519–2525 . https://doi.org/10.1016/S0017-9310(03)00106-6

71. Peng XF, Peterson GP (1996) Convective heat transfer and flow friction for water flow in microchannel structures. Int J Heat Mass Transf 39:2599–2608 . https://doi.org/10.1016/0017-9310(95)00327-4

72. Mohiuddin Mala G, Li D (1999) Flow characteristics of water in microtubes. Int J Heat Fluid Flow 20:142–148 . https://doi.org/10.1016/S0142-727X(98)10043-7

73. Ouyang Y, Zou H, Gao X, Chu G (2018) Computational fluid dynamics modeling of viscous liquid flow characteristics and end effect in rotating packed bed. Chem Eng Process - Process Intensif 123:185–194 . https://doi.org/https://doi.org/10.1016/j.cep.2017.09.005

74. Han LS (1960) Hydrodynamic entrance lengths for incompressible laminar flow in rectangular ducts. J Appl Mech 27:403–409 . https://doi.org/https://doi.org/10.1115/1.3644015

75. Costaschuk D, Elsnab J, Petersen S, Klewicki JC, Ameel T (2007) Axial static pressure measurements of water flow in a rectangular microchannel. Exp Fluids 43:907–916 . https://doi.org/10.1007/s00348-007-0360-9

76. Ham J-H, Platzer B (2004) Semi-Empirical Equations for the Residence Time Distributions in Disperse Systems - Part 1: Continuous Phase. Chem Eng Technol 27:1172–1178 . https://doi.org/10.1002/ceat.200407038

77. Elvira KS, I Solvas XC, Wootton RCR, Demello AJ (2013) The past, present and potential for microfluidic reactor technology in chemical synthesis. Nat. Chem. 5:905–915

78. Gutmann B, Cantillo D, Kappe CO (2015) Continuous-flow technology - A tool for the safe manufacturing of active pharmaceutical ingredients. Angew. Chemie - Int. Ed. 54:6688–6728

79. Song H, Chen DL, Ismagilov RF (2006) Reactions in droplets in microfluidic channels. Angew. Chemie - Int. Ed. 45:7336–7356

80. SALOME Platform. https://www.salome-platform.org/. Accessed 14 Dec 2020

81. Könözsy L (2019) A New Hypothesis on the Anisotropic Reynolds Stress Tensor for Turbulent Flows Volume I : Theoretical Background and Development of an Anisotropic Hybrid k-omega Shear-Stress Transport/Stochastic Turbulene Model. Springer International Publishing

82. Yang Z, Shih TH (1993) New time scale based k-epsilon model for near-wall turbulence. AIAA J 31:1191–1198 . https://doi.org/10.2514/3.11752

83. Dhakal TP, Walters DK (2009) Curvature and rotation sensitive variants of the K-omega SST turbulence model. In: Proceedings of the ASME Fluids Engineering Division Summer

Conference 2009, FEDSM2009. American Society of Mechanical Engineers Digital Collection, pp 2221–2229

84. Menter FR (1992) Influence of freestream values on k-ω turbulence model predictions. AIAA J. 30:1657–1659

85. Cheng JC, Fox RO (2010) Kinetic modeling of nanoprecipitation using CFD coupled with a population balance. Ind Eng Chem Res 49:10651–10662 . https://doi.org/10.1021/ie100558n

86. Raza W, Hossain S, Kim KY (2018) Effective mixing in a short serpentine split-and-recombination micromixer. Sensors Actuators, B Chem 258:381–392 . https://doi.org/10.1016/j.snb.2017.11.135

87. Hossain S, Kim K-Y (2015) Mixing Performance of a Serpentine Micromixer with Non-Aligned Inputs. Micromachines 6:842–854 . https://doi.org/10.3390/mi6070842

88. Hsiao K-Y, Wu C-Y, Huang Y-T (2014) Fluid mixing in a microchannel with longitudinal vortex generators. Chem Eng J 235:27–36 . https://doi.org/10.1016/J.CEJ.2013.09.010

89. Fogler HS (2016) Elements of Chemical Reaction Engineering, 5th ed. Prentice Hall

90. Bourne JR (2003) Mixing and the selectivity of chemical reactions. Org Process Res Dev 7:471–508 . https://doi.org/10.1021/op020074q

91. Raza W, Hossain S, Kim KY (2020) A review of passive micromixers with a comparative analysis. Micromachines 11

92. Gobert SRL, Kuhn S, Braeken L, Thomassen LCJ (2017) Characterization of Milli- and Microflow Reactors: Mixing Efficiency and Residence Time Distribution. Org Process Res Dev 21:531–542 . https://doi.org/10.1021/acs.oprd.6b00359

Appendices

Appendix A. RTD Data Analysis [67, 76, 89]

RTD curves were obtained via transient simulation of a tracer pulse (Δt = 1.4 ms) transported through the LL reactor as a passive scalar. The exiting concentration at all face centre points ($C_{i,k}$) and the axial velocity at all face centre points ($U_{x,i,k}$) for faces having an area of A_k across the outlet patch were used to compute the mass-weighted average outlet concentration ($C_{out,i}$). In the following equations, i denotes a time step and *k* denotes a face on the outlet patch.

$$C_{out,i} = \frac{\sum_k C_{i,k} U_{x,i,k} A_k}{\sum_k U_{x,i,k} A_k} \tag{A-1}$$

The mean residence time ($\bar{t}$) was computed via Eq. A-2 and compared to the nominal space time (τ), the latter of which is based strictly on the reactor volume (V) over the average volumetric flow rate ($\dot{v}$). The former represents the first moment of the RTD curve.

$$\bar{t} = \frac{\sum_i t_i C_{out,i} \Delta t_i}{\sum_i C_{out,i} \Delta t_i} \tag{A-2}$$

$$\tau = \frac{V}{\dot{v}} \tag{A-3}$$

The RTD (E_i, in s^{-1}) was computed by simply changing the concentration scale such that the area under the curve is unity.

$$E_i = \frac{C_{out,i}}{\sum C_{out,i} \Delta t_i} \tag{A-4}$$

The dimensionless RTD (E_θ)—normalized with respect to the mean residence time—is used more often for comparing RTD curves at different flow rates for different reactors, as was done in this study by means of the following equations:

$$\theta_i = \frac{t_i}{\bar{t}} \tag{A-5}$$

$$E_\theta(\theta) = \bar{t} E(t) \tag{A-6}$$

where θ_i denotes the dimensionless time. The second moment of the RTD curve is the variance (σ^2):

$$\sigma^2 = \sum(t_i - \bar{t})^2 E_i \, \Delta t_i \tag{A-7}$$

A low variance is indicative of a narrow RTD, greater radial mixing, and greater resemblance to a plug-flow profile. Alternatively, the dimensionless variance ($\frac{\sigma^2}{\bar{t}^2}$) may be used to characterize the narrowness of the RTD curve and can be analytically linked to the Peclet number (*Pe*) as follows:

$$\frac{\sigma^2}{\bar{t}^2} = \frac{2Pe+8}{Pe^2+4Pe+4} \tag{A-8}$$

Physically, *Pe* represents the rate of mass transfer due to advection relative to the rate of mass transfer due to axial dispersion (AD). The AD model is a single-parameter model based on *Pe* that is used to predict the dimensionless RTD in non-ideal flow patterns that approach plug flow. It assumes a perfectly symmetrical RTD. A $Pe > 100$ is indicative of near-plug-flow behaviour.

$$E_\theta(\theta) = \frac{1}{2}\sqrt{\frac{Pe}{\pi\theta}} exp\left\{-\frac{Pe(1-\theta)^2}{(4\theta)}\right\} \tag{A-9}$$

The above model proved to fit reasonably to the RTD of the LL4381 and LL4361 configurations. However, back-end tailing observed in the RTD curves of the LL4351 and LL4341 configurations (due to the attenuation of secondary flow patterns in the RTC) require a more complex, multi-parameter model that accounts for asymmetry. The semi-empirical Ham and Platzer model is a multi-parameter model described by the following equations:

$$E_\theta(\theta) = \frac{8M\theta_k^M}{\theta^{M+1}}\left(1 - \frac{\theta}{\theta_{max}}\right)^{M-1}\left[1 - \frac{\theta_k^M}{\theta^M}\left(1 - \frac{\theta}{\theta_{max}}\right)^M\right]^7 \tag{A-10}$$

$$\theta_k = \frac{\theta_{min}\theta_{max}}{\theta_{max}-\theta_{min}} \tag{A-11}$$

where θ_{min} and θ_{max} represent the dimensionless breakthrough time and end time, respectively, while *M* is an additional parameter used to adequately fit any given E_θ curve.

Appendix B. Supplementary Figures

Chapter 2. CFD Simulation of Pressure Drop and Macromixing in LL Microreactors

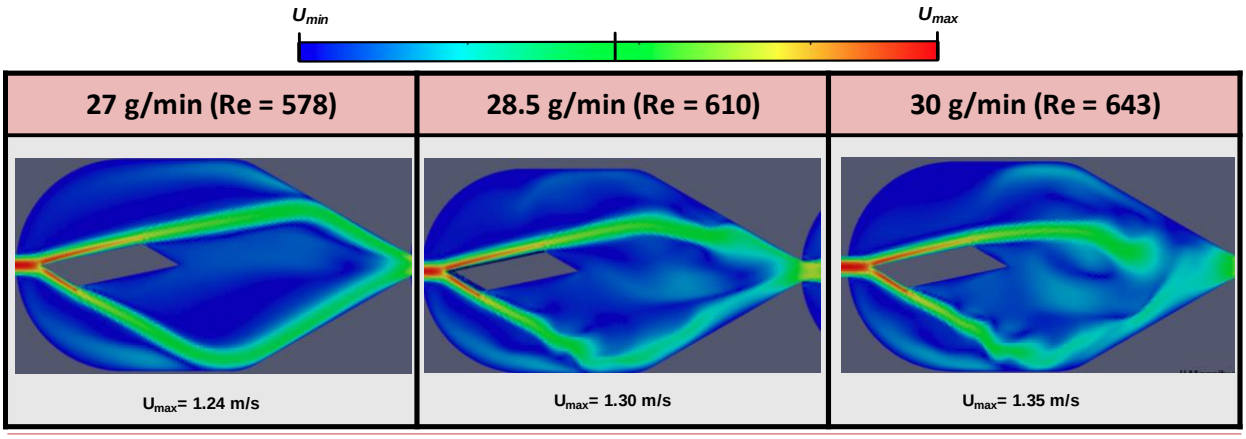

Figure B-2.1. 2D colour plot of velocity magnitude over the center plane (z = 0.625 mm) of LLM for steady-state simulations completed without turbulence modelling. Direction of flow is left to right

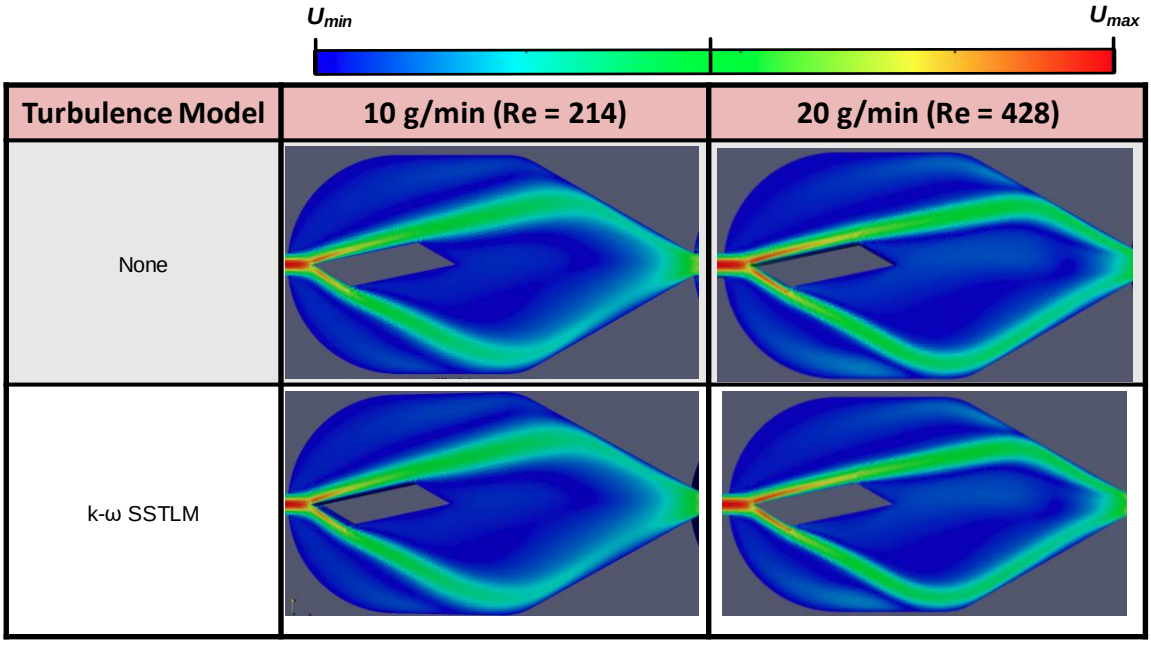

Figure B-2.2. 2D colour plot of velocity magnitude over the center plane (z = 0.625 mm) of LLM with (bottom) and without (top) turbulence modelling. Direction of flow is left to right

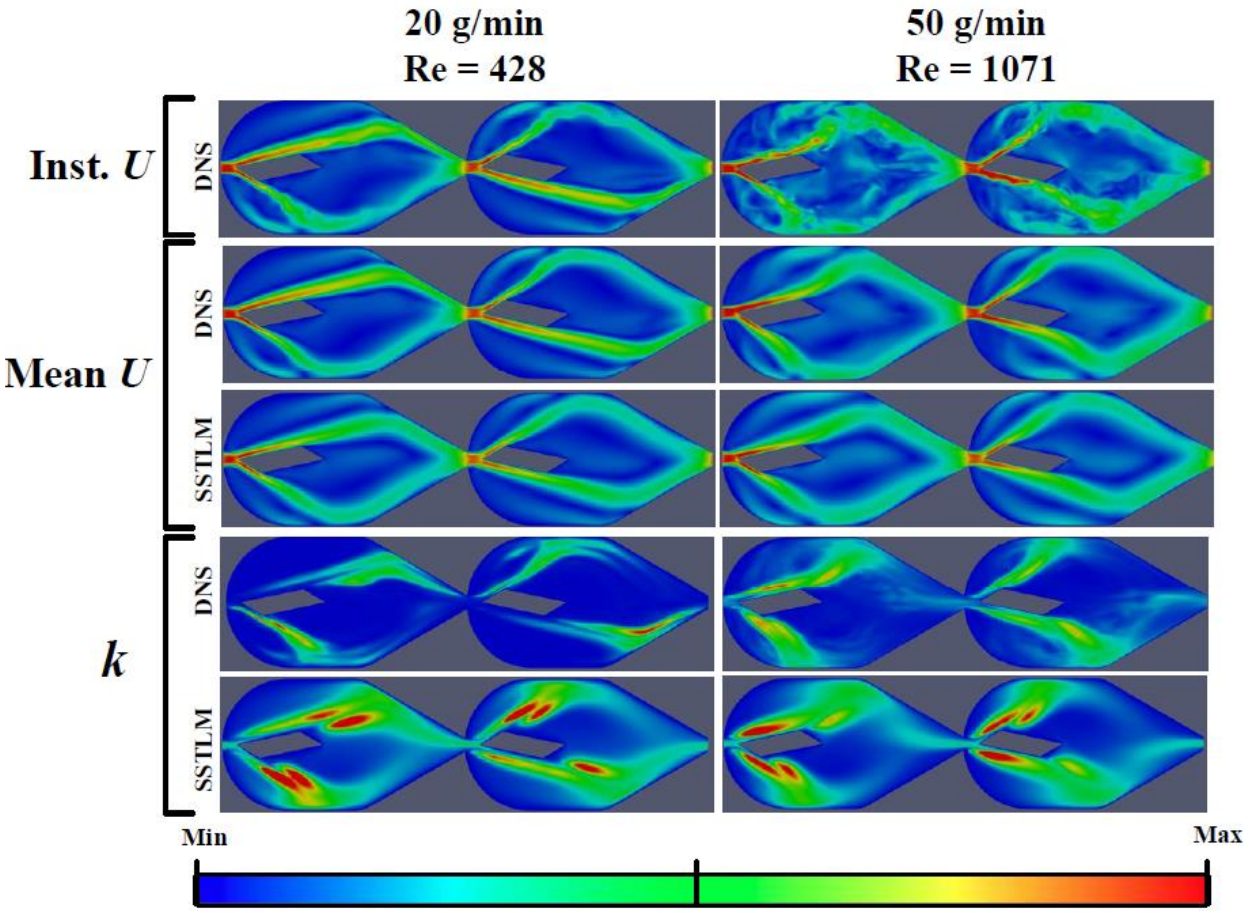

Figure B-2.3. 2D colour plots of velocity magnitude and turbulent kinetic energy over the center plane (z = 0.625 mm) for flow rates of 20 and 50 g/min obtained using SSTLM and DNS. For the 20 g/min flow rate, U_{min} = 0 (blue) and U_{max} = 0.7 m/s (red), and k_{min} = 0 (blue) and k_{max} = 0.01 m^2/s^2 (red). For the 50 g/min flow rate, U_{min} = 0 (blue) and U_{max} = 1.7 m/s (red), and k_{min} = 0 (blue) and k_{max} = 0.15 m^2/s^2 (red). DNS results for the 20 and 50 g/min flow rates were time averaged over 0.1 s and 0.05 s, respectively. Direction of flow is from left to right

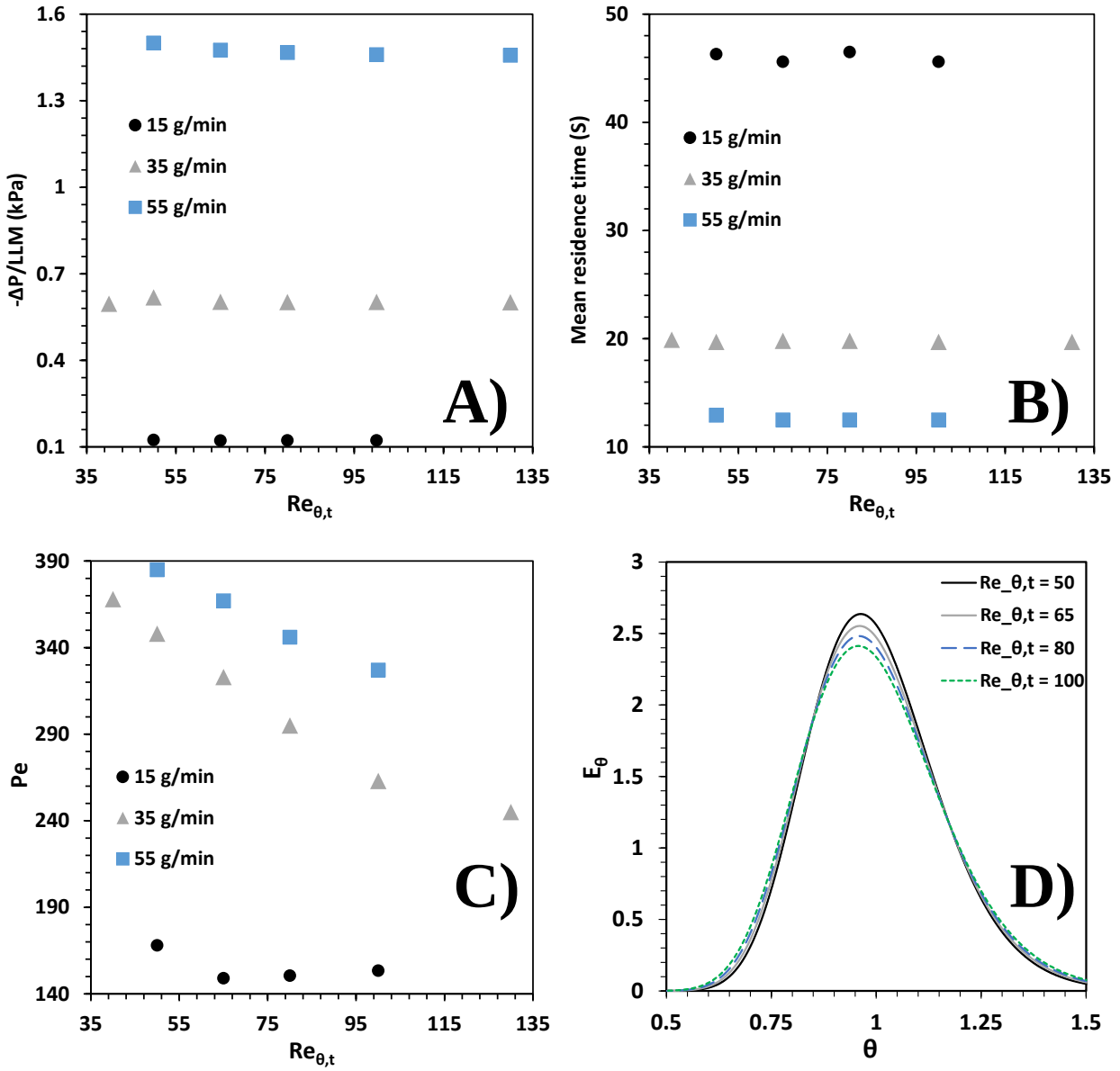

Figure B-2.4. Effect of the inlet value of the momentum thickness Reynolds number ($Re_{\theta,t}$) on the pressure drop per LLM (A), the mean residence time (B), and the Peclet number (C). The latter trend is made evident by the broadness of the dimensionless RTD curve (E_θ) for different $Re_{\theta,t}$ values at 55 g/min (D). Results are for CFD simulations completed over a domain of 49 LLMs

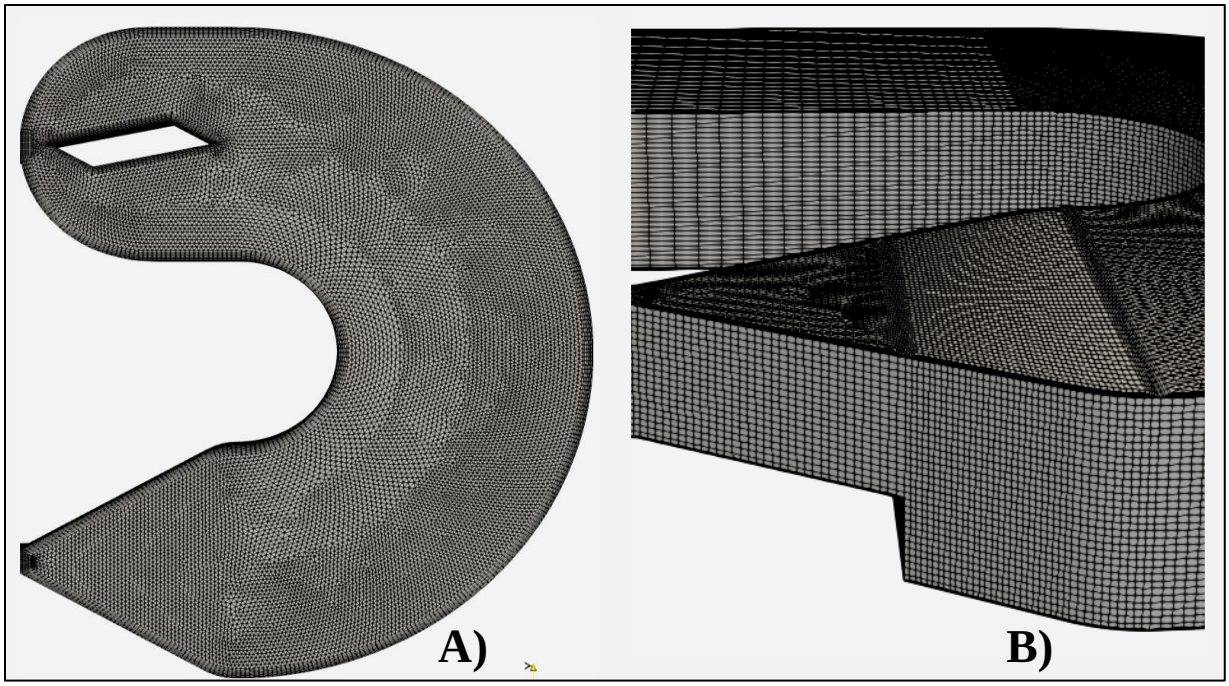

Figure B-2.5. 3D mesh of additional repeating segments in the LL microreactors. (A) Top view of the large LL module (611 960 cells in 3D); (B) Side view of the hydraulic contraction found at the end of an RTC

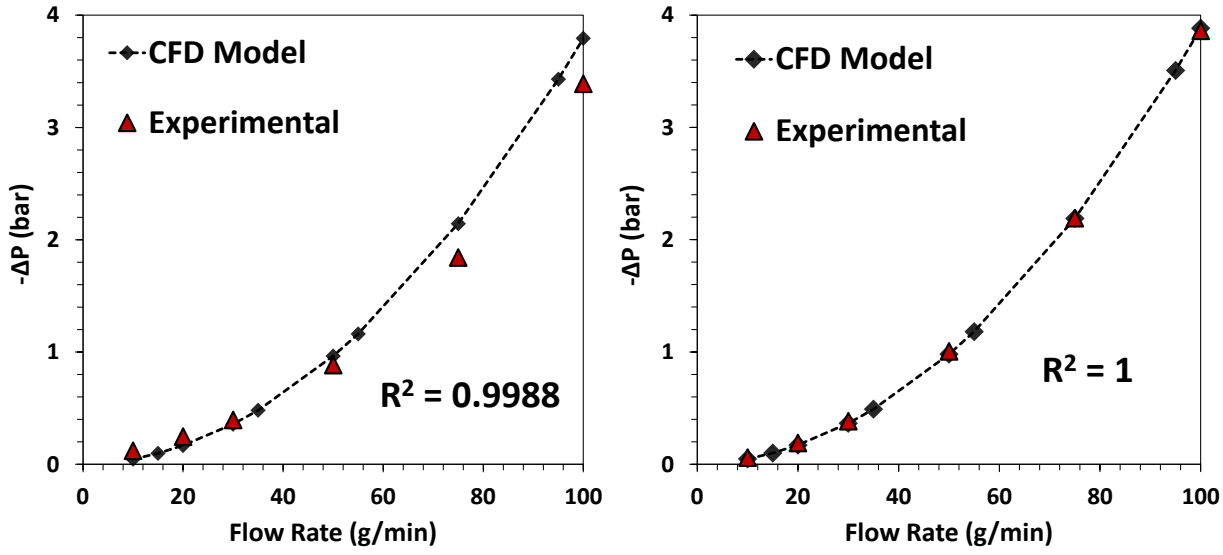

Figure B-2.6. Validation of pressure drop predictions in LL4341 (left) and LL4361 (right) as a function of flow rate

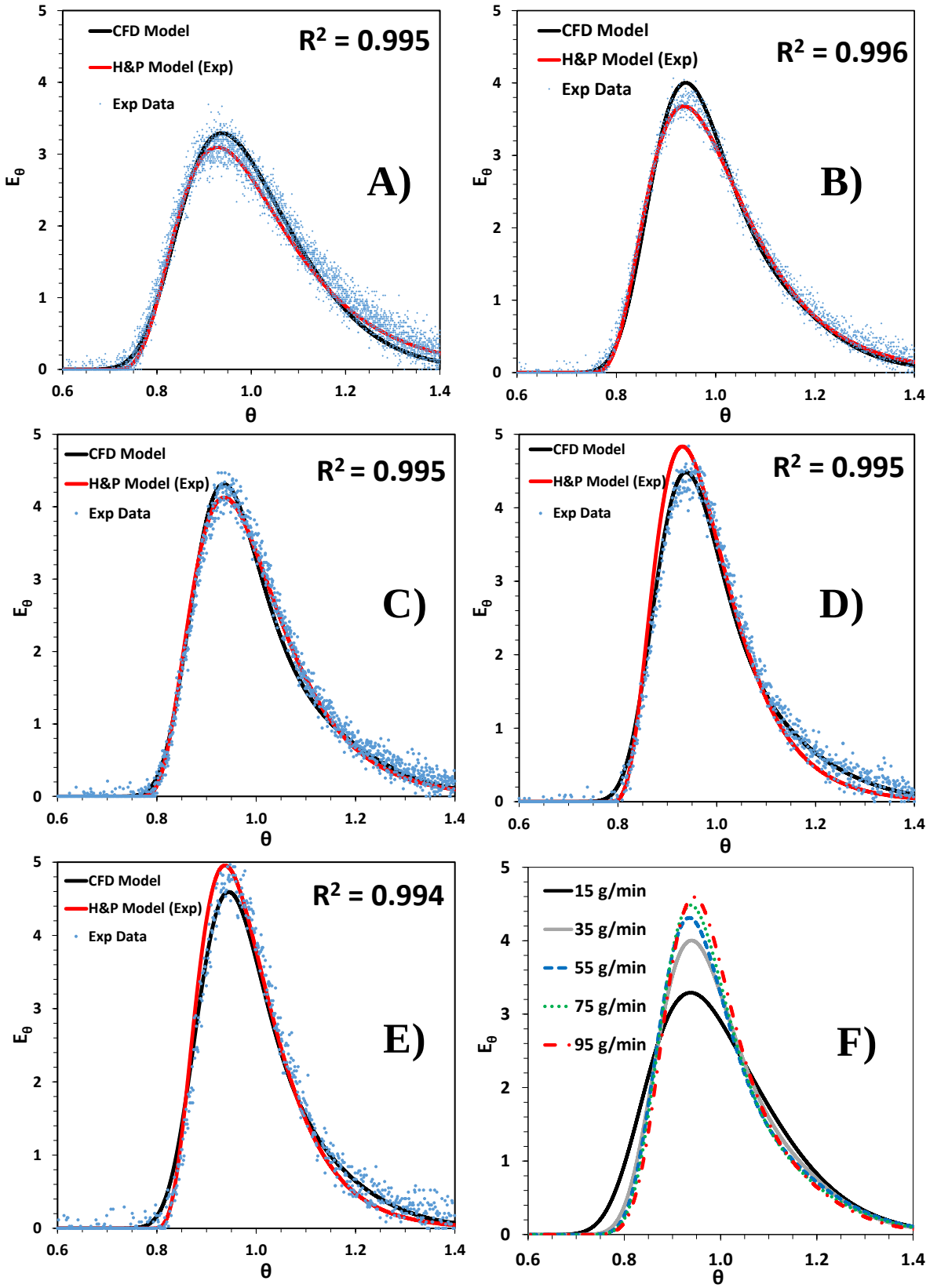

Figure B-2.7. Validation of macromixing performance in LL4341 via dimensionless RTD (E_θ) predictions at flow rates (g/min) of A) 15, B) 35, C) 55, D) 75, E) 95, and (F) all

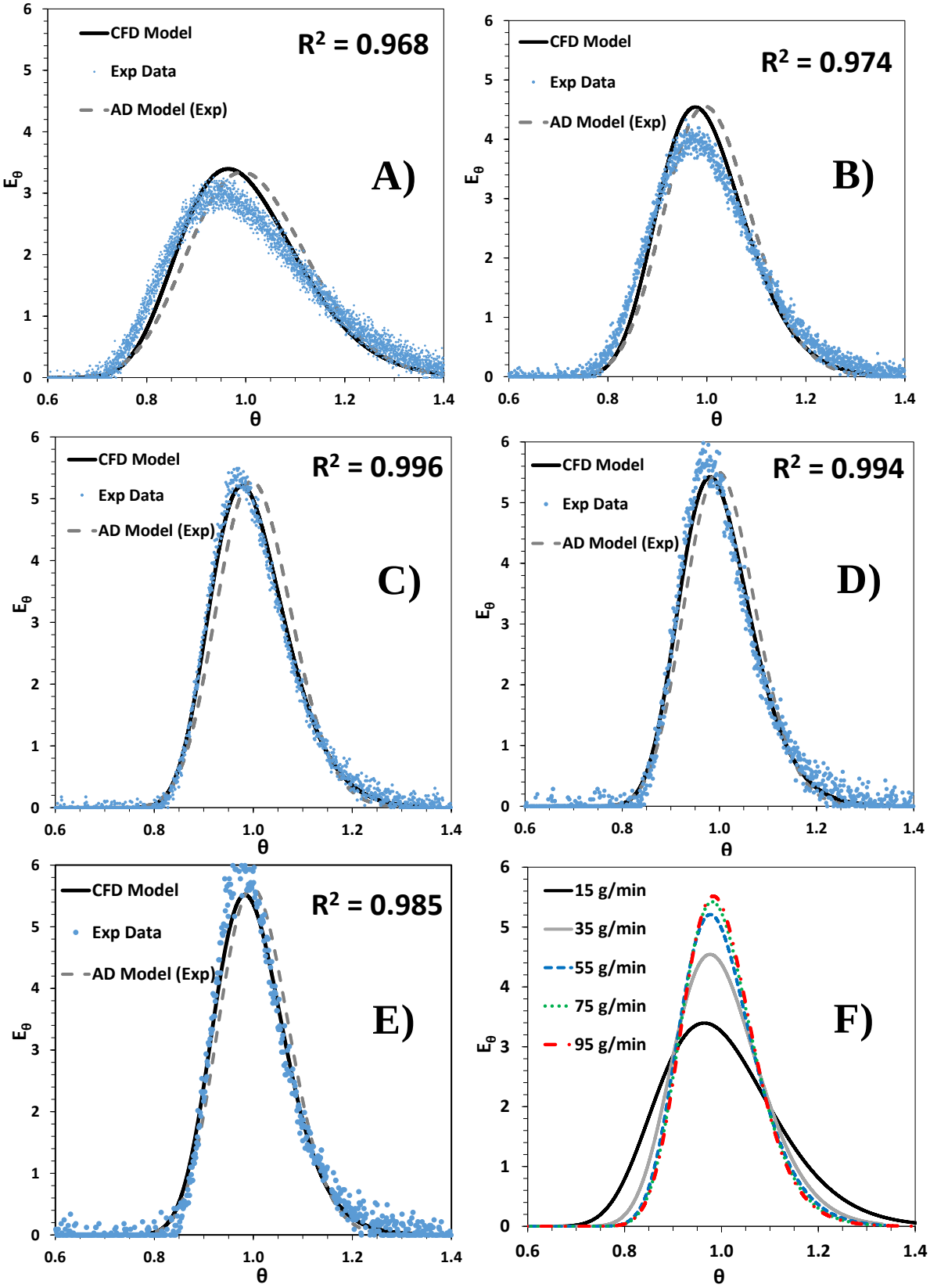

Figure B-2.8. Validation of macromixing performance in LL4361 via dimensionless RTD (E_θ) predictions at flow rates (g/min) of A) 15, B) 35, C) 55, D) 75, E) 95, and (F) all

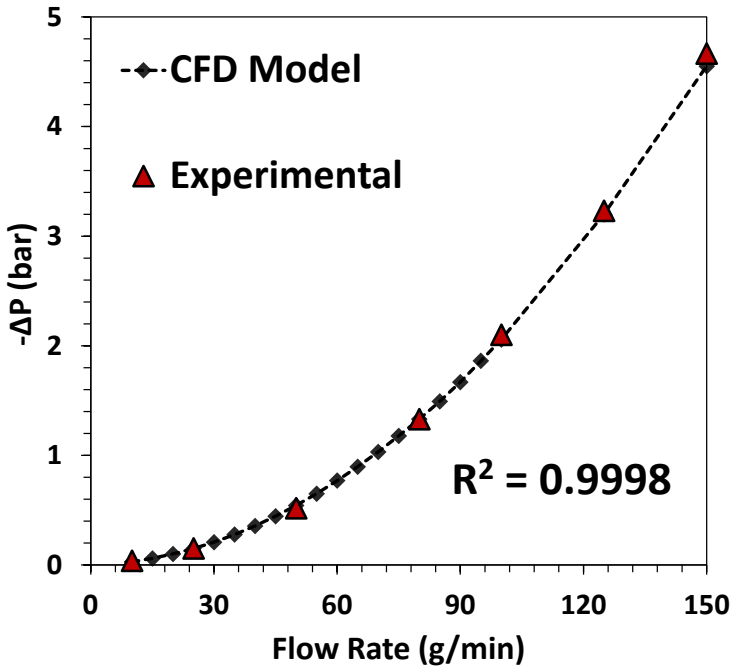

Figure B-2.9. Validation of pressure drop predictions in LL4351 as a function of flow rate

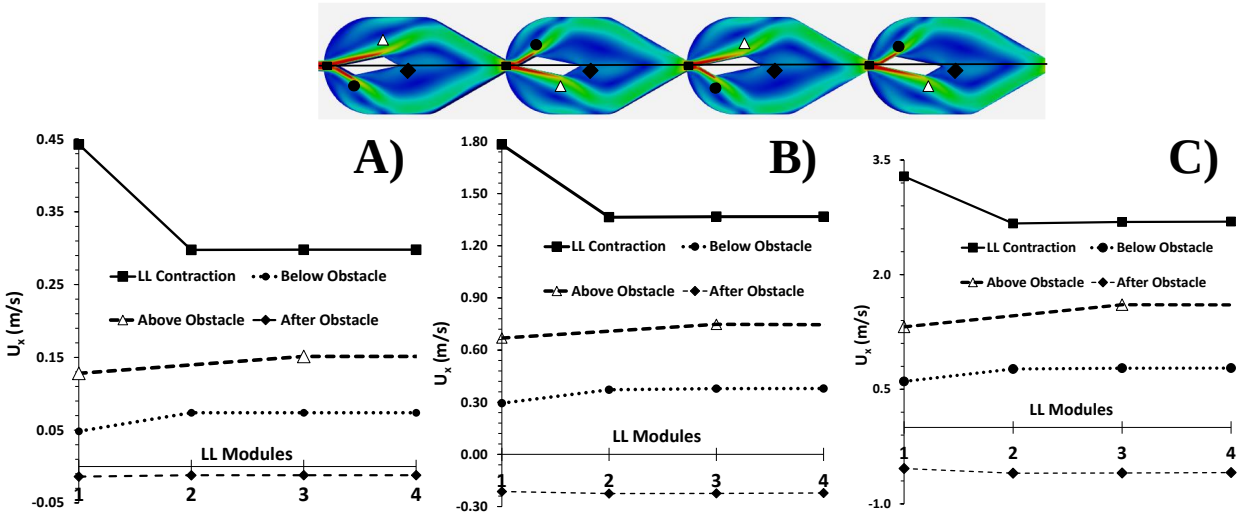

Figure B-2.10. Local velocity computations at four locations inside the LLM for several modules in series at flow rates (g/min) of A) 10, B) 50, and C) 100. Velocity taken at z = 0.3625 mm and direction of flow is from left to right

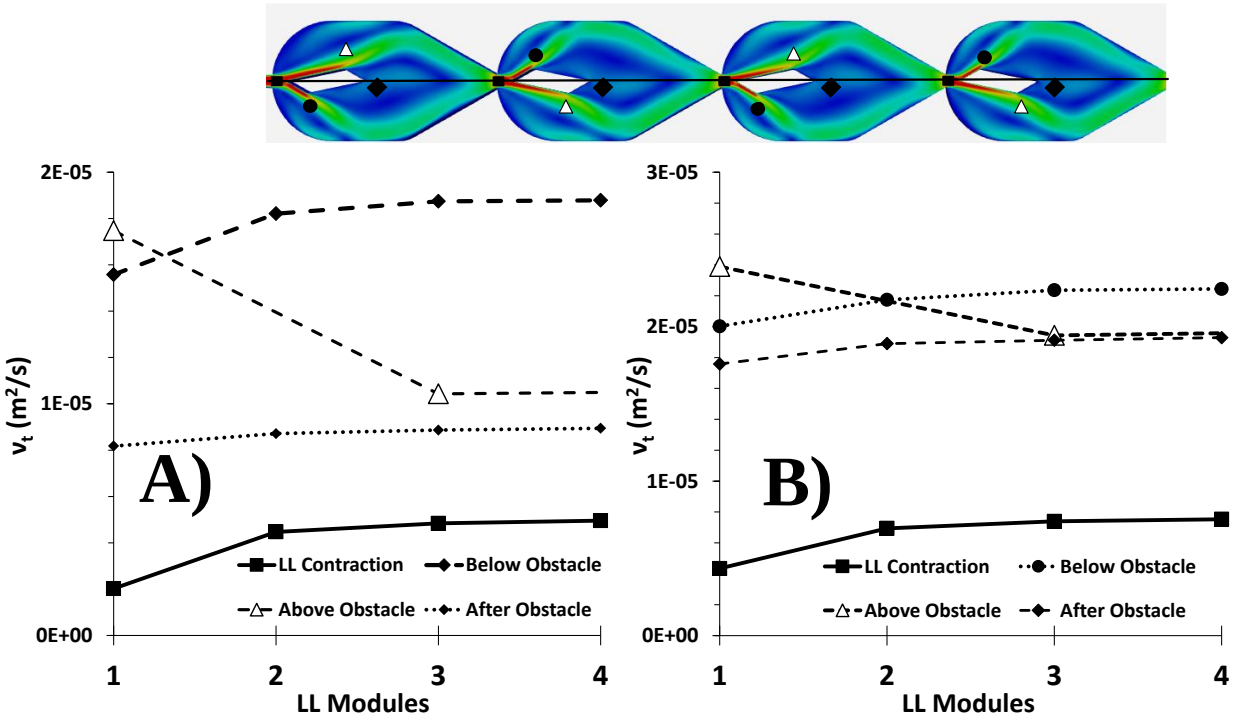

Figure B-2.11. Turbulent viscosity computations at four locations inside the LLM for several modules in series at flow rates (g/min) of A) 50 and B) 100. Local values taken at center-plane depth (z = 0.625 mm) and direction of flow is from left to right

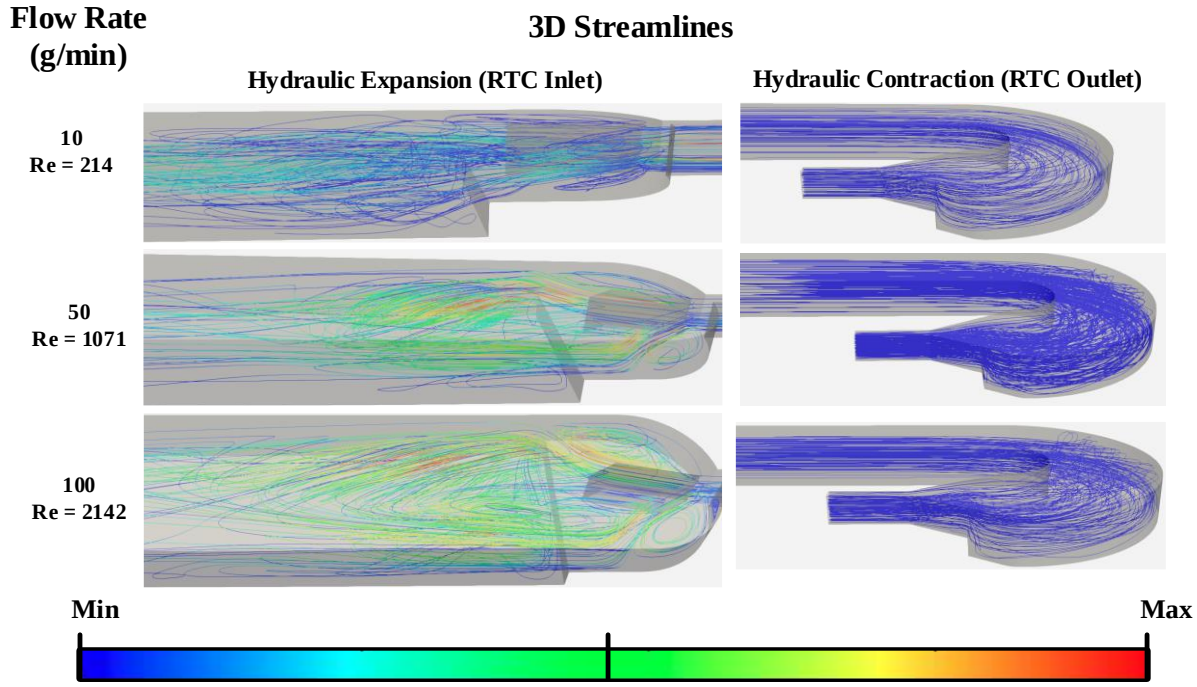

Figure B-2.12. 3D streamlines in the hydraulic regions of the RTC at different flow rates. Direction of flow is from right to left in the expansion (left) and from top to bottom in the contraction (right)

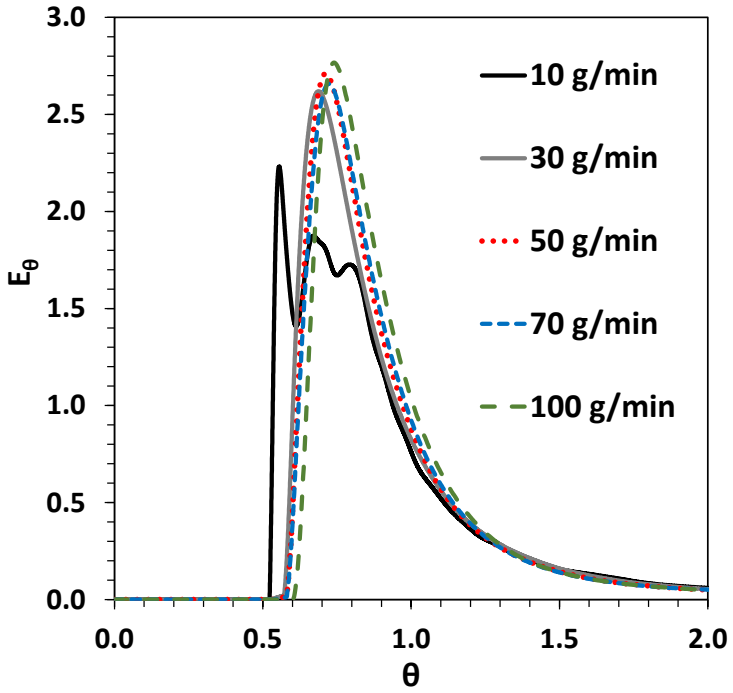

Figure B-2.13. Dimensionless RTD (E_θ) of RTR at flow rates (g/min) of 10 (black), 30 (grey), 50 (red), 70 (blue), and 100 (green)

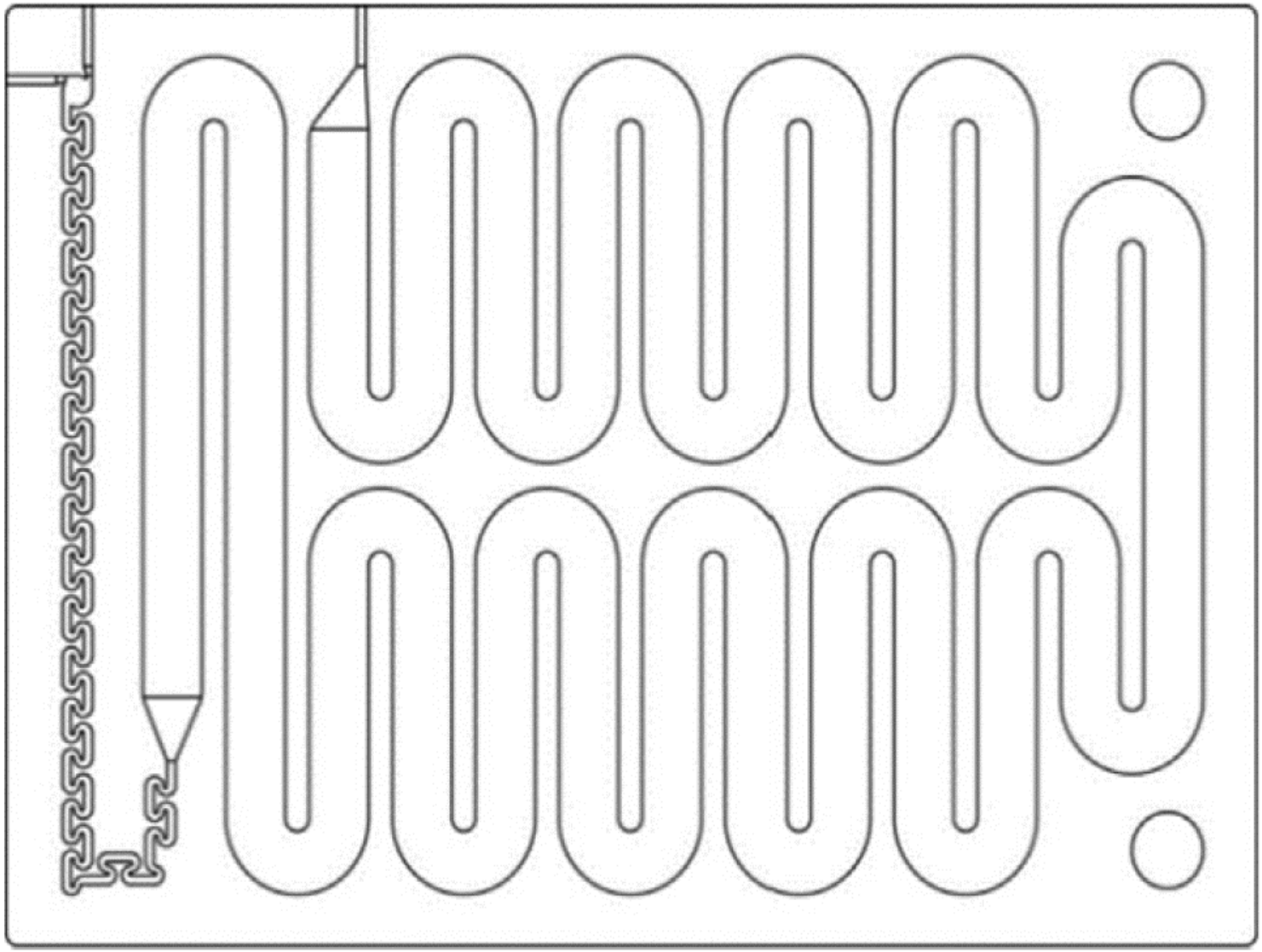

Figure B-3.1. SZ microreactor. Reactor plate is 260 × 148 × 5 mm. Direction of flow is downward from the top-left inlet

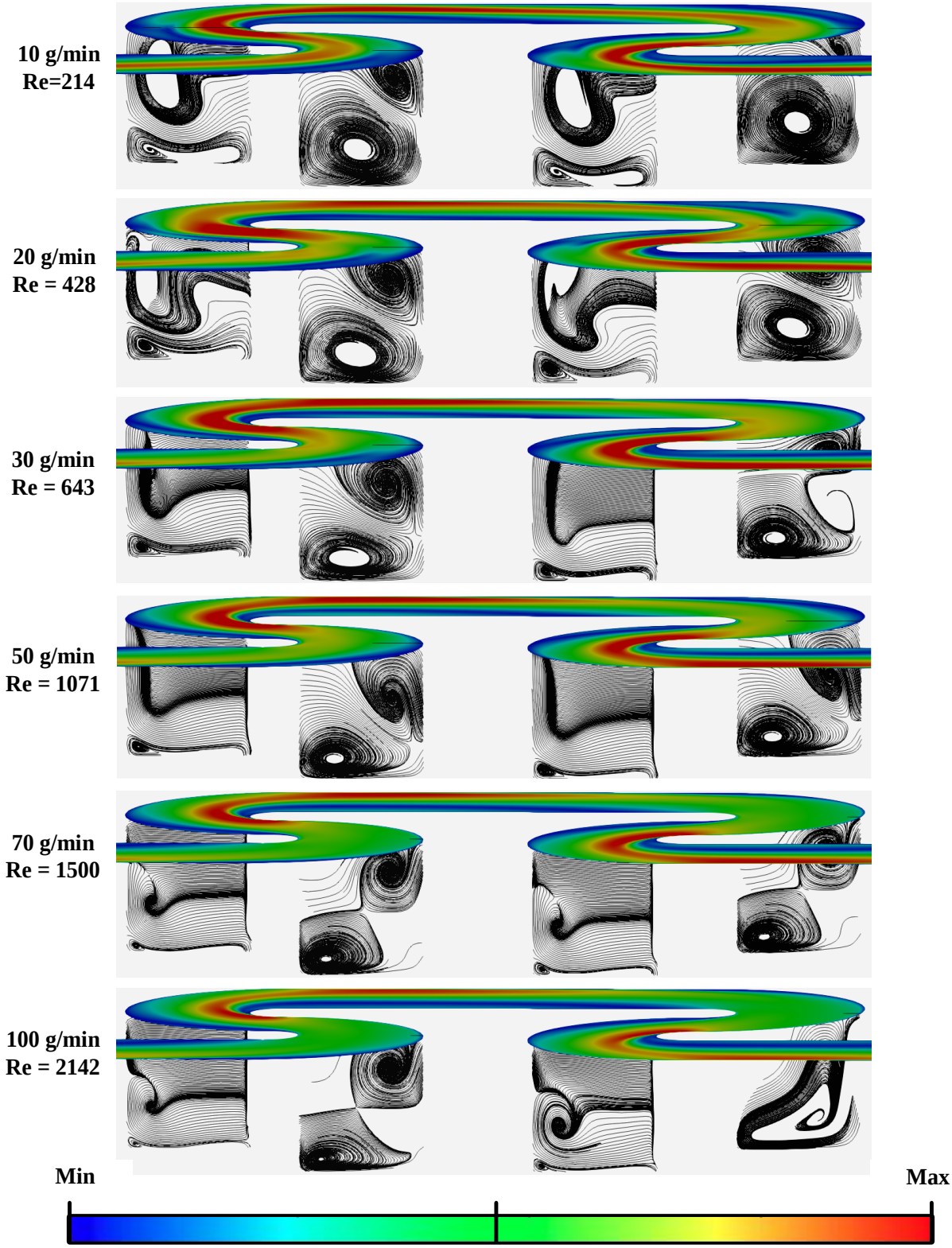

Figure B-3.2. Centerline velocity magnitude (coloured) and Dean vortices (black) perpendicular to the plane of angular rotation in the SZ. U_{min}= 0 (blue) for each flow rate, whereas U_{max} (red) varies as follows (m/s): 0.45 (10 g/min), 0.91 (20 g/min), 1.28 (30 g/min), 2.21 m/s (50 g/min), 3.39 (70 g/min) and 5.37 (100 g/min)

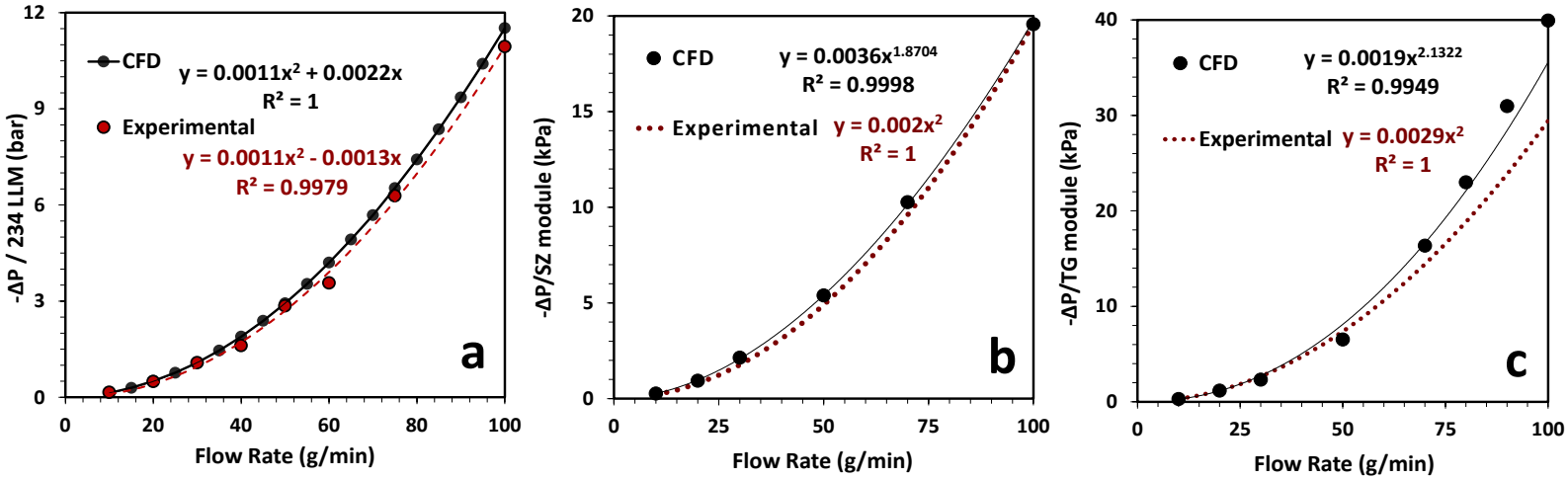

Figure B-3.3. Validation of pressure drop predictions in the LLM (a), SZ (b) and TG (c) modules as a function of flow rate. CFD predictions were validated in comparison to experimental data. The validation was carried out for the LLM on the basis of an entire microreactor (234 LLMs in series), whereas SZ and TG predictions were validated on a per-module basis

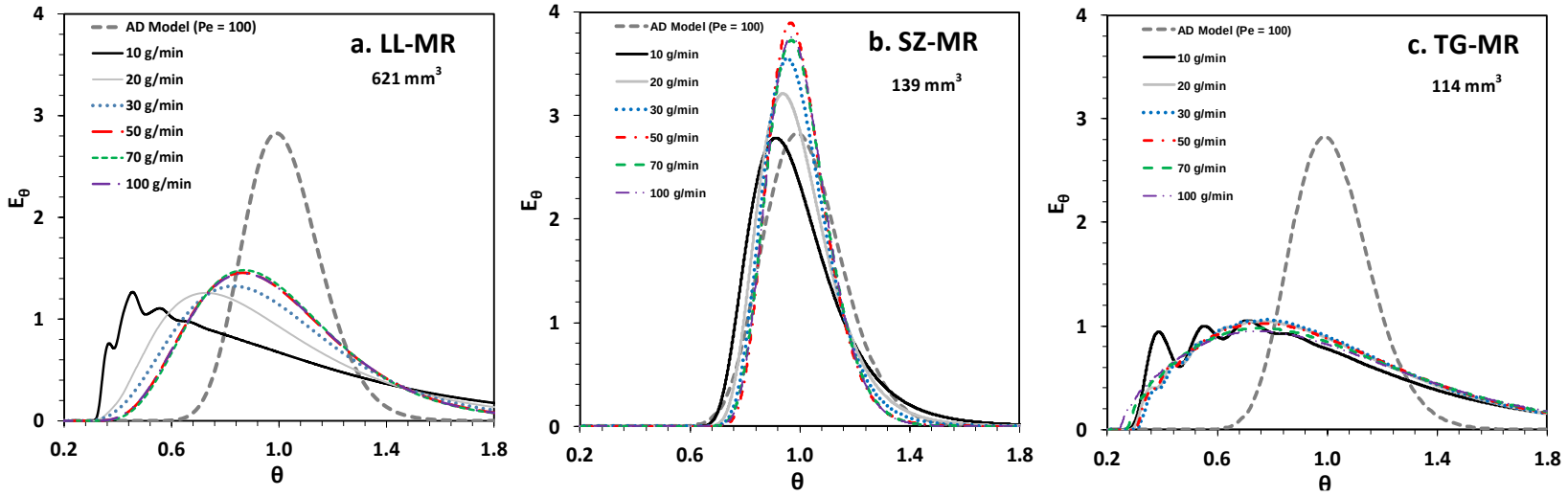

Figure B-3.4. CFD predictions of the dimensionless RTD (E_θ) in the mixing region of the LL (a), SZ (b) and TG (c) microreactors at flow rates ranging from 10 to 100 g/min. An axial dispersion model curve mimicking a near-plug-flow profile (Pe = 100) is shown for better perception of macromixing performance

Appendix C. Supplementary Tables

Chapter 2. CFD Simulation of Pressure Drop and Macromixing in LL Microreactors

Table C-2.1. Comparison of pressure drop predictions in LL mixing module by different turbulence models

Q (g/min)	Re	$-\Delta P_{LL,exp}$ (kPa)	*k-ε* Model		*k-ω* SST Model		*k-ω* SSTLM Model	
			$-\Delta P_{LL,CFD}$ (kPa)	$Diff._{CFD/Exp}$ (%)	$-\Delta P_{LL,CFD}$ (kPa)	$Diff._{CFD/Exp}$ (%)	$-\Delta P_{LL,CFD}$ (kPa)	$Diff._{CFD/Exp}$ (%)
10	214	0.061			0.058	-4.9%	0.058	-4.3%
20	428	0.173			0.201	-12.5%	0.204	-11.2%
30	643	0.383			0.446	-5.8%	0.446	-5.8%
40	857	0.688			0.767	11.4%	0.768	11.5%
50	1071	1.066	1.296	21.6%	1.172	10.0%	1.159	8.7%
60	1285	1.523			1.680	10.3%	1.672	9.8%
75	1607	2.331			2.579	10.6%	2.587	11.0%
100	2142	4.676			-	-	4.619	1.2%

Table C-2.2. Numerical solvers used in CFD simulations completed in OpenFOAM

Variable	Solver
Pressure	Geometric-Algebraic Multi-Grid (GAMG)
Velocity	Stabilized Preconditioner Biconjugate Gradient (PBiCGStab)
k, ν_t , ω, γ_{int} , $Re_{\theta,t}$ (Turbulence)	smoothSolver (w/ symGaussSiedel smoother)
Concentration	PBiCGStab

Table C-2.3. Numerical schemes (2^{nd}-order) used in CFD simulations completed in OpenFOAM

Calculation	simpleFoam	scalarTurbTransportFoam	pimpleFoam
Gradient	Gauss linear	Gauss linear	Gauss linear
Divergence	Gauss linearUpwind	Gauss linearUpwind	Gauss linearUpwind
Laplacian	Gauss linear corrected	Gauss linear corrected	Gauss linear corrected
Interpolation	Linear	Linear	Linear
Time Derivative	steadyState	CrankNicolson	CrankNicolson

Table C-2.4. Number of cells in 3D mesh of the repeating segments (R1–R6) of each LL reactor configuration

Reactor Configuration	Number of Mesh Cells per Region					
	R1	R2	R3	R4	R5	R6
LL4341	2 385 640	1 402 744	1 126 068	1 070 388	1 258 606	702 120
LL4351	2 385 640	1 409 512	818 068	775 380	938 708	413 584
LL4361	2 385 640	1 744 600	1 126 068	1 070 388	1 990 222	702 120
LL4381	2 385 640	2 214 000	1 194 520	1 048 880	1 922 720	1 194 520

Table C-2.5. Boundary conditions used in CFD simulations completed in OpenFOAM

Simulation	Variable	Boundary Patch	Specification
simpleFoam	Velocity	Inlet	fixed flat profile
		Walls	no slip
		Outlet	zero gradient
	k	Inlet	fixed value
		Walls	kLowReWallFunction
		Outlet	zero gradient
	ω	Inlet	fixed value
		Walls	omegaWallFunction
		Outlet	zero gradient
	ν_t	Inlet	calculated
		Walls	nutLowReWallFunction
		Outlet	calculated
	γ_{int}	Inlet	fixed value
		Walls	zero gradient
		Outlet	zero gradient
	$Re_{\theta,t}$	Inlet	fixed value
		Walls	zero gradient
		Outlet	zero gradient
	Pressure	Inlet	zero gradient
		Walls	zero gradient
		Outlet	fixed value
scalarTurbTransportFoam	Concentration	Inlet	uniform fixed value
		Walls	zero gradient
		Outlet	zero gradient

Table C-2.6. Comparison of experimental and CFD pressure drop results in LL4381

Q (g/min)	10	20	30	40	50	60	75	100
Reynolds No.	214	428	643	857	1071	1285	1607	2142
$-\Delta P_{CFD}$ (bar)	0.137	0.508	1.083	1.891	2.931	4.203	6.527	11.519
$-\Delta P_{Exp}$ (bar)	0.153	0.490	1.076	1.611	2.851	3.564	6.284	10.941
Error (%)	-10.5%	3.7%	0.6%	17.4%	2.8%	17.9%	3.9%	5.3%

Table C-2.7. Comparison of experimental and CFD pressure drop results in LL4351

Q (g/min)	10	25	50	80	100	125	150
Reynolds No.	214	536	1071	1714	2142	2678	3213
$-\Delta P_{CFD}$ (bar)	0.029	0.150	0.544	1.331	2.058	3.200	4.551
$-\Delta P_{Exp}$ (bar)	0.038	0.151	0.518	1.330	2.101	3.232	4.666
Error (%)	-22.7%	-0.7%	5.0%	0.1%	-2.1%	-1.0%	-2.5%

Table C-2.8. Comparison of experimental and CFD pressure drop results in LL4341

Q (g/min)	10	20	30	50	75	100
Reynolds No.	214	428	643	1071	1607	2142
$-\Delta P_{CFD}$ (bar)	0.046	0.168	0.358	0.965	2.144	3.794
$-\Delta P_{Exp}$ (bar)	0.122	0.248	0.395	0.884	1.842	3.390
Error (%)	-61.8%	-32.2%	-9.3%	9.2%	16.4%	11.9%

Table C-2.9. Comparison of experimental and CFD pressure drop results in LL4361

Q (g/min)	10	20	30	50	75	100
Reynolds No.	214	428	643	1071	1607	2142
$-\Delta P_{CFD}$ (bar)	0.047	0.171	0.365	0.980	2.188	3.882
$-\Delta P_{Exp}$ (bar)	0.058	0.189	0.383	1.004	2.191	3.859
Error (%)	24.1%	10.6%	5.1%	2.5%	0.2%	-0.6%

Table C-2.10. Comparison of experimental and CFD RTD results in LL4381

Q (g/min)	Re	Pe	1st RTD Moment			2nd RTD Moment		R^2
			τ (s)	$\bar{t}_{Exp}$ (s)	$\bar{t}_{CFD}$ (s)	σ^2_{Exp} (s^2)	σ^2_{CFD} (s^2)	
15	321	155	45.9	45.0	46.5	22	29	0.979
35	750	265	19.7	20.1	19.8	2.8	3.0	0.991
55	1178	385	12.5	13.3	12.6	0.8	0.8	0.994
75	1607	394	9.2	-	9.3	-	0.5	-
95	2035	384	7.2	-	7.3	-	0.3	-

Table C-2.11. Comparison of experimental and CFD RTD results in LL4351

Q (g/min)	Re	1st RTD Moment			2nd RTD Moment		R^2
		τ (s)	$\bar{t}_{Exp}$ (s)	$\bar{t}_{CFD}$ (s)	σ^2_{Exp} (s^2)	σ^2_{CFD} (s^2)	
15	321	88.3	79.3	87.2	190	267	0.996
35	750	37.9	38.2	37.8	25.5	30.6	0.998
55	1178	24.1	24.3	23.6	9.4	9.9	0.997
75	1607	17.7	17.1	19.5	5.2	6.8	0.992
95	2035	14.0	14.9	15.9	2.8	2.9	0.994

Table C-2.12. Comparison of experimental and CFD RTD results in LL4341

Q (g/min)	Re	1st RTD Moment			2nd RTD Moment		R^2
		τ (s)	$\bar{t}_{Exp}$ (s)	$\bar{t}_{CFD}$ (s)	σ^2_{Exp} (s^2)	σ^2_{CFD} (s^2)	
15	321	80.4	77.7	76.1	105	104	0.995
35	750	34.5	36.0	33.6	18	17	0.996
55	1178	21.9	23.4	21.6	6.7	7.2	0.995
75	1607	16.1	17.1	15.9	3.4	3.7	0.995
95	2035	12.7	14.0	12.6	2.1	2.0	0.994

Table C-2.13. Comparison of experimental and CFD RTD results in LL4361

Q (g/min)	Re	Pe	1st RTD Moment			2nd RTD Moment		R^2
			τ (s)	$\bar{t}_{Exp}$ (s)	$\bar{t}_{CFD}$ (s)	σ^2_{Exp} (s^2)	σ^2_{CFD} (s^2)	
15	321	140	81.4	74.9	79.0	103	89	0.968
35	750	260	34.9	35.0	34.5	13.1	9.8	0.974
55	1178	340	22.2	23.1	22.1	3.6	3.2	0.996
75	1607	380	16.3	16.6	16.2	1.5	1.6	0.994
95	2035	398	12.9	13.2	12.8	0.9	1.0	0.985

Chapter 3. Impact of micromixer geometry on residence time and mixing time distributions in the interest of competitive reaction yield

Table C-3.1. Numerical solvers used in CFD simulations completed in OpenFOAM

Variable	Solver
Pressure	Geometric-Algebraic Multi-Grid (GAMG)
Velocity ($\overline{\mathbf{U}}$)	Stabilized Preconditioner Biconjugate Gradient (PBiCGStab)
$k, \nu_t, \omega, \gamma_{int}, Re_{\theta,t}$ (Turbulence)	smoothSolver (w/ symGaussSiedel smoother)
Concentration (C_T)	PBiCGStab
Environment 1 volume fraction (α_1)	smoothSolver (w/ GaussSiedel smoother)
Mixture fractions and variance (a_1, a_2, X_1, X_2)	PBiCGStab
Reaction progress variables (Y_{21}, Y_{22})	PBiCGStab

Table C-3.2. Numerical schemes (2nd-order) used in CFD simulations completed in OpenFOAM

Calculation	simpleFoam	scalarTurbTransportFoam	scalarMicroMixingFoam	twoLiquidIEMFoam
Gradient	Gauss linear	Gauss linear	cellLimited leastSquares	Gauss linear
Divergence	Gauss linearUpwind			
Laplacian	Gauss linear corrected			
Interpolation	Linear			
Time Derivative	steadyState	CrankNicolson	steadyState	Euler